UNIVERSIDAD NACIONAL AUTÓNOMA DE MEXICO

DOCTORADO EN CIENCIAS (FÍSICA)

INSTITUTO DE FÍSICA

COSMOLOGICAL IMPLICATIONS AND OBSERVATIONAL CONSTRAINTS ON DARK ENERGY AS A SCALAR FIELD CONDENSATE WITH AN INVERSE POWER LAW POTENTIAL

TESIS
QUE PARA OPTAR POR EL GRADO DE:
DOCTOR EN CIENCIAS (FÍSICA)

PRESENTA:
ERICK JONATHAN ALMARAZ AVIÑA

TUTOR PRINCIPAL
DR. AXEL RICARDO DE LA MACORRA PETTERSSON MORIEL
INSTITUTO DE FÍSICA

MIEMBROS DEL COMITÉ TUTOR
DR. JERÓNIMO ALONSO CORTEZ QUEZADA
FACULTAD DE CIENCIAS

DR. DARÍO NÚÑEZ ZÚÑIGA
INSTITUTO DE CIENCIAS NUCLEARES

CIUDAD UNIVERSITARIA, CIUDAD DE MÉXICO, JUNIO 2018

Contents

Resumen

El desarrollo alcanzado por la cosmología en los últimos veinticinco años ha marcado el inicio de lo que se considera una época dorada en cuanto a nuestro conocimiento del pasado y evolución del universo a gran escala. Sobre la base de la teoría general de la relatividad y la física de las interacciones fundamentales que conocemos, el modelo cosmológico estándar (ΛCDM) se presenta como el esquema teórico más simple con el que se puede describir consistentemente la evidencia observacional disponible en la actualidad. En este esquema, la expansión acelerada del universo tardío descubierta a finales del siglo pasado y su confirmación en los años subsiguientes, requiere de la introducción de una forma exótica de materia denominada como *energía oscura* parametrizada por una constante cosmológica Λ en las ecuaciones del modelo. Al margen del éxito de la teoría, la identificación de la naturaleza de la energía oscura permanece como uno de los más grandes desafíos de la física moderna. La dificultad más importante se encuentra en la existencia de una fuerte discrepancia entre las estimaciones teóricas al valor de Λ dadas por la física de altas energías, y las cotas extraídas de las observaciones. En el advenimiento de la era de la alta precisión en la cosmología, esta dificultad vuelve indispensable la búsqueda de escenarios alternativos que proporcionen una respuesta más satisfactoria a la cuestión del origen de la energía oscura.

El objetivo de este trabajo es evaluar la viabilidad del modelo de Energía Oscura Ligada (BDE) como una de las posibles alternativas a la constante cosmológica. En nuestro estudio presentamos los fundamentos teóricos del modelo, describimos su fenomenología tanto a nivel de fondo como en las perturbaciones, exploramos las implicaciones cosmológicas y encontramos las constricciones a sus parámetros a partir de evidencia observacional reciente.

La idea central del modelo BDE consiste en introducir un grupo de norma oscuro no abeliano $SU(N_c)$ de partículas ligeras con $N_c = 3$ colores y $N_f = 6$ sabores en su representación fundamental. Partiendo de la escala de unificación $\Lambda_{gut} \sim 10^{16}$ GeV, la interacción entre las partículas del grupo oscuro con las del Modelo Estándar es puramente gravitacional, mientras que el acoplamiento entre ellas inicialmente es pequeño, de manera que las partículas son libres. Luego, a medida que el universo se expande y la temperatura desciende, la constante de acomplamiento crece de modo que estas partículas dejan de ser libres y pasan a formar estados ligados de manera similar a como lo hacen los quarks en la interacción fuerte. En el escenario más simple, la tran-

sición de fase del grupo oscuro se da únicamente a un mesón ultraligero descrito por un campo escalar φ con un potencial de ley inversa de potencias $V(\varphi) = \Lambda_c^{4+\alpha}\varphi^{-\alpha}$, en donde la escala de la condensación del campo $\Lambda_c = 34^{+16}_{-11}$ eV, la época a la que ocurre $a_c = 1.0939 \times 10^{-4}/(\Lambda_c/\mathrm{eV})$, el exponente del potencial $\alpha = 2/3$ y las condiciones iniciales del campo, son cantidades derivadas que sólo dependen de los parámetros N_c y N_f del grupo oscuro y de la escala de energía y la constante de acoplamiento $g_{gut}^2 = 4\pi/(25.83 \pm 0.16)$ en la unificación. *La energía oscura corresponde precisamente a este mesón escalar* φ y dado que el mecanismo que origina al mesón es el confinamiento de partículas libres, el modelo recibe el nombre de Energía Oscura Ligada.

A diferencia del esquema tradicional de quintaesencia en donde el campo escalar sólo es relevante en épocas tardías a pesar de estar presente a lo largo de toda la historia del universo, en el modelo BDE el parámetro de densidad del campo escalar cuando ocurre la condensacion en a_c (mucho antes de la época de igualdad de materia-radiación) no es despreciable. Sin embargo, esta cantidad de energía oscura temprana se diluye rápidamente después de a_c, siendo subdominante la mayor parte del tiempo hasta volver a ser relevante en épocas tardías como lo requiere las observaciones. Téoricamente este escenario resulta atractivo por tres razones importantes:

(i) El número de parámetros cosmológicos baśicos del modelo BDE es uno menos que los de ΛCDM, por lo que no introducimos parámetros básicos adicionales, como en otros modelos alternativos.

(ii) El mecanismo que da origen a la energía oscura proviene de física de primeros principios mediante la que es la más simple extensión al Modelo Estándar de las partículas elementales.

(iii) El modelo BDE no requiere de un ajuste fino en sus parámetros para reproducir las observaciones.

La dinámica de la energía oscura en el modelo BDE afecta tanto la evolución del universo de fondo como las perturbaciones, llevando a diferencias respecto a ΛCDM principalmente en: i) las distancias cosmológicas, ii) la fracción de núcleos ligeros (helio y deuterio) producidos en el universo temprano, iii) el espectro de potencias de materia a escalas pequeñas y iv) el espectro de potencias de las anisotropías de la temperatura de la radiación cósmica de fondo (CMB) a multipolos pequeños. En nuestro estudio consideramos datos recientes de las distancias de supernovas del tipo Ia (SNeIa), de la señal de las oscilaciones acústicas de bariones (BAO) impresas en censos de galaxias y mediciones del espectro de anisotropías del CMB para constreñir las condiciones a las que se da la condensación del campo escalar, así como el valor de los parámetros cosmológicos en nuestra época. Los resultados que encontramos muestran que el modelo BDE es consistente con las observaciones cuando la condensación tiene lugar a una escala $\Lambda_c = 44.09 \pm 0.28$ eV, en una época dada por $a_c = (2.48 \pm 0.02) \times 10^{-6}$, con una densidad inicial del campo de $\Omega_{\mathrm{BDEc}} = 0.112$. El valor actual de la ecuación de estado de la energía oscura, la tasa de expansión y la densidad de materia es $w_{\mathrm{BDE0}} = -0.9294 \pm 0.0007$, $H_0 = 67.82 \pm 0.55$ km $\cdot$ s^{-1}Mpc^{-1} y $\Omega_m = 0.304 \pm 0.007$, respectivamente, siendo estos dos últimos resultados consistentes con las constricciones al modelo ΛCDM usando los mismos datos observacionales. Esta concordancia también la obtenemos para el resto de los parámetros cosmológicos, con excepción de las abundancias de helio y deuterio primordiales, en donde el modelo BDE arroja una fracción más elevada de estos elementos, que por el momento no puede ser verificada por las observaciones dada la dispersión de los datos. No obstante, resulta particularmente estimulante que la calidad del ajuste de nuestro modelo es mejor que la de ΛCDM, concretamente en la información de BAO, en donde se espera obtener mediciones más precisas en los años venideros que habrá que seguir con detenimiento.

Nuestra conclusión principal es que el modelo BDE se mantiene como una opción viable a la constante cosmológica, que cumple con los requerimientos indispensables de fundamentación teórica y consistencia con las observaciones. En la medida en la que se diversifiquen las observables cosmológicas, aumente la precisión de los datos y se identifiquen claramente las tensiones con el modelo estándar, será posible establecer un ruta clara hacia el entendimiento de la naturaleza de la energía oscura.

Abstract

In this work we assess the viability of a dark energy model derived from a natural extension of the Standard Model of particle physics as a possible alternative to the cosmological constant (ΛCDM). Dark energy corresponds to the lightest meson state generated during the phase transition of a hidden gauge group occurring at an energy scale Λ_c and scale factor a_c. The resulting dark energy meson is described by a minimally coupled scalar field φ with an inverse power law potential $V(\varphi) = \Lambda_c^{4+2/3}\varphi^{-2/3}$, where the value of Λ_c and a_c, the exponent $n = -2/3$ of the potential and the initial conditions of the scalar field at the phase transition are quantities derived from theoretical considerations. Moreover, Λ_c and a_c are related by an exact theoretical constraint $a_c\Lambda_c/\mathrm{eV} = 1.0939 \times 10^{-4}$. Our model does not introduce extra free cosmological parameters, but in principle it also has one less free parameter than ΛCDM. We study the cosmological implications of the model both at the background and at the perturbative level, particularly its effects on the cosmological distances, the evolution of matter inhomogeneities and radiation anisotropies, and the production of light nuclei in the early universe. We constrain the model using recent observations of the luminosity distance of type Ia supernovae (SNeIa), the baryon acoustic oscillations (BAO) feature in galaxy surveys, and measurements of the temperature anisotropy spectrum of the Cosmic Microwave Background radiation (CMB). The constraint $\Lambda_c = 44.09 \pm 0.28$ eV we find is consistent with our theoretical expectations $\Lambda_c^{th} = 34^{+16}_{-11}$ eV, leading to $a_c = (2.48 \pm 0.02) \times 10^{-6}$. Remarkably our model not only fits well the data but it also improves the ΛCDM fit to BAO measurements by 21%. This result, together with distinctive signatures in the matter power spectrum and definite predictions on the abundance of light nuclei produced during Big Bang Nucleosynthesis, open the possibility of discriminate our model from the cosmological constant in the forthcoming years.

Introduction

The detection of the anisotropies in the Cosmic Microwave Background Radiation (CMB) [1] at the end of the past century has set the beginning of a golden age in cosmology, characterised by the increasing precision of the observations and the diversification of the cosmological probes. The progress achieved during these years has revealed us a detailed picture of the history of the universe to an unprecedented level of accuracy. Based on the general theory of relativity and the Standard Model of particle physics, the standard cosmological model (ΛCDM) is the simplest account of the universe at large scales that is consistent with the observations. According to this model, the discovery of the late time accelerated expansion of the universe [2, 3] together with the evidence gathered over the following years [4–9] requires the introduction of an exotic form of matter called *dark energy*, which is simply parameterized by a cosmological constant Λ. However, despite the success of the ΛCDM model in fitting the observations, the physical explanation of the nature of the dark energy remains as one of the most challenging problems of modern science. If dark energy is due to the vacuum energy of all the fields present in the universe, the most conservative calculations based on quantum field theory overestimate the observed value of Λ by many orders of magnitude [10, 11]. Moreover, there is no a natural explanation of why the value of the cosmological constant that is realised in nature is such that the universe has just entered the epoch of dark energy dominance [12]. Since dark energy amounts to almost the 70% of the energy content of the universe at present, this means that we are missing the physics behind the main ingredient the universe is made of. In the era of high precision in cosmology, these two shortcomings of the ΛCDM paradigm impel us to find alternative scenarios that provide a more satisfactory answer to the problem of the physical origin of the dark energy.

There have been many attempts to solve the problem including the reinterpretation of the observational evidence [13, 14], the effects of an inhomogeneous distribution of matter [15, 16], the replacement of the cosmological constant by some scalar field [17], and even modifications to the general theory of relativity [18]. These proposals (or any other) will be considered as possible solutions to the dark energy problem or will be ruled out insofar they consistently describe the increasing amount of observational data [19]. *The goal of this study is to assess the possibility of describing dark energy as a particle condensate generated during a phase transition in the history of the universe.*

Our dark energy model [20–23] introduces a non-Abelian supersymmetric gauge group $SU(N_c)$ of light particles with N_c colours and N_f flavours in its fundamental representation. Below the unification scale Λ_{gut} our dark group is coupled with the particles of the Standard Model only through gravity. Initially, the gauge interaction of the dark group is weak, so the corresponding elemental particles are free and its energy density evolves as radiation. Then, as the expansion proceeds and the temperature drops off, the gauge interaction becomes strong and now the particles of the dark group bind together forming dark hadrons and mesons at a condensation scale Λ_c and scale factor a_c. Dark energy is just the lightest scalar meson formed by the non-perturbative interaction of the dark group at low energies. This picture is similar to Quantum Chromodynamics, where the hadrons form due to the strong binding of elemental quarks below the condensation scale $\Lambda_{\mathrm{QCD}} \approx 200$ MeV. Since in this case the physical mechanism generating the dark energy is the binding of initially free particles, we refer to our model as Bound Dark Energy (BDE). The evolution of the light meson corresponding to the dark energy is described by the dynamics of a scalar field φ with an inverse power law potential $V(\varphi) = \Lambda_c^{4+2/3}\varphi^{-2/3}$, where the condensation scale Λ_c, the exponent of the potential $n = -2/3$, and the initial conditions of the scalar field at the phase transition are all derived quantities.

We see then, that unlike traditional quintessence models, where the scalar field is a fundamental entity present in the whole history of the universe (although it is only relevant at late times), the particle condensates representing the dark energy in our BDE model are only present after the phase transition at a_c; before that, there was an extra amount of radiation due to the $SU(N_c)$ group. Among the distinctive theoretical features of our model we may list: i) once we set the fundamental parameters of the dark group N_c and N_f, all the relevant quantities of the model are determined, so we are not introducing any extra free cosmological parameter, ii) we don't need to fine tune the parameters of the model to reproduce the observations, and iii) dark energy is explained from first principles by using what seems to be the most viable extension of the Standard Model of particle physics. Although the theoretical foundations and the basic features of the model were extensively studied in the early 2000's, these analyses were limited to the evolution of the background and the observational evidence available at that time was insufficient to yield accurate constraints. As we mentioned at the beginning of this section, cosmology has undergone a profound transformation since the discovery of the anisotropies of the CMB and we expect that in this high precision era we unravel the true nature of the dark energy. Here we present the first precision constraints on the BDE model, extending the analysis to include dark energy inhomogeneities and the effects on the dynamics of matter and radiation perturbations.

This document is organised as follows. In chapter (1) we do a short review of the ΛCDM model, focusing on the relevant aspects to our research such as the evolution of the homogeneous universe and the essentials of perturbation theory. Then, in chapter (2) we discuss the observational evidence appealing for the introduction of the dark energy in cosmology and the problems of describing it through a cosmological constant. Here we make some comments about the role played by scalar field theories as possible candidates for dark energy. We present our BDE model in chapter (3). Since the aim of this research is to assess the viability of this model as a dark energy candidate, we focus on its cosmological implications rather than on its high-energy physics theoretical foundations, which are fully explained in [20–23]. Here we introduce the parameters of the model and we show the evolution of dark energy both at the background and perturbation level. The cosmological implications of the model are explored in chapter (4). We compare the predictions of our model on cosmological distances, the fraction of light nuclei produced in the early universe, the evolution of matter overdensities and the CMB power spectrum, with a ΛCDM cosmology running with the same set of basic parameters. This shows us the intrinsic differences that arise from the effects of the dynamics of the dark energy in our model. Then, in chapter (5) we present the constraints on the BDE model obtained from multiple datasets and we use these results to set predictions that might help us to discriminate between our model and ΛCDM in the future. Finally we give our conclusions.

In this document we adopt the usual conventions on notation and terminology found in the literature: repeated indices are implicitly summed over and a zero subfix/superfix denotes the value of a given quantity at the present epoch. Unfortunately, there are few important exceptions that we have to be aware of. Some authors denote the matter density parameter today by Ω_{m0}, but others use Ω_m. Moreover, we rapidly run short of letters and it is common to find that τ is used to designate the conformal time and the optical depth. In any case, we make sure to explain the meaning of each term in our expressions.

Chapter 1

The standard cosmological model

The standard csomological model (ΛCDM) is based on two fundamental hypotheses: i) the universe is homogeneous and isotropic at large scales (the cosmological principle) and ii) the dominant interaction at cosmological scales is gravity, which is well described by the general theory of relativity (GR). Although the assumption of these hypotheses is justified by the success of the model in describing the observations available at present, it is important to be aware of the physical conditions under which these statements provide an accurate picture of the universe as a whole. The homogeneity and isotropy of the universe are features that only arise when we consider large enough volumes of space spanning distances of the order of hundreds of megaparsecs (Mpc), where the distribution of matter and radiation can be considered as uniform. At this level, the universe looks the same for any observer at any place[1]. On the other hand, the dominance of gravity over the other interactions means that gravity is the only force driving the expansion of the universe, although the electromagnetic and the weak and strong nuclear forces also leave important imprints on the early universe that can be tracked by the current cosmological probes. In this chapter we do a review of the basic elements of the standard cosmological model. We don't intend to make an exhaustive account of the state of the art, but only a short compilation of the results that we will be using throughout our work, omitting detailed calculations that can be carried out by oneself and verified by consulting the references we quote. This review will also serve as a theoretical reference against which we will compare the results of our dark energy model. The chapter is organized as follows. In section (1.1) we introduce the basic terminology and discuss the evolution of the homogeneous universe. We then depart from this simplified picture in section (1.2) and present the foundations of cosmological perturbation theory. We start by setting out the general equations of motion. Then we present the initial conditions needed to solve these equations and finally we discuss the evolution of matter and radiation perturbations.

---

[1] In this sense, the cosmological principle is compatible with a cosmic version of the Copernican principle, which at the time deprived Earth (and humankind) of a privileged position in the cosmos.

1.1 The homogeneous universe

The two fundamental cosmological hypotheses together with the empirical observation of the systematic recession of the farthest galaxies impel us to choose a convenient system of comoving coordinates where the position of free particles does not change with the expansion of the universe. In this system, the line element in the Friedmann-Lemaître-Robertson-Walker (FLRW) metric adopts the simple form:

$$ds^2 = -dt^2 + a^2(t)\left(\frac{dr^2}{1-Kr^2} + r^2 d\theta^2 + r^2 \sin^2\theta d\phi^2\right), \tag{1.1}$$

where t is the (comoving) time measured by an observer at rest in the comoving frame, r, θ and ϕ are radial and angular comoving spherical coordinates, $a(t)$ is the scale factor relating physical and comoving distances $d_{phys} = a(t)d_{com}$, and the constant $K = 1, -1, 0$ is the curvature corresponding to a closed, open and a flat universe, respectively. The observational evidence of the last years [24–26] favours the flat geometry over the non-flat scenarios, so from now on we will take $K = 0$ and omit any curvature term in our equations. In this case, the line element of equation (1.1) can be rewritten in rectangular coordinates as:

$$ds^2 = -dt^2 + a^2(t)\delta_{ij}dx^i dx^j, \tag{1.2}$$

where δ_{ij} is the Kronecker delta and the scale factor relates the physical ($\bar{x}_{phys}$) with the comoving ($\bar{x}$) coordinates at any time as $\bar{x}_{phys}(t) = a(t)\bar{x}$. This is the only metric that describes a uniform and isotropic distribution of matter and energy in a flat universe [27].

The evolution of the scale factor over the time is determined by the Einstein field equations:

$$\mathcal{R}_{\mu\nu} - \frac{1}{2}g_{\mu\nu}\mathcal{R} + \Lambda g_{\mu\nu} = 8\pi G T_{\mu\nu}, \tag{1.3}$$

which in turn follows from varying the Einstein-Hilbert action:

$$S_{EH} = \frac{1}{16\pi G}\int d^4x\sqrt{-g}(\mathcal{R} - 2\Lambda) + S_m \tag{1.4}$$

with respect to the metric tensor $g_{\mu\nu}$ [12]. In these expressions, $\mathcal{R}_{\mu\nu}$ is the Riemann tensor whose components are given by $g_{\mu\nu}$ and its derivatives, $\mathcal{R} = \mathcal{R}_{\mu\nu}\mathcal{R}^{\mu\nu}$ is the Ricci scalar, G is the universal gravitational constant, $T_{\mu\nu}$ is the energy momentum tensor defined from the variation of the matter action S_m of the contents of the universe, $\sqrt{-g} = det(g_{\mu\nu})$, and Λ is a cosmological constant whose presence in the equations is justified by the indeterminacy of the Einstein-Hilbert action up to an additive constant. Whether or not the current accelerated expansion of the universe is due to this constant, one of the most challenging problems of modern physics is to find the mechanism that sets Λ to its real value. We will come back to this point in chapter 2.

In order to set out the equations of motion for the scale factor, we need to know the components of the energy-momentum tensor on the right hand side of the Einstein equations. Regardless the specific properties of the constituents of the universe, the simplest form the energy-momentum tensor may assume consistent with the symmetries of the FLRW metric is given by [28]:

$$T^{\mu}_{\nu} = diag(-\rho, P, P, P), \tag{1.5}$$

which is the corresponding form of a perfect fluid. Here ρ is the energy density and P is the pressure, both quantities depending only on the time. In the standard cosmological model the contributions to ρ come from the photons (γ), neutrinos (ν), baryons (b), and the cold dark matter (c or CDM), while the dark energy density is directly related with the cosmological constant by:

$$\rho_\Lambda = \frac{\Lambda}{8\pi G}, \tag{1.6}$$

with pressure

$$P_\Lambda = -\rho_\Lambda \tag{1.7}$$

Substituting equations (1.2) and (1.5) into (1.3) we arrive at the two Friedmann equations:

$$H^2 \equiv \left(\frac{\dot{a}}{a}\right)^2 = \frac{8\pi G}{3}\rho + \frac{\Lambda}{3} \tag{1.8}$$

$$\frac{\ddot{a}}{a} = -\frac{4\pi G}{3}(\rho + 3P) + \frac{\Lambda}{3}, \tag{1.9}$$

where $H \equiv \dot{a}/a$ is known as the Hubble expansion rate and the dots stand for comoving time derivatives. Using equations (1.6) and (1.7), these expressions can be rewritten as:

$$H^2 = \frac{8\pi G}{3}\rho_t \tag{1.10}$$

$$\frac{\ddot{a}}{a} = -\frac{4\pi G}{3}(\rho_t + 3P_t), \tag{1.11}$$

where $\rho_t = \rho + \rho_\Lambda$ and $P_t = P + P_\Lambda$. Whenever is not necessary to make explicit the sum involved in ρ_t and P_t, we'll simply write ρ and P to denote the total energy density and pressure including the contribution from the dark energy. If we now take the time derative of H in equation (1.10) and substitute (1.11), we get the continuity equation:

$$\dot{\rho} + 3H(\rho + P) = 0 \tag{1.12}$$

valid for every single fluid as long as it is decoupled from the others. Taking the time derivative of H in equation (1.10) once again but now using the continuity equation, we find:

$$\dot{H} = -4\pi G(\rho + P) \tag{1.13}$$

Of course only two of these four expressions are independent and the use of any of them is often driven by the physical information it may render in a specific problem. In any case, we still need additional equations to solve for all the unknown functions we have, namely, the scale factor and the density ρ_i and pressure P_i of each one of the species i. For the cosmological constant we have $P_\Lambda = -\rho_\Lambda$ as stated in equation (1.7); for the other components the missing equations are obtained by computing the density and the pressure using the corresponding distribution functions $f_i(\bar{p})$ in the phase space [28]:

$$\rho_i = \frac{g_i}{(2\pi)^3} \int d^3p \; E f_i(\bar{p}) \tag{1.14}$$

$$P_i = \frac{g_i}{(2\pi)^3} \int d^3p \; \frac{|\bar{p}|^2}{3E} f_i(\bar{p}), \tag{1.15}$$

where g_i is the degeneracy, E the comoving energy and $\bar{p}$ is the proper momentum defined so that $E^2 = |\bar{p}|^2 + m^2$ [29]. Note that for relativistic particles (radiation), $E \simeq |\bar{p}|$ and therefore:

$$P_i \simeq \frac{1}{3} \frac{g_i}{(2\pi)^3} \int d^3p \; E f_i(\bar{p}) = \frac{1}{3} \rho_i \tag{1.16}$$

irrespective of the statistics obeyed by the particles. On the other hand, if the particles are non-relativistic (matter), that is, if the mass m is much larger than the temperature, we have [28]:

$$\rho_i = g_i m \left(\frac{mT}{2\pi} \right)^{3/2} e^{-(m-\mu)/T} \tag{1.17}$$

$$P_i = g_i T \left(\frac{mT}{2\pi} \right)^{3/2} e^{-(m-\mu)/T}, \tag{1.18}$$

where μ is the chemical potential. Since in this case $m \gg T$, the pressure of matter can be neglected. The preceding results can be summarised introducing the *equation of state* parameter w_i relating the density and the pressure as:

$$P_i = w_i \rho_i \quad \text{where} \quad w_i = \begin{cases} 1/3 & \text{radiation} \\ 0 & \text{matter} \\ -1 & \text{cosmological constant} \end{cases} \tag{1.19}$$

The classification of a particle species into matter or radiation is not always straightforward but may depend on the temperature. Photons are always relativistic whereas cold dark matter particles are non-relativistic. Electrons are relativistic at the very early universe. However, for most of the calculations we are concerned with we can regard them as matter since these calculations correspond to late time epochs when the temperature has dropped off below the mass. On the other hand, although neutrinos have a tiny non-zero mass, the constraints from earth based experiments and cosmological probes are still vague. Moreover, their contribution to the matter content of the universe is minimal in comparison with baryons and cold dark matter. Therefore, throughout our analysis we regard them as relativistic particles. So, unless otherwise stated, we regard photons and neutrinos as radiation and cold dark matter and baryons as matter.

Even if we don't solve the Friedmann equations we can use the scale factor as the time variable instead of the comoving time and see how the energy densities of the different fluids evolve. Substituting w_i into the continuity equation we find:

$$\frac{d\rho_i}{\rho_i} = -3(1+w_i)\frac{da}{a} \quad \Rightarrow \quad \rho_i(a) = \rho_{i0}\left(\frac{a}{a_0}\right)^{-3(1+w_i)}, \tag{1.20}$$

where ρ_{i0} and a_0 are the energy density and the scale factor at present. It is customary to define $a_0 = 1$ so it can be omitted in the equations:

$$\rho_i(a) = \begin{cases} \rho_{i0}a^{-4} & \text{radiation} \\ \rho_{i0}a^{-3} & \text{matter} \\ \rho_{i0} & \text{cosmological constant} \end{cases} \tag{1.21}$$

The energy density at present time is inferred from the observational data. Except for the photons and neutrinos whose density is well known —see below— from the measurements of the temperature of the Cosmic Microwave Background Radiation (CMB), the density of matter and dark energy still lack of an accurate determination, although significant progress over the last twenty years has been made using the information of the current expansion rate H_0 as well as other cosmological probes.

Figure (1.1**a**) shows the evolution of the energy densities according to equations (1.21). The content of the early universe is dominated by relativistic particles. However, since the matter dilutes slowlier it becomes the dominant component of the universe once its energy density equals the density of radiation at a_{eq}. For most of the time the dark energy density lies constant at an incredibly small value and plays no role in the expansion of the universe until late times when the matter has diluted too much. Figure (1.1**b**) shows a close-up of the transition from the matter dominated universe to the dark energy era as a funcion of the redshift z defined as:

$$1 + z = \frac{a_0}{a} = \frac{1}{a}, \tag{1.22}$$

where $z = 0$ corresponds to the present time. From equation (1.11) we see that as the dark energy becomes dominant, the therm $\rho + 3P$ goes from a positive value (ρ_m) to a negative value ($-2\rho_\Lambda$), leading to an accelerated expansion corresponding to $\ddot{a} > 0$. Therefore, we can split up the dynamical evolution of the whole universe in three main stages characterised by the dominance of a single fluid (radiation, matter, dark energy) over the others. The contribution of any species to the energy content of the universe is quantified by the *energy density parameter* Ω_i defined as:

$$\Omega_i = \frac{\rho_i}{\rho_c}, \qquad i = \gamma, \nu, b, \mathrm{CDM}, \Lambda, \tag{1.23}$$

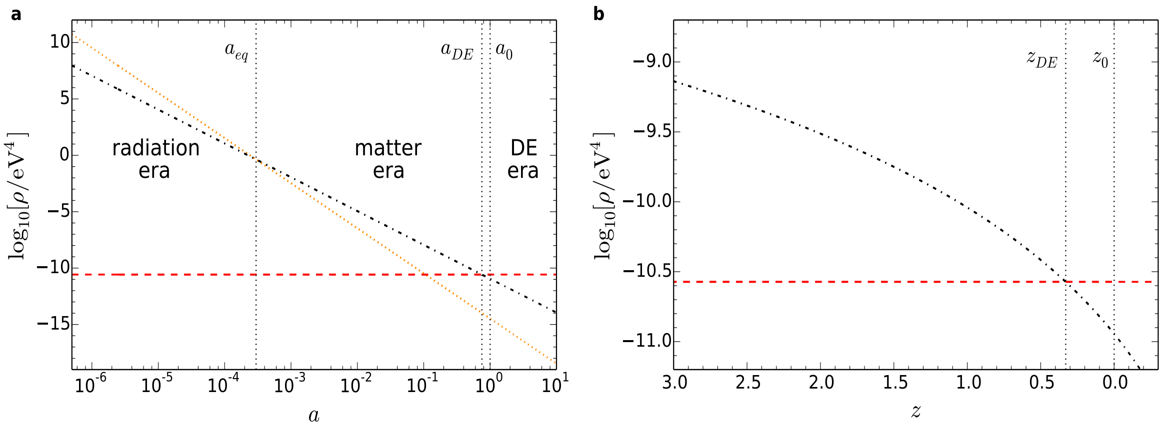

Figure 1.1: (**a**) Evolution of the energy density of radiation (dotted orange), matter (dash-dotted black) and dark energy (dashed red) in the ΛCDM model. The vertical dotted lines mark the matter-radiation equality epoch (a_{eq}), the matter-dark energy equality epoch (a_{DE}), and the present time (a_0). (**b**) Close-up of the energy density of matter and dark energy at late times. The vertical dotted lines mark the equality between matter and dark energy (z_{DE}) and the present time (z_0).

where:

$$\rho_c = \frac{3H^2}{8\pi G} \tag{1.24}$$

is the critical energy density determined by the expansion rate. In general, the curvature term contributes to ρ_c by $\rho_K(a) = -3K/(8\pi G a^2)$. However, in the case of the flat geometry we are considering, the critical density is simply the sum of the densities of all the species:

$$\rho_c = \sum_i \rho_i, \qquad i = \gamma, \nu, b, \mathrm{CDM}, \Lambda, \tag{1.25}$$

so we are lead to:

$$\Omega_r(a) + \Omega_m(a) + \Omega_\Lambda(a) = 1, \tag{1.26}$$

valid at any time, no matter which epoch we are considering. Of course well deep into the radiation era we may take $\Omega_r(a) \approx 1$ and analogously $\Omega_m(a) \approx 1$ and $\Omega_\Lambda(a) \approx 1$ in the matter and dark energy epochs, respectively. If we denote the present value of the density parameter of matter (radiation, dark energy) by Ω_m (Ω_r, Ω_Λ) and we write $\rho_i(a) = \rho_{0i} a^{-3(1+w_i)} = \Omega_i \frac{3H_0^2}{8\pi G}(1+z)^{3(1+w_i)}$ using equations (1.21), (1.22) and (1.23), the first Friedmann equation (1.10) is left as:

$$H(z) = H_0 \left[\Omega_m (1+z)^3 + \Omega_r (1+z)^4 + \Omega_\Lambda\right]^{1/2} \tag{1.27}$$

This expression lies at the heart of many calculations affecting both homogeneous an perturbed cosmological quantities.

Whereas it is easy to describe the dynamical evolution of the universe, the thermal history is quite another matter. We will review some important results in the following. As we mentioned before, the energy density of the photons and neutrinos can be inferred from the temperature of the CMB (T_γ). Solving the integral in equation (1.14) we get:

$$\rho_\gamma(a) = \frac{\pi^2}{30} g_\gamma T_\gamma^4(a) = \frac{\pi^2}{15} T_\gamma^4(a) \tag{1.28}$$

$$\rho_\nu(a) = \frac{7}{8} \cdot \frac{\pi^2}{30} g_\nu T_\nu^4(a) = \frac{7}{8} \cdot \frac{\pi^2}{5} T_\nu^4(a), \tag{1.29}$$

where we use a Bose-Einstein distribution for the photons and a Fermi-Dirac distribution for the neutrinos (in both cases with zero chemical potential [29]), $g_\gamma = 2$ accounting for the two spin states of the photon and $g_\nu = 6$ considering three massless neutrino species and their antiparticles. In any case, if we substitute equation (1.21) on the left hand side we obtain:

$$aT = const, \tag{1.30}$$

which means that the temperature redshifts as a^{-1}. Consequently, the entropy per comoving volume defined as:

$$S \equiv \frac{a^3(\rho + P)}{T} \tag{1.31}$$

remains constant. From equations (1.17) and (1.18) we see that the entropy density S/a^3 for non-relativistic particles is exponentially small:

$$\frac{\rho + P}{T} \simeq \frac{\rho}{T} = \frac{gm}{T} \left(\frac{mT}{2\pi}\right)^{3/2} e^{-(m-\mu)/T} \tag{1.32}$$

Therefore, the major contribution to the entropy content of the universe comes from the radiation. These results allow us to find the relation between the temperatures of photons and neutrinos. Before the synthesis of light nuclei takes place, electrons, positrons, heavy baryons, photons, and neutrinos were tightly coupled in thermal equilibrium via the weak and electromagnetic interactions. As the universe cools down the weak interactions become less efficient and neutrinos decouple from the plasma at a scale factor $a_{\nu dec}$ and temperature about $T_{\nu dec} \sim 1$ MeV [28]. Some time later, when the temperature of the plasma falls about to 500 keV, electrons and positrons annihilate each other but there is not enough energy for pair production, heating the photon bath further. If we consider the period between the neutrino decoupling and some time after electron-positron annihilation, entropy conservation for the barotropic fluid and neutrinos states that:

$$\frac{4}{3} \cdot \frac{\pi^2}{30} g_{\gamma e} T_{\nu dec}^3 a_{\nu dec}^3 = \frac{4}{3} \cdot \frac{\pi^2}{30} g_\gamma T_\gamma^3(a) a^3 \tag{1.33}$$

$$\frac{4}{3}\cdot\frac{7}{8}\cdot\frac{\pi^2}{30}g_\nu T^3_{\nu dec}a^3_{\nu dec}=\frac{4}{3}\cdot\frac{7}{8}\cdot\frac{\pi^2}{30}g_\nu T^3_\nu(a)a^3, \tag{1.34}$$

where $g_{\gamma e}=2+\frac{7}{8}\cdot 2\cdot 2=\frac{11}{2}$ accounting for the photons and the two spin states of electrons and positrons. Dividing these expressions we find:

$$T_\gamma(a)=\left(\frac{g_{\gamma e}}{g_\gamma}\right)^{1/3}T_\nu(a)=\left(\frac{11}{4}\right)^{1/3}T_\nu(a) \tag{1.35}$$

as expected. If we substitute this result into equation (1.29) we get:

$$\rho_\nu(a)=\frac{7}{8}\cdot\frac{\pi^2}{5}\left(\frac{4}{11}\right)^{4/3}T^4_\gamma(a)=\frac{7}{8}\cdot 3\cdot\left(\frac{4}{11}\right)^{4/3}\rho_\gamma(a), \tag{1.36}$$

which amounts to 68% the energy density of photons. At present time, the temperature of the CMB has been measured accurately $T_\gamma(a_0)=2.72548\pm 0.00057\ K$ [30] so $\rho_{\gamma 0}=2.00\times 10^{-15}$ eV^4 and $\rho_{\nu 0}=1.36\times 10^{-15}$ eV^4. Although cosmological neutrinos have evaded so far direct detection [31] they do play an important role in the synthesis of light nuclei in the early universe, the evolution of the CMB anisotropies and the late-time growth of matter perturbations [32].

1.2 Perturbations

1.2.1 Basic perturbation theory

As we stated at the beginning of this chapter, the homogeneity and isotropy of the universe are features that arise only when we average over large volumes of space. The existence of discrete sources of radiation and clustered matter even at cosmological scales means that the simplified picture we have just discussed needs to be refined to account for all the departures from homogeneity and isotropy we observe. If such departures are small it is possible to develop a linear theory to describe their evolution by considering small perturbations to the smooth background. Let's first write the perturbed metric $g_{\mu\nu}$ as a sum of the FLRW metric $\bar{g}_{\mu\nu}$ and a perturbation $h_{\mu\nu}$:

$$g_{\mu\nu}=\bar{g}_{\mu\nu}+h_{\mu\nu} \tag{1.37}$$

From now on and unless otherwise stated, a bar will denote any homogeneous quantity. Moreover, it will be convenient to introduce the conformal time τ defined as:

$$\tau=\int_0^t\frac{1}{a(t')}dt', \tag{1.38}$$

so $d\tau=dt/a(t)$. The components of $h_{\mu\nu}$ and the perturbed energy-momentum tensor $\delta T_{\mu\nu}$ can be decomposed into terms transforming as scalars, vectors, or tensors under coordinate transformations [33]. By applying differential operators to the Einstein equations we obtain separate expressions involging only scalar, vector, or tensor terms, so these components evolve independently. The crucial point is that density perturbations, which are the matter of interest of our study, only couple with the scalar terms [12, 29, 33] so we can restrict our analysis to the scalar perturbations of the metric.

The perturbation of any quantity is defined as the difference between the value it assumes in the perturbed spacetime and the value it assumes in the homogeneous background at the same coordinate values. This requires to define a coordinate transformation relating the points of these two spacetimes [34]. Note that this is not a transformation of coordinates between two different observers in the same spacetime, but a map between different spacetimes seen by the same observer [12]. Moreover, this map is not unique and the adoption of a particular choice is known as fixing the gauge. This freedom is reflected in the indeterminacy of the form of $h_{\mu\nu}$.

In the *netwonian gauge* the line element in a flat universe can be written as:

$$ds^2 = a^2(\tau)[-(1+2\Psi)d\tau^2 + (1-2\Phi)\delta_{ij}dx^i dx^j], \tag{1.39}$$

where the gravitational potential Ψ and the spatial curvature perturbation Φ are two scalar functions that depend on the time and position. The coordinate frame in this gauge is defined by attaching observers to the unperturbed comoving grid where the expansion appears isotropic. These observers measure non-zero peculiar velocities of massive particles moving on the grid and matter fluctuations grow as a result of gravitational collapse. If we split the energy-momentum tensor into its FLRW homogeneous part $\bar{T}_{\mu\nu}$ and a perturbation $\delta T_{\mu\nu}$ as in equation (1.37):

$$T_{\mu\nu} = \bar{T}_{\mu\nu} + \delta T_{\mu\nu} \tag{1.40}$$

and substitute the metric (1.39) into the Einstein field equations (1.3) retaining only the first order terms, the linear perturbed Einstein equations in Fourier space read as [35]:

$$k^2\Phi + 3\mathcal{H}(\Phi' + \mathcal{H}\Psi) = 4\pi G a^2 \delta T^0_0 \tag{1.41}$$

$$k^2(\Phi' + \mathcal{H}\Psi) = 4\pi G a^2(\bar{\rho} + \bar{P})\theta \tag{1.42}$$

$$\Phi'' + \mathcal{H}(\Psi' + 2\Phi') + \left(2\frac{a''}{a} - \mathcal{H}^2\right)\Psi + \frac{k^2}{3}(\Phi - \Psi) = \frac{4\pi G}{3}a^2\delta T^i_i \tag{1.43}$$

$$k^2(\Phi - \Psi) = 12\pi G a^2(\bar{\rho} + \bar{P})\sigma, \tag{1.44}$$

where the primes stand for conformal time derivatives, $\mathcal{H} \equiv a'/a$ is the conformal expansion rate related to H by $\mathcal{H} = aH$, k is the norm of the Fourier mode ($\bar{k} = k\hat{k}$) and the divergence of the velocity θ and the shear σ are defined respectively as:

$$(\bar{\rho} + \bar{P})\theta \equiv ik^j \delta T^0_j \tag{1.45}$$

$$(\bar{\rho}+\bar{P})\sigma \equiv -\left(\hat{k}_i\hat{k}_j - \frac{1}{3}\delta_{ij}\right)\Sigma^i_j \quad , \quad \Sigma^i_j \equiv \delta T^i_j - \frac{\delta^i_j}{3}\delta T^k_k \tag{1.46}$$

At linear order the components of the perturbed energy-momentum tensor are related to the perturbations of the density $\delta\rho = \rho(\tau,\bar{x}) - \bar{\rho}(\tau)$ and pressure $\delta P = P(\tau,\bar{x}) - \bar{P}(\tau)$ as:

$$\delta T^0_0 = -\delta\rho \tag{1.47}$$

$$\delta T^0_i = (\bar{\rho}+\bar{P})v_i = -\delta T^i_0 \tag{1.48}$$

$$\delta T^i_j = \delta P \delta^i_j + \Sigma^i_j \tag{1.49}$$

where $v^i = dx^i/d\tau$ are the components of the peculiar velocity on the expanding grid related to θ as $\theta = ik^j vj$ and $\Sigma^i_i = 0$. The terms on the right hand side of these equations include the contributions from all the components of the universe, except for the dark energy which in the ΛCDM model is assumed to be homogeneous. Just as we did when we derived the continuity equation (1.12), it turns out to be convenient to deduce also other results by combining equations (1.41)-(1.44) or by applying the energy-momentum conservation theorem:

$$\partial_\mu T^{\mu\nu} + \Gamma^\mu_{\alpha\mu}T^{\alpha\nu} + \Gamma^\nu_{\alpha\mu}T^{\mu\alpha} = 0 \tag{1.50}$$

This leads to the following equations of motion for the density contrast $\delta \equiv \delta\rho/\bar{\rho}$ and θ in Fourier space [35]:

$$\delta_i' + (1+w_i)(\theta_i - 3\Phi') + 3\mathcal{H}\left(\frac{\delta P_i}{\delta\rho_i} - w_i\right)\delta_i = 0 \tag{1.51}$$

$$\theta_i' + \left[\mathcal{H}(1-3w_i) + \frac{w_i'}{1+w_i}\right]\theta_i - \frac{\delta P_i/\delta\rho_i}{1+w_i}k^2\delta_i + k^2(\sigma_i - \Psi) = 0 \tag{1.52}$$

valid for every single fluid as long as it is decoupled from the others.

We may alternatively consider the *synchronous gauge* where the line element can be written as:

$$ds^2 = a^2(\tau)[-d\tau^2 + (\delta_{ij}+h_{ij})dx^i dx^j] \tag{1.53}$$

The scalar component of the metric perturbation h_{ij} is also determined by two functions depending on the time and position: one of them may be the trace $h = \mathrm{Tr}(h_{ij})$ while the other (η) is defined so that the conversion from the Fourier space to real space is given by [35]:

$$h_{ij}(\tau,\bar{x}) = \int d^3k e^{i\bar{k}\cdot\bar{x}}\left[\hat{k}_i\hat{k}_j h + \left(\hat{k}_i\hat{k}_j - \frac{1}{3}\delta_{ij}\right)6\eta\right] \tag{1.54}$$

In this case, the linear-order Einstein equations in Fourier space are [35]:

$$k^2\eta - \frac{1}{2}\mathcal{H}h' = 4\pi G a^2 \delta T^0_0 \tag{1.55}$$

$$k^2\eta' = 4\pi G a^2(\bar{\rho}+\bar{P})\theta \tag{1.56}$$

$$h'' + 2\mathcal{H}h' - 2k^2\eta = -8\pi G a^2 \delta T^i_i \tag{1.57}$$

$$h'' + 6\eta'' + 2\mathcal{H}(h'+6\eta') - 2k^2\eta = -24\pi G a^2(\bar{\rho}+\bar{P})\sigma, \tag{1.58}$$

while the conservation equations read as:

$$\delta_i' + (1+w_i)\left(\theta_i + \frac{1}{2}h'\right) + 3\mathcal{H}\left(\frac{\delta P_i}{\delta\rho_i} - w_i\right)\delta_i = 0 \tag{1.59}$$

$$\theta_i' + \left[\mathcal{H}(1-3w_i) + \frac{w_i'}{1+w_i}\right]\theta_i - \frac{\delta P_i/\delta\rho_i}{1+w_i}k^2\delta_i + k^2\sigma_i = 0 \tag{1.60}$$

Although the conservation equations (1.51)-(1.52) and (1.59)-(1.60) look like similar, the perturbations of the density and pressure are quantities whose value and evolution differ from gauge to gauge, which is a natural consequence of the definition of the coordinate grid in each case. In the synchronous gauge observers are usually attached to free-falling cold dark matter particles, so in this case the observers measure zero peculiar velocities of these particles and matter fluctuations grow as a result of the dilation of the coordinate grid rather than gravitational infall [36].

There are other gauges and the use of one or another is a matter or choice, but of course there are some advantages associated with each one. For example, calculations in the newtonian gauge are easier to interpret in terms of our physical intuition of the gravitational collapse, but they are more difficult to be carried out numerically than in the syncrhonous gauge. The important thing is that observable quantities are gauge independent. We may therefore take advantage of this fact and solve the equations in the synchronous gauge while analise and discuss the results in the newtonian one. In doing so, we need the convertion formulas for the density contrast and the divergence of the velocity between these gauges [35]:

$$\delta_i(new) = \delta_i(syn) - \frac{3(1+w_i)}{k^2}\mathcal{H}[3\eta' - \delta_c'(syn)] \tag{1.61}$$

$$\theta_i(new) = \theta_i(syn) - [3\eta' - \delta_c'(syn)], \tag{1.62}$$

where δ_c is the overdensity of cold dark matter. Whenever is clear which gauge we are using, we will omit the *new* and *syn* labels in δ and θ.

The specific perturbation equations for each one of the cosmological species can be derived from equations (1.51) and (1.52) or (1.59) and (1.60), depending on the gauge choice. Using the cold dark matter synchronous gauge, where $\theta_c = 0$ and $\sigma_c = 0$ [35], we first get the evolution equations of the metric potentials. From equations (1.55) and (1.56) we easily find:

$$h' = \frac{2}{\mathcal{H}}\left[k^2\eta + 4\pi G a^2 \sum_i \bar{\rho}_i\delta_i\right], \tag{1.63}$$

$$k^2\eta' = 4\pi G a^2 \left[\bar{\rho}_b\theta_b + \tfrac{4}{3}\bar{\rho}_\gamma\theta_\gamma + \tfrac{4}{3}\bar{\rho}_\nu\theta_\nu\right], \tag{1.64}$$

where we have taken into account the total contribution to δT^0_0 and $(\bar{\rho} + \bar{P})\theta$ on the right hand side. Note that δ_c is directly proportional to h as can be readily seen by substituting the constant zero equation of state w and the null pressure perturbation δP in equation (1.59):

$$\delta_c' = -\frac{h'}{2} = -\frac{a}{a'}[4\pi G a^2(\bar{\rho}_b\delta_b + \bar{\rho}_c\delta_c + \bar{\rho}_\gamma\delta_\gamma + \bar{\rho}_\nu\delta_\nu) + k^2\eta] \tag{1.65}$$

The evolution of baryons and photons is more difficult to describe since they are coupled before recombination[2], so we need to correct the corresponding perturbation equations to account for such interaction. The resulting equations for the baryons are:

$$\delta_b' = -\theta_b - \frac{h'}{2} = -\theta_b - \frac{a}{a'}[4\pi G a^2(\bar{\rho}_b\delta_b + \bar{\rho}_c\delta_c + \bar{\rho}_\gamma\delta_\gamma + \bar{\rho}_\nu\delta_\nu) + k^2\eta], \tag{1.66}$$

$$\theta_b' = -\frac{a'}{a}\theta_b + k^2 c^2_{s,b}\delta_b + \frac{a n_e \sigma_T}{R_s}(\theta_\gamma - \theta_b), \tag{1.67}$$

where $a n_e \sigma_{\mathrm{T}}(\theta_\gamma - \theta_b)/R_s$ is the interaction term with n_e the number density of free electrons, σ_{T} the Thomson cross section and $R_s \equiv 3\bar{\rho}_b/(4\bar{\rho}_\gamma)$ the baryon-to-photon energy density ratio. In the last expression, the $k^2 c^2_{s,b}\delta_b$ term where $c^2_{s,b} = \delta P_b/\delta\rho_b$ is only important for small modes (high k) and we are neglecting the baryon shear stress σ_b [35]. For the photons we have:

$$\delta_\gamma' = -\frac{4}{3}\theta_\gamma - \frac{2}{3}h' = -\frac{4}{3}\theta_\gamma - \frac{4a}{3a'}[4\pi G a^2(\bar{\rho}_b\delta_b + \bar{\rho}_c\delta_c + \bar{\rho}_\gamma\delta_\gamma + \bar{\rho}_\nu\delta_\nu) + k^2\eta], \tag{1.68}$$

$$\theta_\gamma' = k^2\left(\frac{1}{4}\delta_\gamma - \sigma_\gamma\right) + a n_e \sigma_T(\theta_b - \theta_\gamma), \tag{1.69}$$

where now the photon shear σ_γ cannot be neglected and it is determined by an infinite series of coupled equations which has to be truncated at some point depending on the desired accuracy [35]. In this respect, modern Boltzmann codes such as `CAMB` [37] implements the appropiate machinery to cope with such approximation issues. Finally, neutrinos are not coupled with the other fluids during the whole range of time where we solve the system of differential equations (nearly from Big Bang Nucleosynthesis to the present epoch). Therefore, there is no interaction term in the equations, but the shear σ_ν cannot be neglected and the same thing happens as with σ_γ. The perturbation equations in this case are:

$$\delta_\nu' = -\frac{4}{3}\theta_\nu - \frac{2}{3}h' = -\frac{4}{3}\theta_\nu - \frac{4a}{3a'}[4\pi G a^2(\bar{\rho}_b\delta_b + \bar{\rho}_c\delta_c + \bar{\rho}_\gamma\delta_\gamma + \bar{\rho}_\nu\delta_\nu) + k^2\eta], \tag{1.70}$$

---

[2] Baryons are still coupled to photons until the drag epoch z_{drag}, shortly after recombination z_*.

$$\theta'_\nu = k^2 \left(\frac{1}{4}\delta_\nu - \sigma_\nu \right) \tag{1.71}$$

Note that the density perturbation in all species are directly coupled with the synchronous potential η.

1.2.2 Initial conditions

In order to solve the system of perturbation equations we need to specify the corresponding initial conditions. One of the most challenging problems in modern cosmology is to explain where the primeval inhomogeneities came from. So far the most accepted scenario is the theory of cosmic inflation [38], which in its simplest implementation introduces a scalar field that drives the expansion of the early universe at an exponential rate $a \sim e^{Ht}$ between $10^{-36}s$ and $10^{-32}s$ after the Bang ($a = 0$). Among the pleasing results of this theory are the plausible solutions to the flatness and the horizon problems, as well as it provides a natural mechanism to generate the primeval inhomogeneities that gave rise to the anisotropies and structure we see at present. However, the occurrence of an inflationary stage in the early universe has not been unambiguously confirmed by the cosmological observations, which in this case is the only way we have to test the theory since the involved energy scales are well beyond the reach of accelerators even in the future.

For the purposes of this study, we can assume the initial conditions derived from the superhorizon approximation [35]:

$$\delta_\gamma = -\frac{2}{3}h \tag{1.72}$$

$$\delta_c = \delta_b = \frac{3}{4}\delta_\gamma = \frac{3}{4}\delta_\nu \tag{1.73}$$

$$\theta_b = \theta_\gamma = -\frac{1}{18}C(k^4\tau^3) \tag{1.74}$$

$$\theta_\nu = \frac{23 + 4R_\nu}{15 + 4R_\nu}\theta_\gamma \tag{1.75}$$

$$\sigma_\nu = \frac{4C}{3(15 + 4R_\nu)}(k\tau)^2 \tag{1.76}$$

$$h = C(k\tau)^2 \tag{1.77}$$

$$\eta = 2C - \frac{5 + 4R_\nu}{6(15 + 4R_\nu)}C(k\tau)^2, \tag{1.78}$$

where C is an arbitrary dimensionless constant and $R_\nu = \bar{\rho}_\nu/(\bar{\rho}_\gamma + \bar{\rho}_\nu)$ accounts for the contribution of neutrinos and extra relativistic species other than photons to the total content of radiation. We start solving the equations at $a_{ini} \sim 10^{-9}$ after Big Bang Nucleosynthesis, when all the modes of interest still lie outside the horizon, that is, when the corresponding length of a given mode $\lambda = 2\pi/k$ is larger than the distance d_H travelled by the light since the Bang:

$$d_H(t) = \int_0^t \frac{1}{a(t')} dt' \tag{1.79}$$

Note that $d_H(t)$ is just the conformal time τ given by equation (1.38). At these times, neutrinos are already decoupled from baryons, while these latter are tightly coupled with the photons via the Compton scattering, which isotropizes the multipole moments of the photons above the dipole, so $\sigma_\nu \neq 0$ and $\sigma_\gamma = 0$ [29, 36, 39].

The initial conditions (1.72)-(1.78) converted into the newtonian gauge are [35]:

$$\delta_\gamma = -2\Psi \tag{1.80}$$

$$\delta_c = \delta_b = \frac{3}{4}\delta_\gamma = \frac{3}{4}\delta_\nu \tag{1.81}$$

$$\theta_c = \theta_b = \theta_\gamma = \theta_\nu = \frac{1}{2}(k^2\tau)\Psi \tag{1.82}$$

$$\sigma_\nu = \frac{1}{15}(k\tau)^2\Psi \tag{1.83}$$

$$\Phi = \left(1 + \frac{2}{5}R_\nu\right)\Psi \tag{1.84}$$

$$\Psi = \frac{20C}{15 + 4R_\nu} \tag{1.85}$$

Note that the relation between the matter and radiation overdensities is the same in both gauges. Initial conditions fulfilling this relation are called adiabatic initial perturbations. The amplitude of the initial density fluctuations is the same for all the modes[3] and it depends solely on a single metric potential h or Ψ, according to the case. However, since the background density of the neutrinos is proportional to the background density of the photons (c.f. equation (1.36)), R_ν is constant and therefore Ψ is constant too. This implies that before the modes enter the horizon, matter perturbations in the newtonian gauge are frozen (keep constant) at their initial value, while they change (grow) in time in the synchronous gauge.

1.2.3 Evolution of cosmological perturbations

Figure (1.2) shows the evolution of matter perturbations (baryons + cold dark matter) in the newtonian gauge for modes entering the horizon before ($k = 1\text{Mpc}^{-1}, 0.1\text{Mpc}^{-1}$) and after ($k = 0.005\text{Mpc}^{-1}$, 0.001Mpc^{-1}) the matter-radiation equality epoch. Initially,

---

[3] In that case, the primordial spectrum is called a scale-invariant spectrum. See next section.

when all the modes are outside the horizon, δ_m is constant as we have just discussed. Then, matter perturbations start growing once the modes enter the horizon at $\tau_h = 2\pi/k$, which means that small modes (large k) cross the horizon earlier than the large modes (small k) do, as expected. Alternatively, the entry epoch is also defined in terms of the Hubble radius by solving for the scale factor in the following equation:

$$k = a_h H(a_h) \tag{1.86}$$

The growth rate of matter perturbations depends on which fluid drives the expansion. Since the baryon content of the universe is low, matter perturbations are mostly determined by the dynamics of the cold dark matter $\delta_c \approx \delta_m$. Let's then consider a simple model consisting of cold dark matter and radiation. If we neglect the anisotropic shear, equation (1.44) reduces to:

$$\Phi = \Psi \tag{1.87}$$

We have to bear in mind that this is just a rough approximation, especially if we consider equation (1.84), where $R_\nu = 0.405$ and therefore the relation between the initial potentials is $\Phi = 1.162\Psi$. The continuity equations (newtonian gauge) (1.51) and (1.52) in this case are:

$$\delta'_m = -\theta_m + 3\Phi', \tag{1.88}$$

$$\theta'_m = -\mathcal{H}\theta_m + k^2\Phi, \tag{1.89}$$

$$\delta'_r = -\frac{4}{3}\left(\theta_r - 3\Phi'\right), \tag{1.90}$$

$$\theta'_r = \frac{k^2}{4}\delta_r + k^2\Phi, \tag{1.91}$$

while the perturbed Einstein equations (1.41) and (1.42) read as:

$$k^2\Phi + 3\mathcal{H}(\Phi' + \mathcal{H}\Phi) = -\frac{3}{2}\mathcal{H}^2(\Omega_m\delta_m + \Omega_r\delta_r), \tag{1.92}$$

$$k^2(\Phi' + \mathcal{H}\Phi) = \frac{3}{2}\mathcal{H}^2\left(\Omega_m\theta_m + \frac{4}{3}\Omega_r\theta_r\right), \tag{1.93}$$

where we have used $\mathcal{H} = aH$ and equation (1.24). These two expressions can be combined into:

$$k^2\Phi + \frac{9}{2}\frac{\mathcal{H}^3}{k^2}\left(\Omega_m\theta_m + \frac{4}{3}\Omega_r\theta_r\right) = -\frac{3}{2}\mathcal{H}^2\left(\Omega_m\delta_m + \Omega_r\delta_r\right) \tag{1.94}$$

For modes well within the horizon $k \gg \mathcal{H}$, the second term on the left hand side is small compared with the other terms and therefore it can be neglected, leading to:

$$k^2\Phi = -\frac{3}{2}\mathcal{H}^2\left(\Omega_m\delta_m + \Omega_r\delta_r\right) \tag{1.95}$$

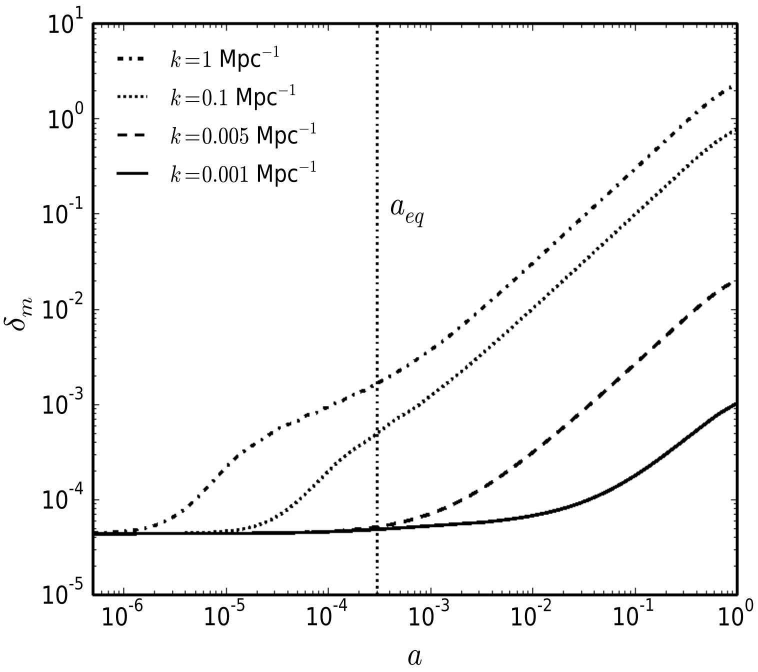

Figure 1.2: Evolution of matter overdensities (baryons + cold dark matter) in the newtonian gauge for modes entering the horizon before ($k = 1\mathrm{Mpc}^{-1}, 0.1\mathrm{Mpc}^{-1}$) and after ($k = 0.005\mathrm{Mpc}^{-1}, 0.001\mathrm{Mpc}^{-1}$) the matter-radiation epoch a_{eq} (vertical dotted line).

If we derive this result and substitute into equation (1.88) we find:

$$\delta'_m = -\theta_m - \frac{9}{2}\frac{\mathcal{H}^2}{k^2}\left(\Omega_i\delta'_i + \Omega'_i\delta_i + \frac{2\mathcal{H}'}{\mathcal{H}}\Omega_i\delta_i\right), \qquad i = m, r \tag{1.96}$$

The second term on the right hand side can be neglected by the same token, so

$$\delta'_m = -\theta_m \tag{1.97}$$

and equation (1.90) turns into:

$$\delta'_r = -\frac{4}{3}\theta_r \tag{1.98}$$

Now, if we derive equation (1.97) and substitute equations (1.89) and (1.95), we find:

$$\delta''_m + \mathcal{H}\delta'_m - \frac{3}{2}\mathcal{H}^2(\Omega_m\delta_m + \Omega_r\delta_r) = 0 \tag{1.99}$$

Following the same procedure, we derive equation (1.90) and substitute equations (1.91) and (1.95), leading to:

$$\delta_r'' + \frac{k^2}{3}\delta_r - \frac{3}{2}\mathcal{H}^2(\Omega_m\delta_m + \Omega_r\delta_r) = 0, \tag{1.100}$$

where we can neglect the third term on the left hand side, since $k \gg \mathcal{H}$:

$$\delta_r'' + \frac{k^2}{3}\delta_r = 0 \tag{1.101}$$

Equations (1.99) and (1.101) govern the growth of matter and radiation perturbations well within the horizon. The solution:

$$\delta_r(\tau) = A\cos(k\tau/\sqrt{3}) + B\sin(k\tau/\sqrt{3}), \qquad A, B = const \tag{1.102}$$

describes rapid oscillations for the modes we are considering $k\tau \gg 1$, so taking the time average we get $\langle\delta_r\rangle = 0$ and therefore equation (1.99) simplifies further to:

$$\delta_m'' + \mathcal{H}\delta_m' - \frac{3}{2}\mathcal{H}^2\Omega_m\delta_m = 0 \tag{1.103}$$

Actually, the evolution of radiation perturbations is more complex and we will review some important results in the next chapter when we consider the evidence of dark energy. The important thing is that radiation fluctuations never grow and we can study them accurately through a linear approach. During radiation domination the matter content Ω_m of the universe is negligible, so equation (1.103) reads as:

$$\delta_m'' + \mathcal{H}\delta_m' = 0 \tag{1.104}$$

Since the background density of radiation redshifts as $\bar{\rho}_r \propto a^{-4}$, from the Friedmann equation (1.10) we have $\mathcal{H} \propto a^{-1}$ and $a \propto \tau$. The solution is given by:

$$\delta_m(\tau) = A + B\ln(\tau), \qquad A, B = const, \tag{1.105}$$

which in terms of the scale factor yields:

$$\delta_m(a) = A + B\ln(a), \tag{1.106}$$

meaning that matter perturbations grow slightly during radiation dominance at a logarithmic rate $\delta_m \propto \ln a$. When the matter drives the expansion $\Omega_m \approx 1$ and now equation (1.103) reads as:

$$\delta_m'' + \mathcal{H}\delta_m' - \frac{3}{2}\mathcal{H}^2\delta_m = 0, \tag{1.107}$$

where $\mathcal{H} \propto a^{-1/2}$ and $a \propto \tau^2$. In terms of the scale factor, the solution is given by [12]:

$$\delta_m(a) = Aa^{-3/2} + Ba, \qquad A, B = const \tag{1.108}$$

The decaying solution $Aa^{-3/2}$ rapidly vanishes, so matter perturbations grow linearly as the scale factor $\delta_m \propto a$ during matter domination. This result is particularly important, since it implies that the scalar potential Φ is constant in this epoch. From equation (1.95) we have:

$$k^2\Phi = -\frac{3}{2}\mathcal{H}^2\delta_m \propto a^{-1}a \propto const \tag{1.109}$$

The transition from matter to dark energy domination at late times produces a time variation of the scalar potential ($\Phi' \neq 0$) leaving an observable imprint on the temperature anisotropy spectrum of the CMB.

Both the logarithmic and the linear growth of small-scale matter perturbations ($k \gtrsim 1\text{Mpc}^{-1}$) can be seen in the plot; large modes ($k \ll 1\text{Mpc}^{-1}$) only evolve linearly. Unlike radiation perturbations, matter overdensities grow and eventually become non-linear when their amplitude is about $\delta_m \approx 1$. At that point, the linear theory we have been discussing is not valid and we need to implement other methods to study the structures we see today. Of course, small modes reach the non-linear regime earlier than the large modes do, as they have had more time to grow since the horizon crossing. It is common to take $k_{nl} = 0.1h\text{Mpc}^{-1} \approx 0.07\text{Mpc}^{-1}$ as the limiting scale ($k < k_{nl}$) where perturbation theory provides accurate results at present time. Figure (1.3) shows the resulting matter power spectrum at $z = 0$ defined as:

$$P(k, a) = \frac{2\pi^2}{k^3}P_sT_m^2(k, a), \tag{1.110}$$

where P_s is the primordial spectrum given by the scalar spectral index n_s and the amplitude A_s as:

$$P_s = A_s\left(\frac{k}{k_0}\right)^{n_s-1}, \qquad k_0 = 0.05\text{Mpc}^{-1}, \tag{1.111}$$

and T_m is the matter transfer function that parameterizes the evolution of matter perturbations from their initial amplitude $\delta_{mi}(k)$:

$$\delta_m(k, a) = \delta_{mi}(k)T_m(k, a) \tag{1.112}$$

Actually, the primordial spectrum is not scale-invariant, but there is a very slight dependence on k, which means that the initial amplitude of matter perturbations is not the same for all the modes and it is given instead by:

$$\delta_{mi}(k) = \sqrt{A_s\left(\frac{k}{k_0}\right)^{n_s-1}}, \tag{1.113}$$

where $n_s \approx 1$. Moving from large to small scales, the matter power spectrum grows as $P \propto k^{n_s}$ reaching its maximum at k_{eq} corresponding to the mode that enters the

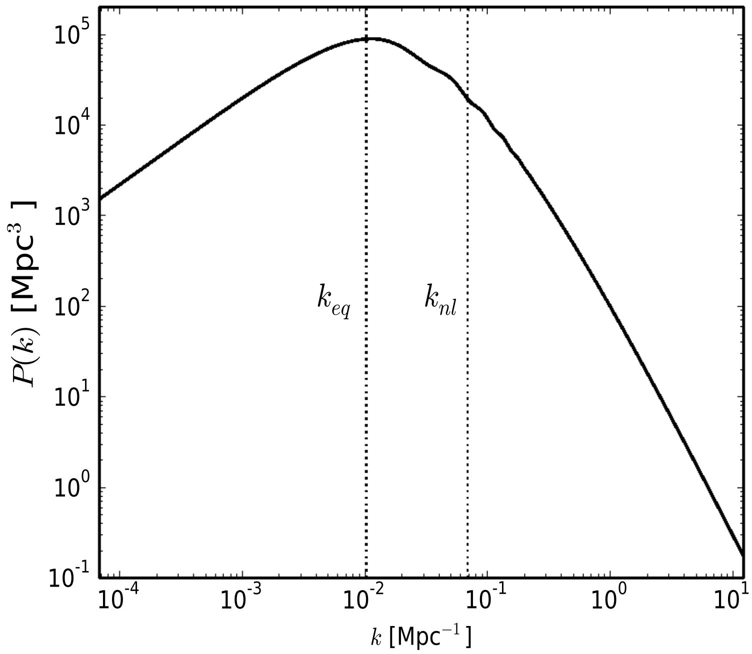

Figure 1.3: Matter power spectrum at $z = 0$ for the ΛCDM model with $\Omega_\Lambda = 0.7$ and $h = 0.68$. The vertical dotted lines mark the mode k_{eq} that enters the horizon at the matter-radiation equality epoch and the scale k_{nl} that separates the perturbative regime from the non-linear region of the spectrum, respectively.

horizon at the matter-radiation equality epoch a_{eq}, and then it decreases for large k as $P \propto k^{n_s - 4}(\ln k)^2$ [12]. We also see the scale k_{nl} that separates the perturbative regime from the non-linear part of the spectrum. Is in this region where we find the wiggles corresponding to the baryon acoustic oscillations that arise from the coupling of baryons with photons before recombination. After performing the Fourier transform of $P(k)$ [12]:

$$\xi(\bar{r}) = \frac{1}{(2\pi)^3} \int d^3k \; P(\bar{k}) e^{i\bar{k}\cdot\bar{r}}, \tag{1.114}$$

these wiggles turn into a peak in the two-point correlation function [4]:

$$\xi(\bar{r}) \equiv \langle \delta(\bar{x} + \bar{r}) \delta(\bar{x}) \rangle, \tag{1.115}$$

which measures the excess of clustering of matter at some distance $\bar{r}$.

Chapter 2

The cosmological constant problem

Unlike the introduction of dark matter in the ΛCDM model whose presence is purely justified by the observations, the simplest theoretical way to describe the dark energy is by associating it with the cosmological constant in the Einstein-Hilbert action (1.4) as we have just seen in the previous chapter. However, this standard approach leads to serious discrepancies with respect to crude estimations based on quantum field theory, so as long as particle physics does not provide a satisfactory explanation of the origin of the dark energy, this misterious component (and dark matter too) is parameterised by its contribution to the energy content of the universe at present.

In this chapter we address the cosmological constant problem. We first review in section (2.1) the evidence supporting the presence of dark energy. This evidence involves the effects of the dark energy on the background and pertubations dynamics and it has widened and strengthened over the last twenty years. Our analysis includes the luminosity distance of type Ia supernovae, the imprint of the distribution of galaxies on the baryon acoustic oscillations, the temperature anistotropy spectrum of the CMB, and consistency checks with respect to lower bounds on the age of the universe. In section (2.2) we discuss the theoretical difficulties arising when we describe dark energy as a cosmological constant. These difficulties is what motivates the quest of alternative scenarios for explaining dark energy. There has been done a lot of research on the subject whose detailed analysis is beyond the scope of this document. However, in preparation for the next chapter, we will focus on scalar field theories which initially received much attention given their natural connection with fundamental particle physics. We present a short review of these theories in section (2.3).

2.1 Evidence of dark energy

2.1.1 Type Ia Supernovae

The use of type Ia supernovae (SNeIa) as a cosmological probe is based on the fact that most of these objects show a homogeneous behaviour in terms of their spectra, light curves and peak absolute magnitudes, which makes them nearly ideal standard candles [40]. Type Ia supernovae are thought to arise from a thermonuclear explosion when a white dwarf belonging to a binary system has reached a critical mass close to the Chandrasekhar limit after accreting matter from its partner. The defining characteristic of SNeIa is the lack of hydrogen absorption lines in contraposition to the presence of a strong Si II line in the spectra. The key feature that makes them useful as distance indicators is the correlation between the absolute magnitude and the shape of the light curve [40]. This curve can be obtained by measuring the light flux over some weeks [2]. Although it remains unknown some of the physics behind SNeIa explosions, the observation of these objects provided the first quantitative evidence of an accelerating universe [2, 3].
The luminosity distance (d_L) of a source located at a comoving distance χ is defined as:

$$d_L(a) \equiv \frac{\chi(a)}{a} = \frac{1}{a}\int_a^1 \frac{1}{a'^2 H(a')} da', \tag{2.1}$$

Substituting equation (1.27) for a flat space and leaving all in terms of the redshift we have:

$$d_L(z) = \frac{1+z}{H_0}\int_0^z \frac{1}{[\Omega_m(1+z')^3 + \Omega_r(1+z')^4 + \Omega_\Lambda]^{1/2}} dz' \tag{2.2}$$

At low redshifts the expansion is driven by matter and dark energy, so we can neglect radiation and thus the luminosity distance is approximately given by:

$$d_L(z) = \frac{1+z}{H_0}\int_0^z \frac{1}{[\Omega_m(1+z')^3 + \Omega_\Lambda]^{1/2}} dz', \tag{2.3}$$

where $\Omega_m + \Omega_\Lambda = 1$. Figure (2.1) shows the dependence of d_L with z for different values of Ω_Λ. Whereas the four models lead to almost the same results in the region $z \ll 1$, as we move to higher redshifts the luminosity distance is larger as the dark energy content increases. We can explain this behaviour by expanding the integrand of equation (2.3) for low z:

$$\frac{1}{[\Omega_m(1+z')^3 + \Omega_\Lambda]^{1/2}} \simeq 1 - \frac{3}{2}\Omega_\Lambda z + \mathcal{O}(2) \tag{2.4}$$

Therefore:

$$d_L(z) = \frac{1+z}{H_0}\int_0^z \left[1 - \frac{3}{2}\Omega_\Lambda z + \mathcal{O}(2)\right] dz' = \frac{1}{H_0}\left[z + \frac{z^2}{4} + \frac{3}{4}\Omega_\Lambda z^2 + \mathcal{O}(3)\right], \tag{2.5}$$

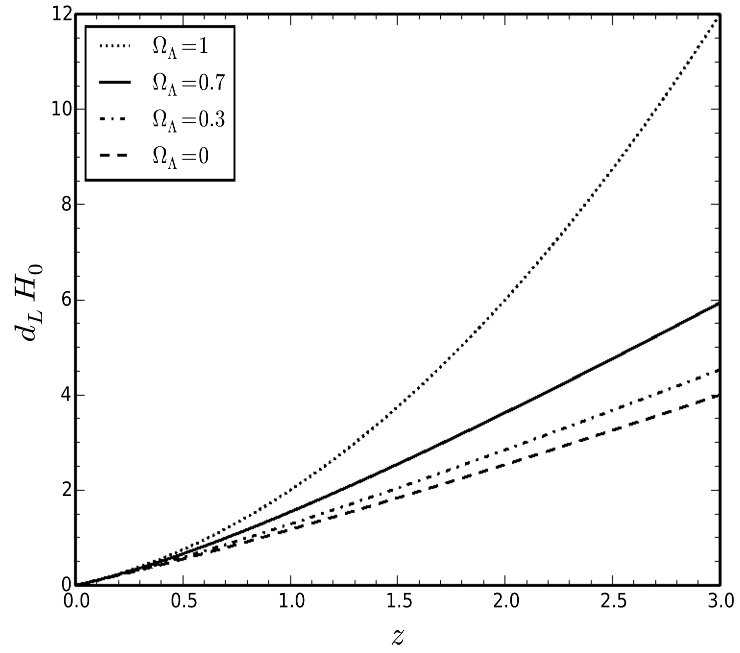

Figure 2.1: Luminosity distance (in units of H_0^{-1}) as a function of the redshift in a flat universe for different values of Ω_Λ. We have neglected the contribution from radiation, so the present matter content is given by $\Omega_m = 1 - \Omega_\Lambda$.

so the contribution from dark energy becomes important as we take larger values of Ω_Λ. The luminosity distance of SNeIa can be probed by measurements of their light fluxes $\mathcal{F}$. Both quantities are related by [17]:

$$\mathcal{F} = \frac{L_s}{4\pi d_L^2}, \tag{2.6}$$

where L_s is the intrinsic luminosity of the source. Usually the flux is expressed in terms of the apparent magnitude (m) defined as:

$$m = -\frac{5}{2}\log_{10}\mathcal{F} + c, \tag{2.7}$$

where c is a reference constant. If we substitute equation (2.6) and rename the constant after dumping into it the 4π factor we have:

$$m = -\frac{5}{2}\log_{10} L_s + 5\log_{10} d_L + c \tag{2.8}$$

Since the absolute magnitude (M) is defined as the apparent magnitude the source

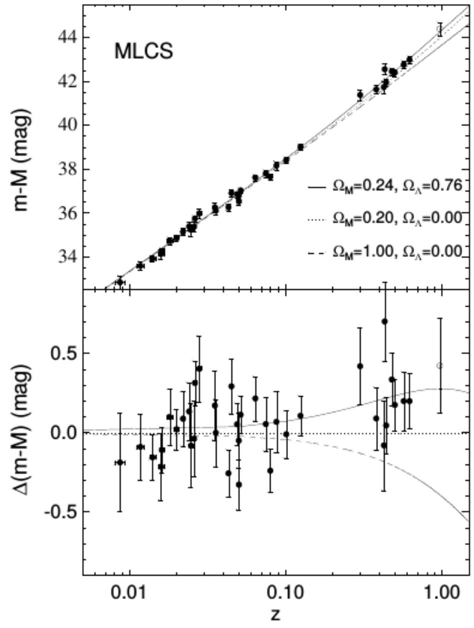

Figure 2.2: *Top.* Distance modulus of the SNeIa samples analysed by the High-z Supernova Search Team. The curves are the theoretical predictions for: the best fit for a ΛCDM model (solid), a flat Einstein-de Sitter universe with $\Omega_m = 1$, $\Omega_\Lambda = 0$ (dashed) and an open Einstein-de Sitter universe with $\Omega_m = 0.20$, $\Omega_\Lambda = 0$ (dotted). The bottom panel shows the residuals with respect to the latter. The figure has been taken from [2].

would have if it were located at 10 pc from the observer we obtain a similar relation:

$$M = -\frac{5}{2}\log_{10} L_s + 5\log_{10} 10\text{pc} + c \tag{2.9}$$

Substituting equation (2.8) into (2.9) we get:

$$\mu \equiv m - M = 5\log_{10}\left(\frac{d_L}{10\text{pc}}\right) \tag{2.10}$$

The term $m - M$ is known as the distance modulus μ. As we mentioned, for SNeIa M can be determined from the shape of the light curve. In real life it is necessary to introduce some corrections to account for the remaining variability of these objects [41]. However, the essential point is that equation (2.10) relates an observable quantity (μ) with a theoretical prediction (d_L) so in principle it is possible to discriminate cosmological models. Figure (2.2) displays the distance modulus of 50 SNeIa analysed by the High-z Supernova Search Team in 1998 together with the theoretical curves for three cosmologies [2]. The bottom panel shows the residuals with respect to an open

Einstein-de Sitter model with $\Omega_m = 0.20$ and $\Omega_\Lambda = 0$. Whereas the low-redshift measurements don't seem to favour any model, the models without dark energy are clearly inconsistent with the high-z sample, so dark energy must be introduced to fit better the whole set. The same conclusion were reached the next year by the Supernova Cosmology Project [3] and more recently by the Supernova Legacy Survey (SNLS) [42] programs. Assuming a flat ΛCDM cosmology the constraints on Ω_m have varied as the number of SNeIa increases and the observational techniques improves. Some of these constraints are: $\Omega_m = 0.287^{+0.068}_{-0.063}$ [43], $\Omega_m = 0.274^{+0.040}_{-0.037}$ [44], $\Omega_m = 0.295 \pm 0.034$ [41], which consistently point out that dark energy amounts to nearly 70% the total energy content of the universe at present.

2.1.2 Baryon Acoustic Oscillations

Baryon acoustic oscillations (BAO) are a powerful tool for probing the imprints left on the late-time distribution of matter and galaxies by sound waves in the early barotropic fluid. These waves arise from the tight-coupling between photons and baryons before recombination. Figure (2.3) presents a series of snapshots showing the propagation of the waves in comoving distance scales. During the tight copupling regime, the baryon overdensities are pulled outwards by the radiation pressure of the photons, whereas the cold dark matter is partially dragged because of gravity. Then, shortly after decoupling the baryons are released from the photons pressure at the drag epoch ($z_{\rm drag}$). This delay is because there are many more photons than baryons, so photons stop feeling the Compton interaction before the baryons do and hence they decouple firstly. The comoving distance traveled by the wave before the drag epoch is called the sound horizon and it is given by:

$$r_{\rm drag} = \int_0^{\eta_{\rm drag}} c_s(\eta) d\eta, \tag{2.11}$$

where here η denotes the conformal time, $c_s^2 = 1/[3(1+R_s)]$ is the effective sound speed squared of the barotropic fluid, and $R_s = (3/4)\rho_b(a)/\rho_\gamma(a)$. The value of $z_{\rm drag}$ is approximately[1] given by [46]:

$$z_{\rm drag} = 1291 \frac{(\Omega_m h^2)^{0.251}}{1 + 0.659(\Omega_m h^2)^{0.828}} [1 + b_1(\Omega_b h^2)^{b_2}], \tag{2.12}$$

where $b_1 = 0.313(\Omega_m h^2)^{-0.419}[1 + 0.607(\Omega_m h^2)^{0.674}]$ and $b_2 = 0.238(\Omega_m h^2)^{0.223}$, so $r_{\rm drag}$ solely depends on the present baryon and matter physical densities $\omega_b \equiv \Omega_b h^2$, and $\omega_m \equiv \Omega_m h^2$, respectively.

---

[1] This fitting formula is inaccurate by some percentage points so in precision calculations $z_{\rm drag}$ is determined numerically by solving for the time $\eta_{\rm drag}$ when the drag optical depth equals one: $\tau_{\rm op}(\eta_{\rm drag}) = \int_{\eta_0}^{\eta_{\rm drag}} \dot{\tau}_{\rm op}/R_s = 1$ [26, 45]. For the present discussion such refinement is not required.

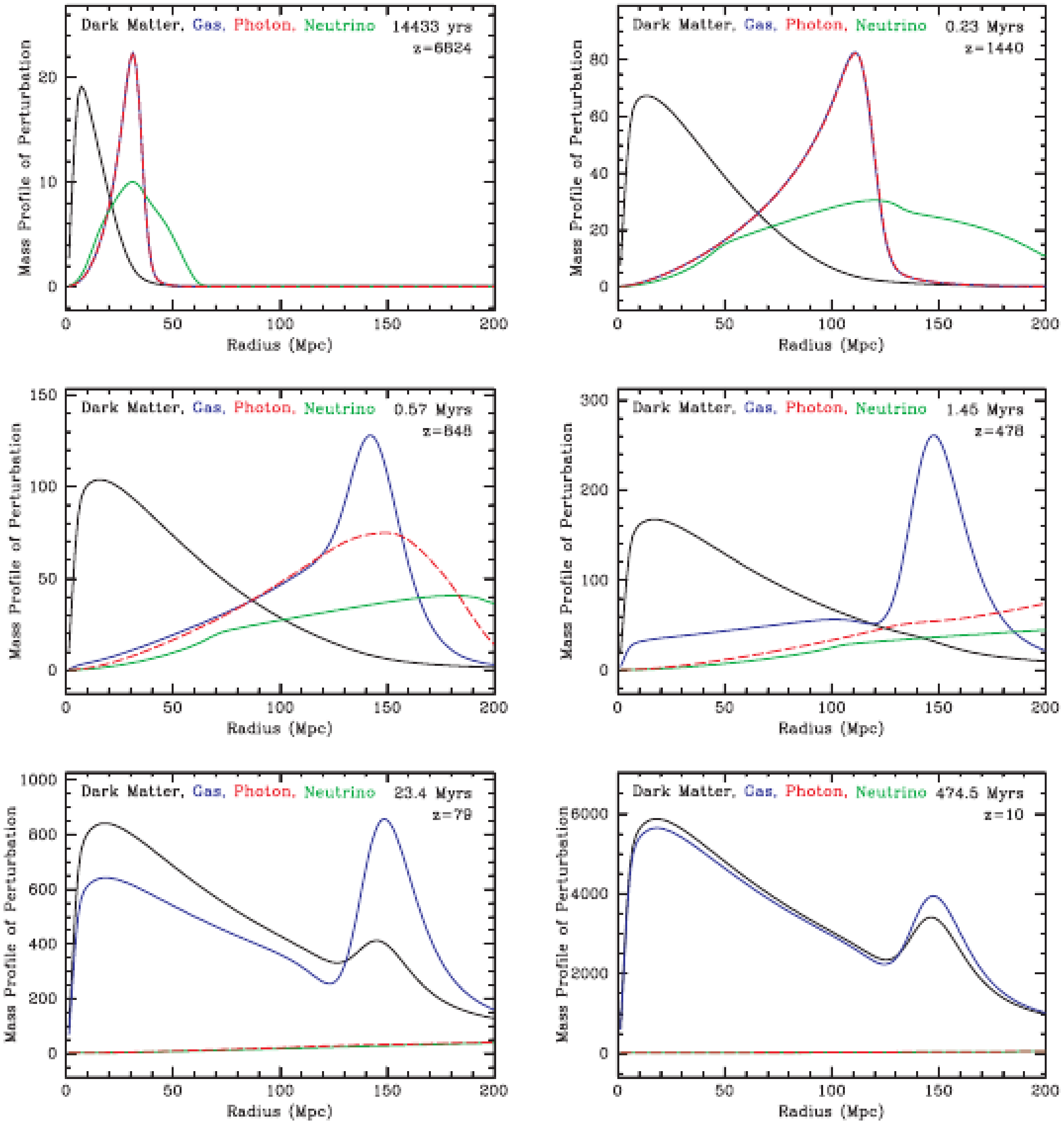

Figure 2.3: Propagation of acoustic waves in the early barotropic fluid and the generation of the BAO signature. The panels show the mass profile $\sim r^2\delta$ versus the comoving radius of initially pointlike overdensities located at the origin for each species: baryons (blue), CDM (black), photons (red), and neutrinos (green). The units of the mass profile are arbitrary. The time after the bang and the corresponding redshift of each snapshot is indicated. *Top.* At early times baryons and photons are tightly coupled. The radiation pressure of the photons pulls the wave outwards, while the CDM is indirectly dragged by gravity. *Middle.* After the drag epoch baryons decouple from photons: whereas the photon wave continues leaking away, the baryon shell stops propagating at $r_{\rm drag} \approx 150$ Mpc. *Bottom.* Once the pressure of the photons is absent gravitational instability takes over. Structure formation is expected near the origin but also at $r_{\rm drag}$. This picture has been taken from [47].

Once the baryons are decoupled from the photons the matter (baryons + CDM) overdensities are completely subject to the gravitational interaction. Matter finally clusters around the origin of the initial perturbations but there is a remnant of the early wave located at r_{drag}. When we map the distribution of galaxies in the late-time universe we expect to see a peak in the pair correlation function at r_{drag} and this is precisely what the Sloan Digital Sky Survey (SDSS) and the 2dF Galaxy Redshift Survey (2dFGRS) detected for the first time in 2005 [4, 5]. The permanence of the BAO signal at low redshifts makes this characteristic length scale a standard ruler with which is possible to constrain cosmological parameters. If we map a sample of galaxies around some redshift z, the angular size $\Delta\theta$ and the redshift separation $\Delta z_{\shortparallel}$ along the line-of-sight direction of the BAO length scale is given by [48]:

$$\Delta\theta = \frac{r_{\text{drag}}}{(1+z)D_A(z)}, \qquad \Delta z_{\shortparallel} = r_{\text{drag}} H(z), \tag{2.13}$$

where $D_A(z)$ is the angular diameter distance related with the luminosity distance by:

$$D_A(z) = \frac{d_L(z)}{(1+z)^2} \tag{2.14}$$

This relation is valid whether or not the universe is flat or the radiation content is neglected at late times as in equation (2.3) [12]. So far galaxy surveys are not large enough to measure the angular and the radial separation of the BAO length scale separately [49]. The data can constrain the quotient

$$r_{\text{BAO}}(z) = \frac{r_{\text{drag}}}{D_V(z)}, \tag{2.15}$$

where $D_V(z)$ is a geometrical mean of the radial and the two transverse directions:

$$D_V(z) \equiv \left[(1+z)^2 D_A^2(z) \frac{z}{H(z)}\right]^{1/3} \tag{2.16}$$

Figure (2.4) shows the BAO ratio has a function of the redshift for three flat cosmologies $\Omega_m + \Omega_\Lambda = 1$. We include the measurements of the BOSS-DR12 survey at $z = 0.32$ and $z = 0.57$ [50], the measurement of the 6dF Galaxy Survey at $z = 0.106$ [51], the measurement of the SDSS-DR7 survey at $z = 0.15$ [52], and the results of the WiggleZ Dark Energy Survey at $z = 0.44$, 0.6, and 0.73 [53]. Clearly the Einstein-de Sitter model with no dark energy is inconsistent with the data. The same thing happens for a model with about 5% of baryon content and the rest in the form of dark energy with no dark matter. BAO measurements can be combined with CMB information to constrain other cosmological parameters. Since r_{drag} solely depends on ω_m and ω_b and these two parameters can be inferred from the height and shape of the first acoustic peaks of the CMB spectrum [49], it is possible to obtain r_{drag} alone. Substituting r_{BAO} and r_{drag} in

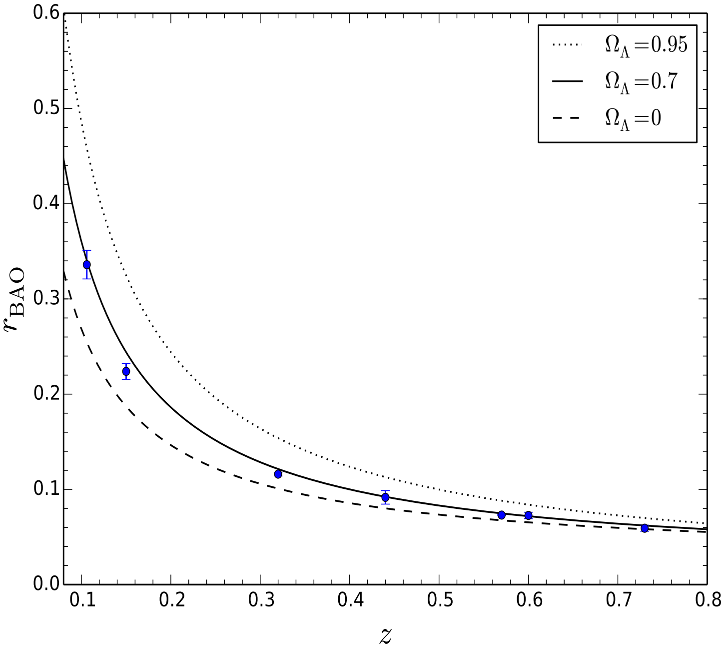

Figure 2.4: BAO ratio as a function of the redshift in a flat universe ($\Omega_m + \Omega_\Lambda = 1$) for three different values of Ω_Λ. The points are the measurements of the BOSS-DR12 galaxy survey at $z = 0.32$ and $z = 0.57$ [50], the 6dF Galaxy Survey at $z = 0.106$ [51], the SDSS-DR7 survey at $z = 0.15$ [52], and the WiggleZ Dark Energy Survey at $z = 0.44$, 0.6, and 0.73 [53]. In this plot $h = 0.7$ and $\omega_b = 0.0224$.

equation (2.15) we can solve for D_V and thus constrain the parameters embedded in $H(z)$. The results of this joint analysis made by the Planck collaboration for the ΛCDM model are $\Omega_m = 0.310 \pm 0.008$ and $H_0 = (67.6 \pm 0.6)$ km s^{-1} Mpc^{-1} [26]. As in the case of SNeIa the present content of dark energy is about 70%.

2.1.3 CMB anisotropies

Even though radiation fluctuations do not grow appreciably with time, the most accurate source of cosmological information comes from the anisotropies of the CMB. The shape of the power spectrum is affected by phenomena that took place at recombination, when free electrons were captured by atomic nuclei, and long time after, when reionization happens and the dark energy took over the expansion of the universe. As far as our research is concerned, the imprints of the dark energy on the CMB is reflected in the location of the acoustic peaks and in the low multipole region of the spectrum corresponding to large angular scales. Here we quote some important results.

Since the energy density of the photons depends on the temperature[2] $\rho \propto T^4$, the anisotropies manifest as temperature fluctuations δT, which depend on the time, the position ($\bar{x}$) and also on the momentum ($\bar{p}$) inasmuch the interaction term between photons and baryons before recombination depends on $\bar{p}$ too. Actually, the dependence of δT on the momentum is only through its direction $\hat{p}$, since the magnitude of the momentum is approximately conserved in Compton scattering [12, 29, 39]. If we define the fractional fluctuation:

$$\Theta(\tau,\bar{x},\hat{p}) \equiv \frac{\delta T}{T}, \tag{2.17}$$

the perturbed distribution function of the photons is given by:

$$f(\tau,\bar{x},\hat{p}) = \left[exp\left\{ \frac{p}{T(\tau)[1+\Theta(\tau,\bar{x},\hat{p})]} \right\} - 1 \right]^{-1} \tag{2.18}$$

The evolution of Θ is determined by the Boltzmann equation:

$$\frac{\partial f}{\partial \tau} + \frac{\partial f}{\partial x^i}\frac{dx^i}{d\tau} + \frac{\partial f}{\partial p}\frac{dp}{d\tau} + \frac{\partial f}{\partial \hat{p}^i}\frac{d\hat{p}^i}{d\tau} = C[f], \tag{2.19}$$

where $C[f]$ is the interaction term, and the fourth term on the left hand side can be neglected at first order [29]. The resulting equation of motion in Fourier space is [12, 29, 36, 54]:

$$\Theta' + ik\mu\Theta = \Phi' - ik\mu\Psi - \tau'_{op}[\Theta_0 - \Theta + \mu v_b], \tag{2.20}$$

where $\mu \equiv \hat{k}\cdot\hat{p}$, v_b is the velocity of the baryons, and Θ_0 is the monopole of Θ defined by the expansion in Legendre ($\mathcal{P}_l$) series:

$$\Theta_l = \frac{1}{(-i)^l}\int_{-1}^{1}\frac{d\mu}{2}\mathcal{P}_l(\mu)\Theta(\mu), \qquad l = 0,1,2,... \tag{2.21}$$

Before recombination the isotropizing effect of the Compton scattering washes out all the multipole moments above the dipole Θ_1 [39], so the anisotropies during this epoch are well described only by Θ_0 and Θ_1. Once the photons decouple from the baryons they stream freely across the universe and now the higher multipoles start evolving. It can be shown [29, 54] that the multipoles at the present time (τ_0) can be approximately given by the monopole and the dipole momenta at recombination (τ_*) by:

$$\begin{aligned} \Theta_l(\tau_0,k) \simeq\ & [\Theta_0(\tau_*,k) + \Psi(\tau_*,k)]j_l[k(\tau_0-\tau_*)] \\ & +3\Theta_1(\tau_*,k)\left\{ j_{l-1}[k(\tau_0-\tau_*)] - \frac{(l+1)j_l[k(\tau_0-\tau_*)]}{k(\tau_0-\tau_*)} \right\} \\ & + \int_0^{\tau_0} d\tau\ e^{-\tau_{op}}[\Psi'(\tau,k) - \Phi'(\tau,k)]j_l[k(\tau_0-\tau)], \end{aligned} \tag{2.22}$$

---

[2] For the sake of clarity in the notation, we omit the γ subindex in this section.

where j_l is the spherical Bessel function of order l. When we perform a map of the sky, we don't measure these multipole moments $\Theta_l(\tau_0, k)$, but temperature variations between different spots label by the direction $\hat{p}$ of the incoming photons. The fractional fluctuations of equation (2.17) can be expanded in spherical harmonics series:

$$\Theta(\tau, \bar{x}) = \sum_{l=1}^{\infty} \sum_{m=-l}^{l} a_{lm}(\tau, \bar{x}) Y_{lm}(\hat{p}), \tag{2.23}$$

where the entire collection of coefficients a_{lm} contain the same information as Θ. Actually, what we really measure is the variance C_l^{TT} of such coefficients at τ_0:

$$\langle a_{lm} a^*_{l'm'} \rangle = \delta_{ll'} \delta_{mm'} C_l^{TT}, \tag{2.24}$$

where C_l^{TT} is related to the multipole moments in Fourier space $\Theta_l(\tau_0, k)$ by [12]:

$$C_l^{TT} = \frac{2}{\pi} \int_0^{\infty} dk\ k^2 |\Theta_l(k)|^2 \tag{2.25}$$

Figure (2.5) shows the power spectrum $D_l \equiv l(l+1)C_l^{TT}/(2\pi^2)$ for three flat ΛCDM cosmologies $\Omega_m + \Omega_\Lambda = 1$ together with the 2015 measurements of the Planck satellite [26]. In all cases the baryon density is the same $\Omega_b = 0.05$, but the content of cold dark matter varies as $\Omega_c = \Omega_m - \Omega_b$. The relative heights of the peaks depend on the difference between the amount of cold dark matter and baryons [36], so they are not of our primary interest here. On the contrary, we note that the more content of dark energy we have, the more shifted to the right the peaks are. This is simply because the location of the peaks is given by [12, 36, 55]:

$$l_n = \frac{n\pi}{2r_s(z_*)}(1+z_*)D_A(z_*), \qquad n = 1, 2, 3, ... \tag{2.26}$$

Since $D_A \propto d_L$ as stated in equation (2.14), and since d_L increases for large Ω_Λ as shown in figure (2.1), then l_n increases for large Ω_Λ. We see that regardless of the amplitude of the oscillations, the model with low content of dark energy is inconsistent with the measurements of the location of the peaks. If we now take into account the height of the peaks, the preferred scenario corresponds to Ω_Λ to be around 0.7.

As we mentioned before, the other effect of dark energy on the spectrum manifests at low multipoles. This effect comes from the last term on the right hand side of equation (2.22) and it is known as the Integrated Sachs-Wolfe effect (ISW) [56]. The asymptotic behaviour of the Bessel function makes this term relevant only for low$-l$ [12, 29]. If we neglect the time lapse of radiation domination and if we consider a universe made only of matter, this term would be zero since in that case the potentials Φ and Ψ would be constant as we showed in equation (1.109) of section (1.2.3). On the other hand, if the dark energy content of the universe is small, the contribution from the ISW term

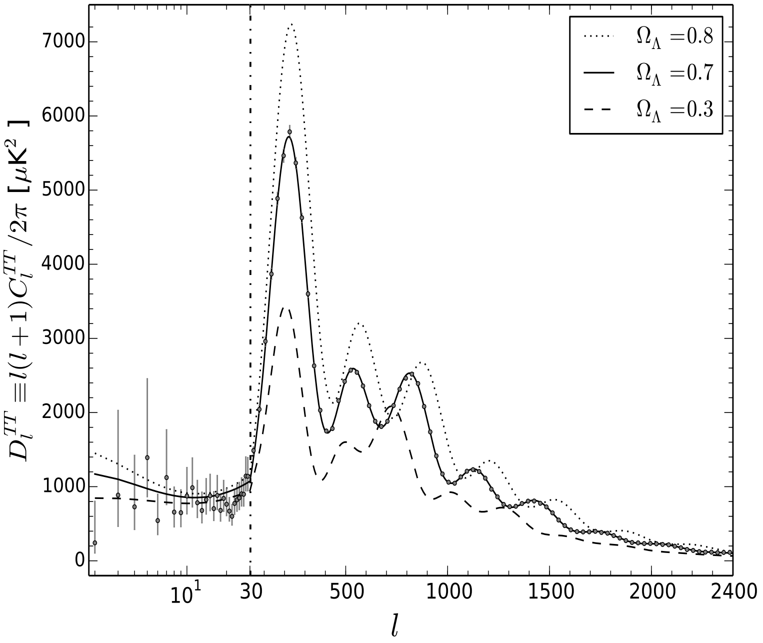

Figure 2.5: CMB temperature anisotropy spectrum for three ΛCDM flat cosmologies $\Omega_m + \Omega_\Lambda = 1$. The baryon content in all cases is the same $\Omega_b = 0.05$. The grey dots correspond to Planck 2015 data [26]. We use a logarithmic scale for multipoles between $2 \leqslant l \leqslant 30$ and then a linear scale for higher multipoles.

is also small and the spectrum is suppressed, as shown in the plot. However, in this case it is not possible to discriminate between these models, since the error bars due to the cosmic variance are large enough to embrace the curves of the three models. Nevertheless, despite this intrinsic limitations, it has been possible to detect the ISW effect by cross-correlating the CMB anisotropies with tracers of matter distribution [6–9, 57]. Therefore, a universe without dark energy is clearly inconsistent with the positive detection of the ISW effect.

2.1.4 Age of the universe

Although the age of the universe (t_0) is not an observable quantity, it is possible to determine lower bounds based on the estimated ages of the oldest astronomical objects, so any cosmological model must be consistent with these bounds. Table 2.1 quotes the age of some metal-poor stars and globular clusters (GC) in our galaxy. Despite the size of the uncertainties, we see that most estimations place t_0 above 10 Gyr.

Table 2.1: Estimated age of some old stars and globular clusters in the Milky Way.

type of object	name	age (Gyr)
star	CS 31082-001	14.1 ± 2.5 [58]
	BD +17°3248	13.8 ± 4 [59]
	HD 221170	11.7 ± 2.8 [60]
GC	various	12.9 ± 2.9 [61]
	M4	12.7 ± 0.7 [62]

The age of the universe can be calculated from the definition of the expansion rate (H):

$$t_0 = \int_0^{a_0} \frac{1}{aH(a)} da = \int_0^{\infty} \frac{1}{(1+z)H(z)} dz \tag{2.27}$$

Substituting equation (1.27) we have:

$$t_0 = \frac{1}{H_0} \int_0^{\infty} \frac{1}{(1+z)[\Omega_m (1+z)^3 + \Omega_{r0}(1+z)^4 + \Omega_\Lambda]^{1/2}} dz \tag{2.28}$$

We can neglect the contribution from radiation since at low redshifts the expansion is driven by matter and dark energy. On the other hand, at high redshifts (i.e. $z \gtrsim z_{eq}$) $1/\Omega_r(1+z)^4 \ll 1$ and hence the time elapsed during the radiation domination epoch only amounts to a negligible fraction of t_0. We have then:

$$t_0 \simeq \frac{1}{H_0} \int_0^{\infty} \frac{1}{(1+z)[\Omega_m (1+z)^3 + \Omega_\Lambda]^{1/2}} dz \tag{2.29}$$

Let's first consider an Einstein-de Sitter universe where $\Omega_m = 1$ and $\Omega_\Lambda = 0$. Equation (2.29) leads to:

$$t_0^{\mathrm{EdS}} = \frac{2}{3H_0} \tag{2.30}$$

Using a loose constraint $H_0 = 72 \pm 6$ km·s^{-1}Mpc^{-1}, the age of the universe without a cosmological constant lies in the range 8.36 Gyr $< t_0^{\mathrm{EdS}} <$ 9.88 Gyr. This range falls below the ages of the globular clusters listed in table (2.1). The discrepancy is small but in order to get $t_0^{\mathrm{EdS}} \geqslant 10$ Gyr it is needed to have $H_0 \leqslant 65.23$ km·s^{-1}Mpc^{-1}, which is not favoured by local measurements of H_0 [63], [64]. The inclusion of the dark energy as a cosmological constant solves this problem since it allows to get larger values of t_0. In this case equation (2.29) leads to:

$$t_0^{\Lambda} = \frac{2}{3H_0} \left[\frac{1}{\sqrt{\Omega_\Lambda}} \mathrm{arcsinh} \sqrt{\frac{\Omega_\Lambda}{\Omega_m}} \right], \tag{2.31}$$

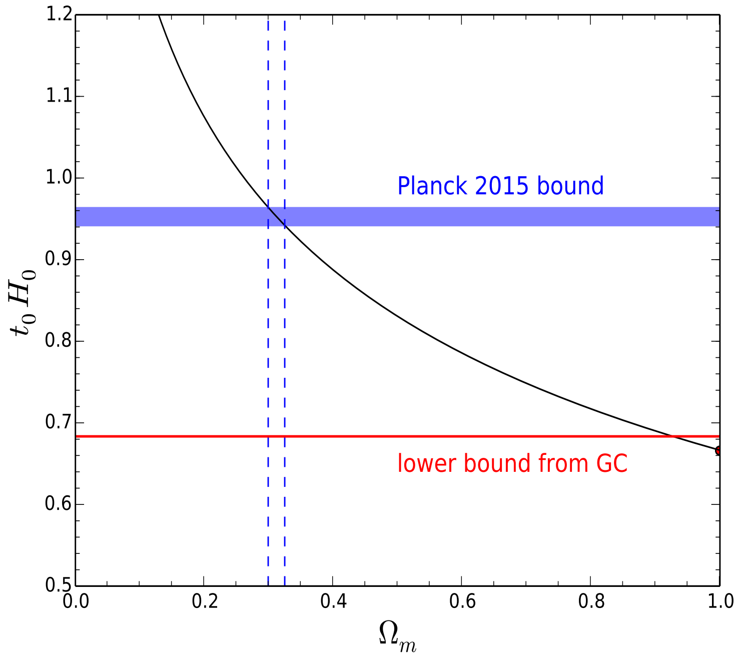

Figure 2.6: Age of the universe in units of H_0^{-1}. We include the lower bound set by the globular clusters and the Planck-2015 constraints for the base ΛCDM model [26]. The vertical dashed lines mark the constraints on Ω_m which yield a cosmic age consistent with Planck data, while the red circle at $\Omega_m = 1$ marks the prediction for the Einsten-de Sitter universe.

where $\Omega_m + \Omega_\Lambda = 1$. Note that $t_0^\Lambda \to t_0^{\text{EdS}}$ when $\Omega_m \to 1$, while $t_0^\Lambda \to \infty$ when $\Omega_m \to 0$, so it is now possible to find proper values of Ω_m that yield a cosmic age consistent with the bounds of table (2.1). Figure (2.6) shows the plot of t_0^Λ as a function of Ω_m. When we take into account the Planck-2015 constraints $t_0 = 13.807 \pm 0.026$ Gyr and $H_0 = 67.51 \pm 0.64$ km·s^{-1}Mpc^{-1} [26] for the ΛCDM model, the current matter density given by equation (2.31) lies in the range $0.300 < \Omega_m < 0.326$.

2.2 The cosmological constant problem

We have seen the necessity of introducing the cosmological constant term in the Friedmann equations to describe the observational evidence. Actually, the ΛCDM model is so successful not only because it fits the data, but also because the constraints obtained from independent observations are consistent each other. This is of the utmost importance, since in cosmology the consistency is often the only way we have to test a model.

For this reason, ΛCDM is also referred to as the concordance model. However, some problems arise when we consider the physical origin of Λ. From the point of view of the general theory of relativity, there is no special reason to keep this term or drop it from the equations. It is then a free parameter whose value (or equivalently ρ_Λ, c.f. equation (1.6)) is determined from observations [11]. Since the universe is dominated by the dark energy at late times, ρ_Λ is approximately given by:

$$\rho_\Lambda^{obs} \approx \frac{3H_0^2}{8\pi G} \sim 10^{-47}\text{GeV}^4, \tag{2.32}$$

where we have used (1.10) and $H_0 \approx 70\ \text{km} \cdot \text{s}^{-1}\text{Mpc}^{-1}$. If we now consider quantum field theory, Lorentz invariance implies that the contribution to the energy-momentum tensor due to the zero-point (vacuum) energy of all the fields present in the universe must be of the form [10]:

$$T_{\mu\nu}^{vac} = -\rho_{vac} g_{\mu\nu}, \tag{2.33}$$

where ρ_{vac} is constant [11]. Comparing this result with equation (1.3) we conclude that Λ must be somehow related to ρ_{vac}. Moreover, ρ_{vac} can be estimated through [12, 17]:

$$\rho_{vac} = \frac{1}{2}\int_0^{k_{cut}} \frac{d^3k}{(2\pi)^3}\sqrt{k^2+m^2} \simeq \frac{k_{cut}^4}{16\pi^2}, \tag{2.34}$$

where k_{cut} ($\gg m$) is some cut-off scale. Here is where the first problem arises. If we take the cut-off scale to be any characteristic scale in nature such as the Planck scale $k_{\text{Pl}} = m_{\text{Pl}} \sim 10^{19}$ GeV, the electroweak scale $k_{\text{EW}} \approx 246$ GeV, or the QCD scale $k_{\text{QCD}} \approx 200$ GeV, the estimations we get are well beyond ρ_Λ^{obs}: $\rho_{vac}(k_{\text{Pl}}) \sim 10^{74}$ GeV^4, $\rho_{vac}(k_{\text{EW}}) \sim 10^8$ GeV^4, and $\rho_{vac}(k_{\text{QCD}}) \sim 10^{-2}$ GeV^4, respectively. This discrepancy clearly indicates that the zero-point energy is not the only mechanism behind Λ, but there must be other phenomena leading to the almost complete cancellation of the vacuum energy from ρ_{vac} to the observed value ρ_Λ^{obs}. *The fine-tuning problem* of the ΛCDM model just refers to the lack of a natural explanation of the hidden mechanism producing this cancellation.

The question of the origin of the cosmological constant gets worse if we recall the evolution of the energy density of the contents of the universe as shown in figure (1.1**a**). Since ρ_Λ keeps constant over the time (c.f. equation (1.21)), it seems very unnatural that among all the infinite possibilities, the value of ρ_Λ realised in nature is just the one that equals ρ_m at late-times. *The coincidence problem* refers to the lack of a natural explanation of why the universe has just entered the dark energy domination age.

These two difficulties might suggest that although ΛCDM is so successful fitting the observations, the model is just a parametric description of the universe awaiting to be embraced by a deeper theoretical framework. From this point of view, dark energy is not due to a cosmological constant, but it is due to to a still unknown mechanism. We note that even if we drop Λ from our equations, the issue of the cancellation of the vacuum energy still remains as one of the most challenging problems of theoretical physics and indeed this question has been addressed long before the discovery of the accelerated expansion of the universe at the end of the XX century. In this regard, the model we propose here has nothing new to say.

2.3 Scalar field theories

Among the proposed alternatives to the cosmological constant, scalar field theories receive special attention because of the possibility of explaining dark energy from first principles through physics beyond the Standard Model [17, 65]. After all, if dark energy and dark matter turned out to be real fluids, we would expect to find a particle physics description of them. Early research on cosmological scalar fields as dark energy candidates dates back to the late 1980's [66–68]. However, despite much of the phenomenology was studied in the following years [69–75], it has been only possible to constrain these models until recently [76–79], thanks to the growing amount of observational evidence and the diversification of the cosmological probes. Scalar field theories aimed to describe dark energy are generically called quintessence models.

In the simplest implementation of quintessence [80, 81], we replace the cosmological constant term in the Einstein-Hilbert action (1.4) by the minimally coupled lagrangian:

$$\mathcal{L} = \frac{1}{2} g^{\mu\nu} \partial_\mu \varphi \partial_\nu \varphi + V(\varphi), \tag{2.35}$$

where the functional form of the potential $V(\varphi)$ might be justified by some theoretical model. Unlike the cosmological constant, the equation of state of the scalar field (w_φ) varies over the time. Quintessence potentials are roughly classified into freezing or thawing potentials, depending on the way w_φ approaches to -1 at late times [80]. In any case, there are three conditions that must be fulfilled [67]:

(i) The energy density of the scalar field in the early universe has to be small so that Big Bang Nucleosynthesis constraints are not spoiled.

(ii) There has to be a long enough epoch of matter dominance to allow structures to be formed.

(iii) The scalar field must roll slowly $\dot{\varphi} \ll V$ at late times to ensure a dark energy behaviour ($w_\varphi \approx -1$).

Moreover, it has been shown [70, 72] that some kind of potentials possess attractor solutions, where the dark energy evolution is not sensitive to the initial conditions. This is a nice result since the energy scales of the theories on which these models are built on are well beyond the reach of particle accelerators and therefore we can't be pretty sure on the physical conditions when the scalar field starts evolving. The low sensitivity on the initial conditions could be also a possible answer to the coincidence problem, since in this case the universe is now dominated by dark energy because it is old enough to reach the attractor solution. However, we have to be aware that coincidence might arise when selecting the values of the parameters of the potentials.

Here we present a dark energy model with an inverse power law potential $V \sim \varphi^{-n}$. Quintessence models of this kind have been extensively studied and constrained [66, 72, 76, 77, 79]. Nevertheless, we point out that in most analyses the scalar field is a fundamental entity present over the whole history of the universe, that is, its existence is justified by the same reason that of the photons and the other components. On the contrary, in our model the scalar field arises from a phase transition that tooks place at some point after the Big Bang Nucleosynthesis epoch; before that, the field is absent. Therefore, the physical interpretation, the cosmological consequences, and the constraints on the parameters are quite different in both scenarios.

Chapter 3

The Bound Dark Energy Model

In order to be considered as a viable alternative to ΛCDM, any dark energy model must not only fulfil consistency with the observations, but the model also has to avoid the naturalness and coincidence problems as well as being based on theoretical foundations [72]. In this work, we show that the Bound Dark Energy model (BDE) satisfies all these requirements. The core idea of the model is to describe the origin of dark energy as a phase transition phenomenon very often found in high energy physics. The basic picture is the following [20–23]. We introduce a hidden non-Abelian dark gauge group with very light particles that interact with the Standard Model (SM) only through gravity. Initially, the gauge coupling of the dark group is small at high energies, so the dark particles are free and its energy density redshifts as radiation. Then, as the universe expands and the temperature drops off, the dark interaction becomes strong and now the dark particles bind together forming composite states as is the case in the strong interaction, where hadrons form as a result of the non-perturbative dynamics of the elementary quarks. The lightest composite state corresponds to a scalar meson represented by a scalar field φ with an effective inverse power law potential $V = \Lambda_c^{4+\alpha}\varphi^{-\alpha}$, where the condensation energy scale Λ_c, the exponent of the potential α, the condensation epoch a_c, and the initial conditions of the scalar field are quantities derived from the parameters of the dark group and other high-energy characteristic quantities. *Dark energy corresponds to this light scalar particle formed at the phase transition undergone by the dark group when the gauge coupling becomes strong.*

In this chapter we present the Bound Dark Energy model focusing on its cosmological aspects rather than on its high-energy physics theoretical foundations, which are fully explained in [20–23]. In section (3.1) we describe the evolution of the dark group before the dark particles condense into the scalar meson φ. Then, in section (3.2) we review the physical mechanism leading to the scalar field potential, and finally we explore the evolution of homogeneous dark energy and its perturbations in sections (3.3) and (3.4), respectively.

3.1 Before the phase transition

The dark energy model we study introduces a supersymmetric hidden dark group $SU(N_c)$ with N_c colours and N_f elementary massless fields in its fundamental representation [20–23]. These colours and flavours have the same fundamental status than the colours and flavours of the gauge groups of the Standard Model (SM), in the sense that they are quantities not derived from a more fundamental theory. We assume gauge coupling unification of all the groups at the unification scale Λ_{gut} as expected from string theory. Below this scale, the dark group and the SM particles interact only via gravity. The possible values of N_c and N_f were extensively explored in [22, 23]. Using the limited observational evidence available at that time and imposing the gauge coupling unification constriction, the preferred model has $N_c = 3$ and $N_f = 6$ [22]. We take these values as the input parameters of our model.

Before the condensation, when the coupling strength of the dark group is weak, the fields of the dark group contribute to the total content of radiation of the universe so its energy density redshifts simply as $\rho_{\rm DG} \propto a^{-4}$. In terms of the degrees of freedom $g_{\rm DG}$ and the temperature $T_{\rm DG}$ the energy density is given by:

$$\rho_{\rm DG}(T_{\rm DG}) = \frac{\pi^2}{30} g_{\rm DG} T_{\rm DG}^4, \tag{3.1}$$

where [22]:

$$g_{\rm DG} = \left(1 + \frac{7}{8}\right)\left[2(N_c^2 - 1) + 2N_cN_f\right] = 97.5 \tag{3.2}$$

This value keeps constant until the phase transition at a_c, since the elementary fields of the dark group are massless and they don't decay/condense into other particles before that time. Analogously, the energy density of the SM particles is given by:

$$\rho_{\rm SM}(T_{\rm SM}) = \frac{\pi^2}{30} g_{\rm SM} T_{\rm SM}^4, \tag{3.3}$$

where the degrees of freedom $g_{\rm SM}$ is a function of the temperature that decreases as the universe cools down and the particles become non-relativistic [28]. For the Minimum Supersymmetrical extension of the Standard Model, $g_{\rm SM}^{gut} = 228.75$ at the unification epoch a_{gut} [22], so $T_{\rm SM}(a_{gut}) = T_{\rm DG}(a_{gut})$ and the ratio of the energy densities are:

$$\frac{\rho_{\rm DG}(a_{gut})}{\rho_{\rm SM}(a_{gut})} = \frac{g_{\rm DG}}{g_{\rm SM}^{gut}} = 0.426, \tag{3.4}$$

which means that the dark group amounts to 30% the energy content of the universe at that time:

$$\Omega_{\rm DG}(a_{gut}) = \frac{\rho_{\rm DG}(a_{gut})}{\rho_{\rm SM}(a_{gut}) + \rho_{\rm DG}(a_{gut})} = 0.299 \tag{3.5}$$

As we stated before, below the unification scale the dark group and the SM particles interact only via gravity and they are no longer kept in thermal equilibrium. However, we can use entropy conservation to relate their temperatures below this point. Since now they are decoupled, the entropy per comoving volume $S = \frac{2\pi^2}{45} g T^3 a^3$ is independently conserved [22]. Let's first consider the period between the unification scale and the neutrino decoupling at $a_{\nu dec}$ ($T \sim 1\mathrm{MeV}$). For the dark group we have:

$$g_{\mathrm{DG}} T^3_{\mathrm{DG}}(a_{gut}) a^3_{gut} = g_{\mathrm{DG}} T^3_{\mathrm{DG}}(a_{\nu dec}) a^3_{\nu dec}, \tag{3.6}$$

while for the SM particles:

$$g^{gut}_{\mathrm{SM}} T^3_{\mathrm{SM}}(a_{gut}) a^3_{gut} = g^{\nu dec}_{\mathrm{SM}} T^3_{\mathrm{SM}}(a_{\nu dec}) a^3_{\nu dec} \tag{3.7}$$

Since $T_{\mathrm{SM}}(a_{gut}) = T_{\mathrm{DG}}(a_{gut})$ we divide these expressions to get:

$$\frac{T_{\mathrm{DG}}(a_{\nu dec})}{T_{\mathrm{SM}}(a_{\nu dec})} = \left(\frac{g^{\nu dec}_{\mathrm{SM}}}{g^{gut}_{\mathrm{SM}}} \right)^{1/3}, \tag{3.8}$$

where $g^{\nu dec}_{\mathrm{SM}} = 2 + \frac{7}{8}[2(3) + 2(2)] = 10.75$ accounting for the photons, three massless neutrino species (with their antiparticles), electrons, and positrons. Now let's consider the period between $a_{\nu dec}$ and the BDE field condensation epoch a_c. During this stage we have three decoupled fluids: the barotropic component consisting of photons, electrons and positrons, the dark group, and the neutrinos. Entropy conservation now states that:

$$\text{barotropic fluid:} \quad g_{\gamma e} T^3_{\mathrm{SM}}(a_{\nu dec}) a^3_{\nu dec} = g_\gamma T^3_\gamma(a_c) a^3_c \tag{3.9}$$

$$\text{neutrinos:} \quad g_\nu T^3_{\mathrm{SM}}(a_{\nu dec}) a^3_{\nu dec} = g_\nu T^3_\nu(a_c) a^3_c \tag{3.10}$$

$$\text{dark group:} \quad g_{\mathrm{DG}} T^3_{\mathrm{DG}}(a_{\nu dec}) a^3_{\nu dec} = g_{\mathrm{DG}} T^3_{\mathrm{DG}}(a_c) a^3_c, \tag{3.11}$$

where T_γ (T_ν) is the temperature of the photons (neutrinos), $g_{\gamma e} = 2 + \frac{7}{8}[2(2)] = \frac{11}{2}$ and $g_\gamma = 2$, this latter assuming that electrons and positrons annihilate before a_c so only photons contribute to the entropy [23]. Dividing equations (3.9) and (3.10) we recover the well-known relation between the photon and neutrino temperatures evaluated at a_c (1.35):

$$T_\gamma(a_c) = \left(\frac{g_{\gamma e}}{g_\gamma} \right)^{1/3} T_\nu(a_c) = \left(\frac{11}{4} \right)^{1/3} T_\nu(a_c) \tag{3.12}$$

This relation holds for arbitrary a below neutrino decoupling since both temperatures redshift as a^{-1}. If we now divide equations (3.10) and (3.11) we get:

$$T_\nu(a_c) = \frac{T_{\mathrm{SM}}(a_{\nu dec}) T_{\mathrm{DG}}(a_c)}{T_{\mathrm{DG}}(a_{\nu dec})} \tag{3.13}$$

Substituting this result and equation (3.8) into (3.12) we obtain:

$$T_\gamma(a_c) = \left(\frac{11}{4}\cdot\frac{g_{\rm SM}^{gut}}{g_{\rm SM}^{\nu dec}}\right)^{1/3} T_{\rm DG}(a_c) \tag{3.14}$$

On the other hand, the energy density of photons and neutrinos after $a_{\nu dec}$ is given by [28]:

$$\rho_r = \frac{\pi^2}{30} g_r T_\gamma^4, \tag{3.15}$$

where the degrees of freedom are:

$$g_r = 2 + \frac{7}{8}(2)N_\nu\left(\frac{T_\nu}{T_\gamma}\right)^4 = 2 + \frac{7}{4}N_\nu\left(\frac{4}{11}\right)^{4/3} = 3.383, \tag{3.16}$$

with $N_\nu = 3.046$ accounting for neutrino decoupling effects [82]. Combining equations (3.1), (3.15) and (3.14), the ratio of the energy density of the dark group to the standard radiation consisting of photons and neutrinos at the phase transition (ρ_{rc}) is:

$$\frac{\rho_{\rm DGc}}{\rho_{rc}} = \frac{g_{\rm DG}}{g_r}\left(\frac{4}{11}\cdot\frac{g_{\rm SM}^{\nu dec}}{g_{\rm SM}^{gut}}\right)^{4/3} = 0.1268, \tag{3.17}$$

which means that the dark group still amounts to a non-negligible fraction of the energy content of the universe when the BDE field condensation occurs:

$$\Omega_{\rm DGc} = \frac{\rho_{\rm DGc}}{\rho_{rc} + \rho_{\rm DGc}} = 0.113 \tag{3.18}$$

As we will see in section (3.3) the energy density of the dark group just at this time is given by:

$$\rho_{\rm DGc} = 3\Lambda_c^4, \tag{3.19}$$

where Λ_c is the condensation scale, while the density of photons and neutrinos is simply $\rho_{rc} = \rho_{r0} a_c^{-4}$. Substituting these results into equation (3.17) we arrive at:

$$\frac{a_c\Lambda_c}{\rm eV} = \left(\frac{\rho_{r0}}{3{\rm eV}^4}\cdot\frac{g_{\rm DG}}{g_r}\right)^{1/4}\left(\frac{4}{11}\cdot\frac{g_{\rm SM}^{\nu dec}}{g_{\rm SM}^{gut}}\right)^{1/3} = 1.0939\times 10^{-4}, \tag{3.20}$$

which is a meaningful constriction of the model relating the epoch and the energy scale of the BDE phase transition. This quantity can be used to parameterize the amount of non-standard radiation due to the dark group before the condensation. We recall that the energy density $\rho = \rho_\nu + \rho_{ext}$ of relativistic fluids other than photons is usually parameterized by N_{eff} defined as [26]:

$$\rho = N_{eff}\frac{7}{8}\left(\frac{4}{11}\right)^{4/3}\rho_\gamma, \tag{3.21}$$

where $N_{eff} = N_\nu + N_{ext}$. Using equations (1.36), (3.15) and (3.16) we simplify to:

$$\rho_{ext} = N_{ext}\frac{7}{8}\left(\frac{4}{11}\right)^{4/3}\rho_\gamma \tag{3.22}$$

If we evaluate this equation at a_c taking $\rho_{ext} = \rho_{\mathrm{DGc}} = 3\Lambda_c^4$ and solve for N_{ext} we get:

$$N_{ext} = \frac{3(a_c\Lambda_c)^4}{\rho_{\gamma 0}} \cdot \frac{8}{7}\left(\frac{11}{4}\right)^{4/3} \tag{3.23}$$

Substituting $a_c\Lambda_c$ from equation (3.20) we obtain:

$$N_{ext} = \frac{4}{7}g_{\mathrm{DG}}\left(\frac{g_{\mathrm{SM}}^{\nu dec}}{g_{\mathrm{SM}}^{gut}}\right)^{4/3} = 0.945, \tag{3.24}$$

where we use $\rho_{r0} = \frac{g_r}{2}\rho_{\gamma 0}$ from (3.15) and (3.16). It is important to bear in mind that unlike the usual extensions of the ΛCDM model where N_{ext} keeps constant over the whole history of the universe, in the BDE model the extra amount of radiation is only present before the phase transition and it vanishes once the condensation occurs. More precisely:

$$N_{ext} = \begin{cases} 0.945 & \text{if } a < a_c \\ \\ 0 & \text{if } a \geqslant a_c \end{cases} \tag{3.25}$$

Equations (3.24) and (3.2) show the relation between this amount of early radiation and the fundamental parameters of the model, to wit, the colours and flavours of the dark group. A change in N_c, N_f, the mechanism the BDE field condenses [22], the supersymmetric extension of the SM or even a purely phenomenological model where we have a transition from early dark radiation to a scalar field without a dark group would imply a different N_{ext}. In those scenarios N_{ext} can be calculated from equation (3.23) where a_c and Λ_c may be independent quantities not related by an expression of the form of (3.20). In any case the energy density before a_c redshifts as radiation $\propto a^{-4}$. For our BDE model we use equation (3.19) so:

$$\rho_{\mathrm{DG}}(a) = \rho_{\mathrm{DGc}}(a/a_c)^{-4} = 3(a_c\Lambda_c)^4 a^{-4} \qquad \text{for } a < a_c \tag{3.26}$$

and the expansion rate during that period is given by:

$$H^2(a) = \frac{8\pi G}{3}\left[\rho_{m0}a^{-3} + \rho_{r0}a^{-4} + \rho_{\mathrm{DGc}}(a/a_c)^{-4}\right] \qquad \text{for } a < a_c \tag{3.27}$$

3.2 The BDE potential

As the universe expands and the temperature decreases, the gauge coupling of the dark group becomes strong and the dark quarks stop being free, forming composite states which also interact with the particles of the Standard Model only through gravity. The condensation scale Λ_c at which this occurs is given by [22, 83]:

$$\Lambda_c = \Lambda_{gut} \cdot exp\left(-\frac{8\pi^2}{b_0 \alpha_{gut}^2}\right), \tag{3.28}$$

where $b_0 = 3N_c - N_f = 3$ is the one-loop beta function, Λ_{gut} is the unification scale and α_{gut} is the gauge coupling at that time. Taking $\Lambda_{gut} = (1.05 \pm 0.07) \times 10^{16}$ GeV and $\alpha_{gut}^2 = 4\pi/(25.83 \pm 0.16)$ [84] we find:

$$\Lambda_c = 34^{+16}_{-11} \text{ eV} \tag{3.29}$$

As we mentioned before, the lightest composite state corresponds to a meson represented by a scalar field φ. We assume that any other heavier state will decay into this meson rapidly [22]. At first sight this might seem a very artificial assumption, especially if we consider the whole variety of particles produced in QCD. However, even in this case the only free stable particle is the proton, so our hypothesis is not unnatural after all. Therefore, all the energy of the dark group is transferred to the scalar field at the phase transition and:

$$\rho_{\text{DGc}} = \rho_{\text{BDEc}} \tag{3.30}$$

The potential V of the scalar field arising from the non-perturbative effects of the strong interaction of the particles of the dark group can be calculated from the Affleck-Dine-Seiberg superpotential [85] for a non-Abelian $SU(N_c)$ group with N_f massless fields, which in this case leads to an inverse power law potential [22]:

$$V(\varphi) = \frac{\Lambda_c^{4+n}}{\varphi^n}, \tag{3.31}$$

where the exponent is given by:

$$n = 2\left(1 + \frac{2}{N_c - N_f}\right) \tag{3.32}$$

This potential is stable against radiative corrections [22, 23]. Note that all the relevant quantities we have introduced so far (c.f. equations (3.2), (3.20), (3.24), (3.28), and (3.32)) depend only on the parameters of the dark group and other quantities that we may know (g_r, $g_{\text{SM}}^{\nu dec}$), or we can measure with enough accuracy (ρ_{r0}), or that are fixed in nature if unification and supersymmetry turn out to be real (Λ_{gut}, α_{gut}, g_{SM}^{gut}). Therefore, we are not introducing extra free parameters other than N_c and N_f and once we set their values, these quantities are automatically fixed and cannot be varied arbitrarily, excepting Λ_c whose uncertainties come from the inaccuracy of Λ_{gut} and α_{gut}. Thus, for $N_c = 3$ and $N_f = 6$ the potential of the scalar BDE meson is:

$$V(\varphi) = \frac{\Lambda_c^{4+2/3}}{\varphi^{2/3}} \tag{3.33}$$

3.3 BDE background evolution

Once the condensation occurs the evolution of the scalar field is described by the same theoretical machinery as canonical quintessence. The term with the cosmological constant ($\Lambda/(8\pi G)$) in the Einstein-Hilbert action (1.4) is replaced by the minimally coupled lagrangian:

$$\mathcal{L} = \frac{1}{2} g^{\mu\nu} \partial_\mu \varphi \partial_\nu \varphi + V(\varphi), \tag{3.34}$$

where $V(\varphi) = \Lambda_c^{4+2/3} \varphi^{-2/3}$ as stated in equation (3.33). The components of the energy-momentum tensor can be readily obtained following the Noether's prescription:

$$T_{\mu\nu} = \frac{\partial \mathcal{L}}{\partial(\partial_\mu \varphi)} \partial_\nu \varphi - \mathcal{L} \delta^\mu_\nu = g^{\alpha\mu} \partial_\alpha \varphi \partial_\nu \varphi - \mathcal{L} \delta^\mu_\nu \tag{3.35}$$

Let's firstly consider a homogeneous field $\varphi = \varphi(t)$ in a flat universe described by the FLRW metric (1.2). The density and the pressure of the BDE field are:

$$\rho_{\rm BDE} = -T^0_0 = \frac{1}{2}\dot{\varphi}^2 + V \qquad\qquad P_{\rm BDE} = \frac{T^i_i}{3} = \frac{1}{2}\dot{\varphi}^2 - V, \tag{3.36}$$

so the equation of state $w_{\rm BDE} = P_{\rm BDE}/\rho_{\rm BDE}$ is given by:

$$w_{\rm BDE} = \frac{\frac{1}{2}\dot{\varphi}^2 - V}{\frac{1}{2}\dot{\varphi}^2 + V} \tag{3.37}$$

Unlike the ΛCDM model where the DE equation of state $w_\Lambda = -1$ is constant in time, the magnitude and sign of $w_{\rm BDE}$ at every moment depends on the interplay between the kinetic ($\dot{\varphi}^2$) and the potential (V) terms. However, the concordance of the ΛCDM model with the observations enforces a slow-roll condition of the scalar field at present:

$$w_{\rm BDE}(a_0) \approx -1 \quad \Rightarrow \quad \dot{\varphi}^2(a_0) \ll V(\varphi_0) \tag{3.38}$$

We can derive the Klein-Gordon equation governing the evolution of the BDE field by substituting the expressions of the energy density and the pressure (3.36) into the continuity equation (1.12):

$$\ddot{\varphi} + 3H\dot{\varphi} + \frac{dV}{d\varphi} = 0 \tag{3.39}$$

The Friedmann equation now reads as:

$$H^2 = \frac{8\pi G}{3}(\rho_r + \rho_m + \rho_{\rm BDE}), \tag{3.40}$$

where we have replaced the energy density of the dark group by the energy density of the BDE field. In solving the system of equations (3.39) and (3.40) we must specify the initial conditions. On this regard, since Λ_c is the relevant energy scale of the binding process of the elementary fields of the dark group, the natural initial condition of the scalar field at the condensation is:

$$\varphi_c = \Lambda_c \tag{3.41}$$

If we substitute this value into equations (3.36) and (3.37) and solve for $\dot{\varphi}$ we find:

$$\dot{\varphi}_c = \sqrt{2\Lambda_c^4\left(\frac{1+w_{\rm BDEc}}{1-w_{\rm BDEc}}\right)}, \tag{3.42}$$

where $w_{\rm BDEc}$ is the equation of state of the scalar field at the phase transition. We may assume that $w_{\rm BDEc} = 1/3$, since the dark group evolves as radiation before a_c and the effective mass of the scalar meson $m_\varphi = \sqrt{d^2V/d\varphi^2} = 1.05\Lambda_c$ at the condensation epoch is comparable to the temperature of the dark group at that time $T_{\rm DG}(a_c) = 24.4$ eV (c.f. equation (3.14)). In any case, we find that the late-time parameters H_0, $\Omega_{\rm BDE0}$ and $w_{\rm BDE0}$ are not sensitively affected by the choice of $w_{\rm BDEc}$. From now on, we'll take $w_{\rm BDEc} = 1/3$. The crucial point is that we don't need to know the dark energy density today to set the initial conditions of the scalar field. This is a remarkable difference with respect to other models where the scalar field is elemental. In such models the value of φ and $\dot{\varphi}$ at some initial time has to be set properly to retrieve the current value of the dark energy density. On the other hand, in the BDE model the initial conditions can be set naturally from physical considerations. Moreover, taking as input the value of the physical density of matter $\Omega_m h^2$ and the condensation scale Λ_c we solve the system of equations (3.39) and (3.40) with the initial conditions (3.41) and (3.42) to find a, φ and $\dot{\varphi}$ at any time. The dark energy density at present is given by evaluating the solution thus obtained at $z = 0$:

$$\rho_{\rm BDE0} = \frac{1}{2}\dot{\varphi}_0^2 + V(\varphi_0), \tag{3.43}$$

which directly leads to the current value of the expansion rate H_0. We see then, that in the BDE model the present content of dark energy is a derived quantity instead of being a free parameter. This appealing feature not only distinguish the BDE model from other scalar field theories, but also from the ΛCDM one. On this regard, we recall that in ΛCDM the dark energy density is given by $\rho_\Lambda = \Lambda/8\pi G$, where the cosmological constant Λ is a free parameter to be determined by the observations. Therefore, we conclude that *the BDE model has one less free parameter than ΛCDM.* We'll come back to this point in section (5.1.2). When solving equations (3.39) and (3.40) it is convenient to introduce the variables [17]:

$$x \equiv \frac{\dot{\varphi}}{M_{\rm Pl}\sqrt{6}H} \quad , \quad y \equiv \frac{\sqrt{V}}{M_{\rm Pl}\sqrt{3}H} \tag{3.44}$$

$$\lambda \equiv -\frac{M_{\rm Pl}V'}{V} \quad , \quad \Gamma \equiv \frac{VV''}{(V')^2}, \tag{3.45}$$

where $M_{\rm Pl} = (8\pi G)^{-1/2}$ is the reduced Planck mass and the primes stand for derivatives with respect to φ. We note that x and y are simply the square root of the kinetic and the potential terms of $\rho_{\rm BDE}$ divided by the critical density, respectively. From the above definitions the density parameter and the equation of state of the scalar field can be expressed as:

$$\Omega_{\rm BDE} = x^2 + y^2 \tag{3.46}$$

$$w_{\rm BDE} = \frac{x^2 - y^2}{x^2 + y^2}, \tag{3.47}$$

whereas the slow-roll condition of equation (3.38) now reads as:

$$x_0^2 \ll y_0^2 \tag{3.48}$$

If we introduce the total energy density of matter and radiation and its effective equation of state:

$$\rho_s(a) = \rho_m(a) + \rho_r(a), \tag{3.49}$$

$$w_s(a) = \frac{1}{3}\frac{\rho_r(a)}{\rho_r(a) + \rho_m(a)}, \tag{3.50}$$

we find:

$$\frac{\Omega_m(a)}{\Omega_r(a)} = \frac{\rho_{m0}a}{\rho_{r0}} = \frac{1 - 3w_s(a)}{3w_s(a)} \tag{3.51}$$

Substituting this result into the flatness relation $\Omega_m(a) + \Omega_r(a) + \Omega_{\rm BDE}(a) = 1$, the density parameter of matter and radiation at any time is given by:

$$\Omega_m(a) = [1 - 3w_s(a)][1 - \Omega_{\rm BDE}(a)] \quad , \quad \Omega_r(a) = 3w_s(a)[1 - \Omega_{\rm BDE}(a)] \tag{3.52}$$

Now we may take the time derivative of the Friedmann equation (3.40) and use expressions (3.39), (3.44), (3.49) and (3.50) to obtain:

$$\frac{\dot{H}}{H^2} = -\frac{3}{2}\left[2x^2 + (1 - x^2 - y^2)(1 + w_s)\right] \tag{3.53}$$

All these results show that the background quantities can be expressed by simple relations involving the dynamical variables defined in (3.44) and (3.45). In the same way, the equations (3.39) and (3.40) can be transformed into a system of equations for these variables. Taking the number of e-foldings after the condensation $N = \log(a/a_c)$ as the independent variable instead of the cosmic time and using the chain rule $\frac{d}{dt} = \frac{dN}{dt}\frac{d}{dN}$, we find:

$$x_N = -3x + \frac{\sqrt{6}}{2}\lambda y^2 + \frac{3}{2}x[2x^2 + (1 - x^2 - y^2)(1 + w_s)], \tag{3.54}$$

$$y_N = -\frac{\sqrt{6}}{2}\lambda xy + \frac{3}{2}y[2x^2 + (1 - x^2 - y^2)(1 + w_s)], \tag{3.55}$$

$$\lambda_N = -\sqrt{6}(\Gamma - 1)x\lambda^2, \tag{3.56}$$

where $f_N \equiv df/dN$. In the case of the potential (3.33), $\Gamma = 5/2$ so the dynamical system (3.54)-(3.56) is closed[1] but not autonomous since w_s explicitly depends on N. However, when the matter-radiation fluid is dominated by one of its components, $w_s \simeq 0$ or $1/3$ so in these epochs the equations (3.54)-(3.56) can be consider as an autonomous system. The energy density of the BDE field at a_c is obtained by evaluating the initial conditions (3.41) and (3.42) in the expression of $\rho_{\rm BDE}$ of equations (3.36):

$$\rho_{{\rm BDE}c} = \frac{1}{2}\dot{\varphi}_c^2 + \frac{\Lambda_c^{4+2/3}}{\varphi_c} = 3\Lambda_c^4 \tag{3.57}$$

As we stated before, this is the density of the dark group at the condensation scale $\rho_{\rm DGc}$ assuming all the composite dark hadrons decay into the lightest meson φ. The corresponding density parameter is:

$$\Omega_{{\rm BDE}c} = \frac{\rho_{{\rm BDE}c}}{\rho_{rc} + \rho_{mc} + \rho_{{\rm BDE}c}} = \frac{3(\Lambda_c a_c)^4}{\rho_{r0} + \rho_{m0}a_c + 3(\Lambda_c a_c)^4} \tag{3.58}$$

The initial conditions for x and y follow from equations (3.46) and (3.47). Solving for each one we obtain:

$$x_c = \sqrt{\frac{\Omega_{{\rm BDE}c}}{2}(1 + w_{{\rm BDE}c})} = \sqrt{\frac{2}{3}\Omega_{{\rm BDE}c}} \tag{3.59}$$

$$y_c = \sqrt{\frac{\Omega_{{\rm BDE}c}}{2}(1 - w_{{\rm BDE}c})} = \sqrt{\frac{1}{3}\Omega_{{\rm BDE}c}}, \tag{3.60}$$

whereas the initial condition for λ follows directly form its definition and equation (3.41):

$$\lambda_c = \frac{2}{3}\left(\frac{M_{\rm Pl}}{\Lambda_c}\right) \tag{3.61}$$

Figure (3.1**a**) shows the solution for x and y for $\Lambda_c = 44.02$ eV, $\Omega_c h^2 = 0.1173$, and

---

[1] That is, the equations don't involve any other dependent variable than x, y, and λ.

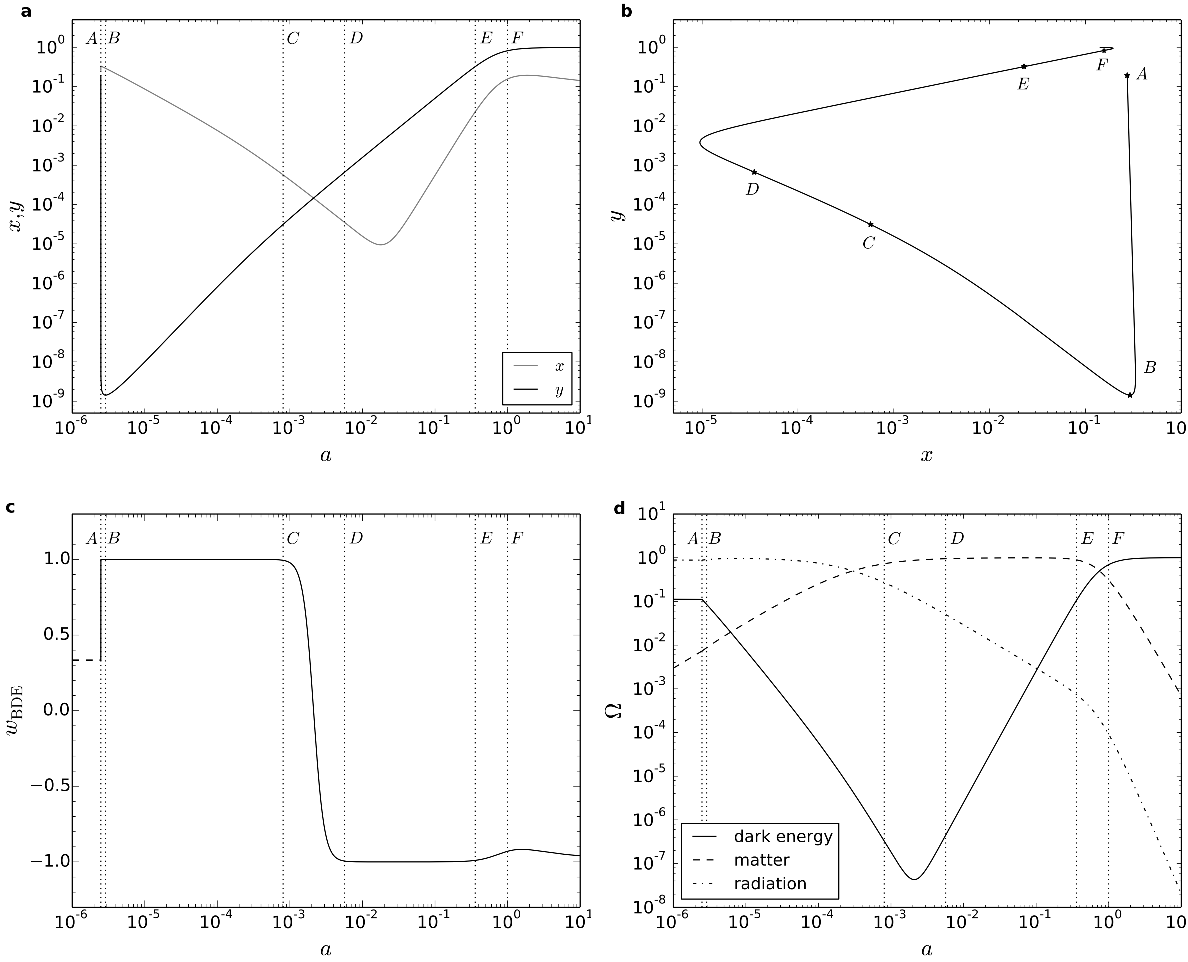

Figure 3.1: Background evolution in the BDE model. **a**, Solution for the dynamical variables x and y defined in equations (3.44). **b**, The path of the solution in the phase space. **c**, Evolution of the equation of state of the BDE scalar field. The dashed line corresponds to the equation of state $w_{\rm DG} = 1/3$ of the dark group. **d**, Density parameter of matter, radiation, and dark energy (first as the dark group, then as the BDE scalar field). Letters A and F mark the condensation and the present epochs, respectively, while the rest correspond to other important stages described in the text. In all these plots $\Lambda_c = 44.02$ eV, $\Omega_c h^2 = 0.1173$, and $\Omega_b h^2 = 0.02252$.

$\Omega_b h^2 = 0.02252$. From the constriction (3.20) we obtain $a_c = 2.48 \times 10^{-6}$. Substituting these values into equation (3.58) the density parameter of the BDE field at a_c is $\Omega_{{\rm BDE}c} = 0.1117$, so $x_c = 0.2729$, $y_c = 0.1930$, and $\lambda_c = 3.7 \times 10^{25}$. The condensation and the present epoch are indicated by A and F, respectively; the other letters mark specific stages in the dynamical evolution of the system. As we have seen, initially x and y

have similar values but then y undergoes a sudden drop of several orders of magnitude until reaches a minimum value at B almost instantly. From this time onwards it grows monotonically. On the other hand, x takes a little leap and then it falls too, but the fall is smooth and takes much more time before reaching the minimum, so immediately after the transition x dominates over y. This situation reverses between C and D where we can observe the cross-over. Then x reaches its minimum and starts growing but always keeping below y. The maximum close up occurs between E and the present epoch after which x reaches a maximum value and then decreases again, whereas y approaches asymptotically to 1. The path in the phase space can be seen in figure (3.1**b**), where the stars mark the corresponding epochs of figure (3.1**a**). The initial drop of y is depicted as fast move from A to B. Every time some variable reaches an extreme there is a turnaround in the curve. The stability conditions of the solution [70]:

$$\Gamma > 1 \quad , \quad \left| \frac{d\Gamma}{dN} \right| \ll 1 \tag{3.62}$$

are plenty satisfied by our potential (3.33), which means that although the present values of the solution may depend on the initial conditions, these are not fine-tuned [21]. The effect on the equation of state is shown in figure (3.1**c**). Before the phase transition the dark group evolves as radiation with $w_{\rm DG} = 1/3$. Once the condensation occurs the initial drop of y leads to a sudden leap to 1. Since x is much larger than y between B and C the equation of state stays at this value as we can see by taking $x \gg y$ in equation (3.47). The cross-over and the dominance of the potential term is reflected in the change from 1 to -1. Here we have $y \gg x$ so equation (3.47) this time leads to $w_{\rm BDE} \simeq -1$. Although the scale factor when this happens depends predominantly on Λ_c and $\Omega_c h^2$ we will see that for the models favoured by the observations C is located shortly after decoupling. This implies that for most of the cosmic time the equation of state behaves like a cosmological constant. Finally, when x gets closer to y between E and the present epoch, the equation of state grows to a larger value and eventually it will be approaching to -1 in the future. The evolution of the density parameter of the scalar field, matter, and radiation is shown in figure (3.1**d**). Before the phase transition the density parameter of the dark group is:

$$\Omega_{\rm DG}(a < a_c) = \frac{\Omega_{{\rm DG}c}}{\Omega_{rc} + \Omega_{mc}(a/a_c) + \Omega_{{\rm DG}c}}, \tag{3.63}$$

where $\Omega_{{\rm DG}c} = \Omega_{{\rm BDE}c} = 0.1117$ as we have seen, and Ω_{mc} and Ω_{rc} is the value of the density parameter of matter and standard radiation (photons and neutrinos) at a_c, respectively. These can be obtained by substituting $\Omega_{{\rm BDE}c}$ and a_c into equations (3.50) and (3.52). Since in these times the matter density is negligible $\Omega_{\rm DG}(a < a_c) \approx \Omega_{{\rm DG}c}/(\Omega_{rc}+\Omega_{{\rm DG}c})$. When the condensation occurs the equation of state leaps to 1. This implies that the energy density of the BDE field dilutes faster than matter and radiation as $\rho_{\rm BDE} \sim a^{-6}$, reaching its minimum in the cross-over of x and y. From this time onwards, $\Omega_{\rm BDE}$ grows monotonically equating the matter density in the recent past and since then driving the expansion as required by the observations. Some of the dynamics shown in figure (3.1) turns out to be irrelevant for the cosmological observations since the BDE field component remains subdominant over almost all the history of the universe until late times. However, the dark group amounts to a non-negligible fraction of the energy density in the early universe. Therefore, besides the late-time effects of the dark energy we expect additional imprints left by the early contribution of the dark group. This is one of the main differences of the BDE model with respect to ordinary quintessence.

3.4 BDE perturbations

The smooth background approximation must be refined to account for the inhomogeneities of matter and radiation we observe. These inhomogeneities are also present both in the dark group and the BDE field since they are coupled with the other fluids through the metric, so a physical realistic description must include perturbations in the dark group and the scalar field too [69]. We assume that before a_c the dark group perturbations behave as the neutrino perturbations. This assumption relies on the fact that at the initial time when we start solving the equations, the neutrinos are already decoupled from the electrons, so they interact with the other particles only via gravity making no difference with respect the dynamics of the particles of the dark group. We'll come back to this point in section (4.3). Once the transition occurs, we decompose the BDE field into a homogeneous part (denoted with a bar as in section (1.2) and a small position-dependent perturbation:

$$\varphi(\tau, \mathbf{x}) = \bar{\varphi}(\tau) + \delta\varphi(\tau, \mathbf{x}), \tag{3.64}$$

where τ is the conformal time. The lagrangian of equation (3.34) is now given by:

$$\mathcal{L} = \frac{1}{2} g^{\mu\nu} (\partial_\mu \bar{\varphi} + \partial_\mu \delta\varphi)(\partial_\nu \bar{\varphi} + \partial_\nu \delta\varphi) + V(\bar{\varphi} + \delta\varphi) \tag{3.65}$$

If we perform a Taylor expansion about $\bar{\varphi}$ we get:

$$V(\bar{\varphi} + \delta\varphi) = V(\bar{\varphi}) + \left.\frac{dV}{d\varphi}\right|_{\varphi=\bar{\varphi}} \delta\varphi \tag{3.66}$$

From now on, we denote $V = V(\bar{\varphi})$, $\left.\frac{dV}{d\varphi}\right|_{\varphi=\bar{\varphi}} = V_\varphi$, and $\left.\frac{d^2V}{d\varphi^2}\right|_{\varphi=\bar{\varphi}} = V_{\varphi\varphi}$. Working in the synchronous gauge (1.53) the perturbations of the energy density and the pressure are:

$$\delta\rho_{\rm BDE} = -\delta T^0_0 = \frac{\bar{\varphi}' \delta\varphi'}{a^2} + V_\varphi \delta\phi, \quad \delta P_{\rm BDE} = \frac{1}{3} {\rm Tr}(\delta T^i_j) = \frac{1}{3} {\rm Tr} \left[\left(\frac{\bar{\varphi}' \delta\varphi'}{a^2} - V_\varphi \delta\varphi \right) \delta^i_j \right] \tag{3.67}$$

We see that $\delta T^i_j = 0$ for $i \neq j$, which means that the BDE field has no anisotropic shear $\sigma = 0$ (c.f. equation (1.46)). The other components of the perturbed energy-momentum tensor are:

$$\delta T^i_0 = -\delta T^0_i = \frac{\bar{\varphi}'}{a^2}\partial_i \delta\varphi \tag{3.68}$$

Taking the Fourier transform, the velocity divergence eq. (1.45) is given by:

$$(\bar{\rho}_{\text{BDE}} + \bar{P}_{\text{BDE}})\theta_{\text{BDE}} = ik_j \delta T^0_j = \frac{k^2}{a^2}\bar{\varphi}'\delta\varphi \;\;\Rightarrow\;\; \theta_{\text{BDE}} = \frac{k^2\delta\varphi}{\bar{\varphi}'}, \tag{3.69}$$

where we have used equations (3.36) and transformed to conformal time derivatives according to equation (1.38). In this regard, the Klein-Gordon equation (3.39) in conformal time reads as:

$$\bar{\varphi}'' + 2\mathcal{H}\bar{\varphi}' + a^2 V_\varphi = 0, \tag{3.70}$$

while the continuity equation (1.12) has the same form by placing $\mathcal{H}$ instead of H: $\bar{\rho}' + 3\mathcal{H}(\bar{\rho} + \bar{P}) = 0$. Using equations (3.67), (3.69), (3.70), (3.37) and (1.12) the evolution of the BDE scalar field overdensities $\delta_{\text{BDE}} \equiv \delta\rho_{\text{BDE}}/\bar{\rho}_{\text{BDE}}$ are given by:

$$\delta'_{\text{BDE}} = \frac{1}{a^2\bar{\rho}_{\text{BDE}}}\left[\bar{\varphi}'\delta\varphi'' - \mathcal{H}(1 - 3w_{\text{BDE}})\bar{\varphi}'\delta\varphi' + a^2(\bar{\varphi}'V_{\varphi\varphi} + 3\mathcal{H}(1 + w_{\text{BDE}})V_\varphi)\delta\varphi\right] \tag{3.71}$$

Substituting this result into the conservation equation (1.59) and after doing some algebraic manipulation we arrive at a Klein-Gordon equation for $\delta\varphi$:

$$\delta\varphi'' + 2\mathcal{H}\delta\varphi' + (k^2 + a^2 V_{\varphi\varphi})\delta\varphi = -\frac{1}{2}\bar{\varphi}'h' \tag{3.72}$$

As we can see (c.f. section (4.3)), the scalar field inhomogeneities are coupled with the perturbation equations of the other fluids through the synchronous potential h (or equivalently, the cold dark matter perturbations δ_c). In order to solve equation (3.72), we need to set the initial conditions for $\delta\varphi$ and $\delta\varphi'$ at the condensation epoch a_c. However, it has been shown [72] that for inverse power law potentials the perturbed solutions are insensitive to the initial conditions, so we are free to select them arbitrarily. In our case, we match the overdensities of the dark group and the BDE field at a_c, i.e., $\delta_{\text{DG}}(a_c) = \delta_{\text{BDE}}(a_c)$, where

$$\delta_{\text{BDE}} = \left(\frac{\bar{\varphi}'\delta\varphi'}{a^2} + V_\varphi \delta\phi\right)/\bar{\rho}_{\text{BDE}} \tag{3.73}$$

Substituting equations (3.41) and (3.57) into this expression we can solve either for $\delta\varphi(a_c)$, $\delta\varphi'(a_c)$ or both of them. We consider three cases:

$$i) \qquad \delta\varphi'(a_c) = 0 \;\;\text{and}\;\; \delta\varphi(a_c) = -\frac{9}{2}\Lambda_c \delta_{\text{DG}}(a_c) \tag{3.74}$$

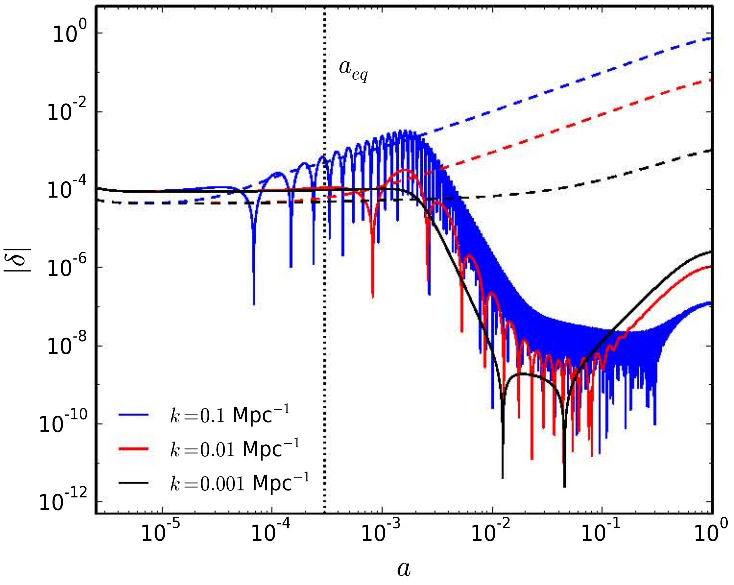

Figure 3.2: Evolution of dark energy overdensities (solid) and matter (dashed) in the newtonian gauge for modes entering the horizon before ($k = 0.1\mathrm{Mpc}^{-1}$), at ($k = 0.01\mathrm{Mpc}^{-1}$) and after ($k = 0.001\mathrm{Mpc}^{-1}$) the matter-radiation epoch a_{eq} (vertical dotted). In order to show the fluctuations below the background $\bar{\rho}_{\mathrm{BDE}}$ we plot the absolute value $|\delta_{\mathrm{BDE}}|$; in the case of the matter overdensities, $|\delta_m| = \delta_m$.

$$ii) \qquad \delta\varphi(a_c) = 0 \quad \text{and} \quad \delta\varphi'(a_c) = \frac{3}{2} a_c \Lambda_c^2 \delta_{\mathrm{DG}}(a_c) \tag{3.75}$$

$$iii) \quad \frac{\bar{\varphi}'\delta\varphi'}{a^2} = 2V_\varphi \delta\varphi \neq 0 \ \text{ with } \ \delta\varphi(a_c) = -\frac{3}{2}\Lambda_c \delta_{\mathrm{DG}}(a_c)\ ,\ \delta\varphi'(a_c) = a_c \Lambda_c^2 \delta_{\mathrm{DG}}(a_c) \tag{3.76}$$

We verified that the solutions obtained in each case are the same as expected. Once we solve for $\delta\varphi$ and get δ_{BDE} from equation (3.73) using the background solution, we can substitute this result into equation (1.61) to convert it to the newtonian gauge. Figure (3.2) shows the evolution of BDE overdensities for modes entering the horizon before, at, and after the matter-radiation equality epoch a_{eq}. For the sake of comparison we also plot the matter overdensities. The modes entering the horizon before a_{eq} are characterised by rapid oscillations whose amplitudes are initially enhanced and subsequently damped from $a \sim 2 \times 10^{-3}$ to the present epoch. For these modes the time average is zero $< \delta_{\mathrm{BDE}} > \simeq 0$ so at small scales the dark energy is very homogeneous. On the other hand, for large modes these oscillations are less present and particularly at late times there is a growth of dark energy structure, but even in those cases the growth is negligible in comparison with the matter, so at large scales the dark energy is also very homogeneous.

Chapter 4

Cosmological implications

The distinctive dynamics of the dark energy in the BDE model has effects on the physical quantities that can be measured through the cosmological probes we review in the previous chapter. These effects manifest both at the background and perturbation level, and unlike traditional quintessence models, the influence of the dark energy component (first as the dark group and then as the scalar field) is present not only at late times, but also in the early universe. In this chapter we study the cosmological implications of the BDE model and its main differences with respect to ΛCDM. To that end, we adopt a fiducial ΛCDM cosmology running with the following set of basic parameters: $\Omega_b h^2 = 0.02252$, $\Omega_c h^2 = 0.1173$, $H_0 = 67.68\ \mathrm{km}\cdot\mathrm{s}^{-1}\mathrm{Mpc}^{-1}$, $n_s = 0.9774$, $A_s = 2.367 \times 10^{-9}$ and optical depth $\tau = 0.117$. We have shown that in the BDE model the present content of dark energy or H_0 can be calculated from $\rho_{m0} \propto \Omega_m h^2$ and Λ_c. The value of the condensation scale consistent with these fiducial values of $\Omega_b h^2$, $\Omega_c h^2$ and H_0 is $\Lambda_c = 44.02\mathrm{eV}$. Thus, throughout this chapter both the matter and the dark energy content of the universe at present time and the primordial power spectrum will be the same in both models, so all the differences arise because of the effect of the dark group and the scalar field. This allows us to identify where the BDE model deviates from the ΛCDM scenario the most and it will be a very useful tool to analyse the results when we fit the data in the next chapter. In section (4.1) we study the differences on the expansion rate and the cosmological distances probed by SNeIa and BAO information. We study the impact of the dark group in the production of light nuclei during Big Bang Nucleosynthesis (BBN) in section (4.2). The perturbation equations (synchronous gauge) of the BDE model when the dark group and the scalar field is present are shown in section (4.3). Then we study the evolution of matter perturbations and the imprint left on the matter power spectrum. Finally in section (4.4) we discuss the effects on the temperature anisotropy spectrum of the CMB.

4.1 The expansion rate and cosmological distances

The immediate consequence of considering other mechanism than the cosmological constant as the physical origin of the dark energy is the modification of the expansion rate. We recall that in the BDE and ΛCDM models this quantity is given by:

$$H^2_{\rm BDE}(a) = \begin{cases} \frac{8\pi G}{3}[\rho_{m0}a^{-3} + \rho_{r0}a^{-4} + \rho_{\rm DGc}(a/a_c)^{-4}] & \text{if } a < a_c \\ \\ \frac{8\pi G}{3}[\rho_{m0}a^{-3} + \rho_{r0}a^{-4} + \rho_{\rm BDE}] & \text{if } a \geqslant a_c \end{cases} \tag{4.1}$$

$$H^2_{\Lambda{\rm CDM}}(a) = \tfrac{8\pi G}{3}[\rho_{m0}a^{-3} + \rho_{r0}a^{-4} + \rho_\Lambda] \tag{4.2}$$

As we have shown in the previous chapter, the large value of $a_c\Lambda_c/\mathrm{eV}$ (resulting from the degrees of freedom of the dark group prior the condensation, c.f. eq(3.20)) leads to a non-negligible contribution of the dark group to the energy content of the universe at early times. This contribution can be expressed in terms of additional radiation before the phase transition as stated in equation (3.25). We therefore expect to see major deviations from the ΛCDM model not only at late times when the dark energy obeys a quite distinct dynamics, but also when the extra relativistic degrees of freedom due to the dark group are present.

Figure (4.1) shows the ratio $H_{\rm BDE}/H_{\Lambda{\rm CDM}}$ as a function of the scale factor. Before the phase transition the ratio is nearly constant $H_{\rm BDE}/H_{\Lambda{\rm CDM}} \approx \sqrt{1+\rho_{\rm DGc}/\rho_{rc}} = 1.062$ since the matter content is negligible during the radiation epoch $a \lesssim 3\times10^{-4}$. When the condensation occurs the BDE scalar field component quickly dilutes because the equation of state immediately leaps to 1 as shown in figure (3.1**c**) making the field redshift as $\rho_{\rm BDE} \propto a^{-6}$ in this period. The dilution of the scalar field proceeds so quickly that long before the matter-radiation equality takes place the expansion rate in both models are the same. This situation prevails over the matter epoch until the dark energy becomes relevant at late times. Note that for our specific choice of cosmological parameters $\rho_{\rm BDE}(a_0) = \rho_\Lambda$, so $H_{\rm BDE}/H_{\Lambda{\rm CDM}} = 1$ also today. However, since the equation of state of the scalar field departs from -1 to a larger value at low redshifts (c.f. fig(3.1**c**)), $\rho_{\rm BDE} \propto a^{-3(1+w_{\rm BDE})} > \rho_\Lambda$ which implies that $H_{\rm BDE}/H_{\Lambda{\rm CDM}} > 1$ leading to the peak observed in the plot.

We can verify that the peak is due to the difference of the dark energy dynamics at late times by plotting the ratio for a ΛCDM model with extra relativistic degrees of freedom $N_{ex} = 0.945$ over the whole history of the universe. At early times the ratio is the same as BDE, but now there isn't a rapid dilution of the scalar field at a_c. Instead, the total amount of radiation dilutes slowly shifting the equality epoch to a later time. Once the content of radiation is negligible, $H_{\Lambda{\rm CDM}}(N_{ex})/H_{\Lambda{\rm CDM}} \approx 1$, and since the dynamics of the dark energy is the same in both models the ratio is not modified at late times when the dark energy drives the expansion, so the peak is absent in this case. The cosmological implications of the different expansion rate both at early and

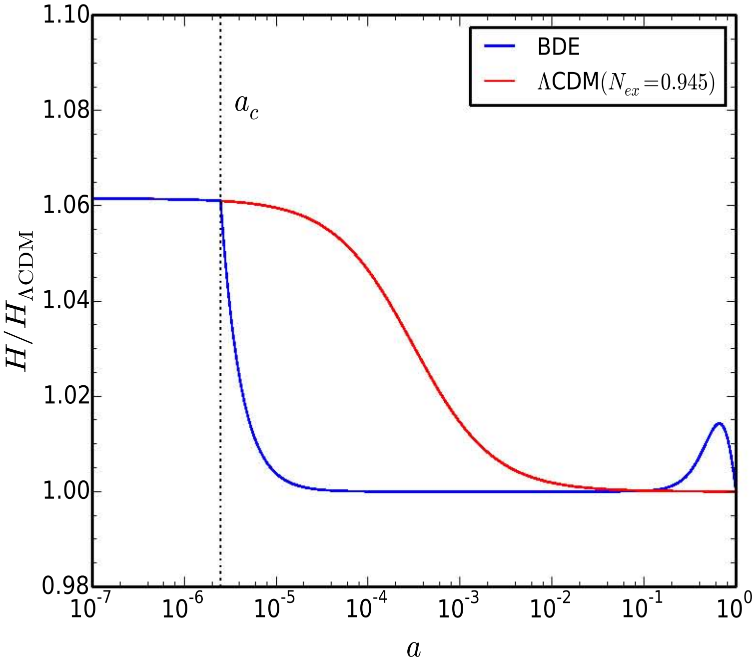

Figure 4.1: Comparison of the expansion rate between the BDE and the ΛCDM models. The blue curve shows the ratio $H_{\mathrm{BDE}}/H_{\Lambda\mathrm{CDM}}$ before and after the phase transition as given by equations (4.1) and (4.2). The vertical dotted line marks the condensation epoch. The red curve shows the ratio of the expansion rate for a ΛCDM cosmology with $N_{ex} = 0.945$ extra relativistic degrees of freedom to standard ΛCDM with only three massless neutrino species.

late times in the BDE model is reflected in all the observables we discussed in chapter 2. Let's first consider distance measurements at low redshifts. If we express the luminosity distance of equation (2.1) in terms of the redshift we have:

$$d_L(z) = (1+z)\int_0^z \frac{1}{H(z')}dz' \tag{4.3}$$

This is a general expression also valid for the BDE model. Since $H_{\Lambda\mathrm{CDM}} < H_{\mathrm{BDE}}$ at $z \lesssim 4$, the luminosity distance in the BDE model is smaller than in ΛCDM. Now, from the definition of the distance modulus in equation (2.10), this implies that $\mu_{\mathrm{BDE}} < \mu_{\Lambda\mathrm{CDM}}$ as shown in figure (4.2**a**), where we plot the ratio $\mu_{\mathrm{BDE}}/\mu_{\Lambda\mathrm{CDM}}$ in the range of redshifts accessible by present day SNeIa and BAO measurements. Therefore, for this combination of parameters light sources appear slightly fainter in a ΛCDM cosmology. On the other hand, angular diameter distances are smaller in the BDE model as can be immediately deduced from equation (2.14). We have then $(D_A^2/H)_{\mathrm{BDE}} < (D_A^2/H)_{\Lambda\mathrm{CDM}}$

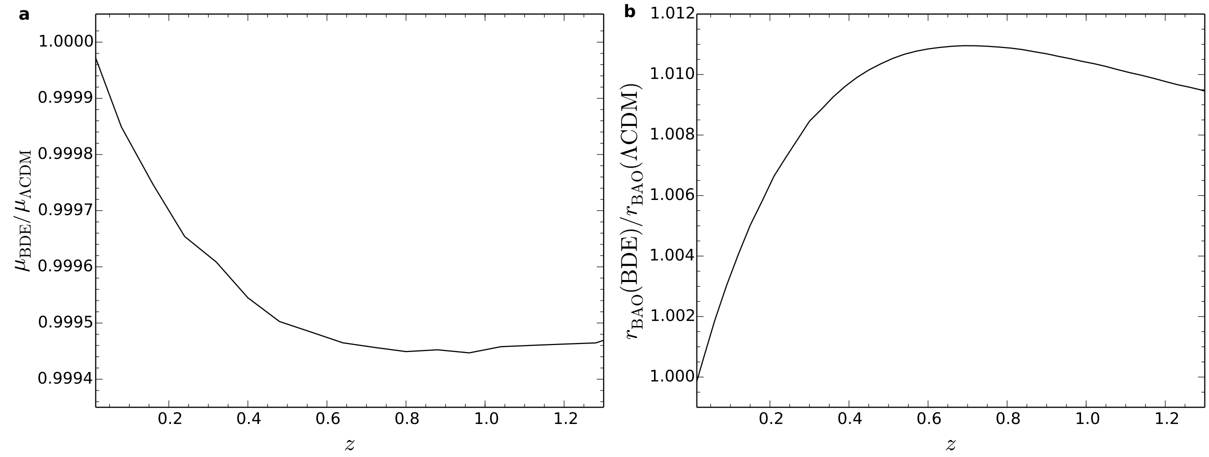

Figure 4.2: Effect of the expansion rate on SNeIa and BAO distance measurements. **a**, Comparison of the distance modulus μ for the BDE and ΛCDM models. **b**, Comparison of the BAO ratio.

and therefore $D_V(\text{BDE}) < D_V(\Lambda\text{CDM})$. If we recall that the sound horizon at the drag epoch depends predominantly on $\Omega_b h^2$ and $\Omega_c h^2$, we get $r_s(\text{BDE}) \approx r_s(\Lambda\text{CDM})$ and thus $r_{\text{BAO}}(\Lambda\text{CDM}) < r_{\text{BAO}}(\text{BDE})$ as shown in figure (4.2**b**). We stress that these conclusions are valid only when both models run with the same parameters. As we will see in section (5) when fitting to measurements the values of the parameters may change from model to model and therefore both the amount of deviation and even the relative order of μ and r_{BAO} won't be necessarily the same. In any case, note that r_{BAO} is more sensitive than μ to the underlying cosmology. This is because μ is a logarithmic function of d_L instead of an algebraic one as r_{BAO}, making more difficult to observe deviations in the SNeIa diagrams.

4.2 Light element abundances

The freeze-out temperature at which neutrinos decouple from the electrons and positrons before the onset of BBN is given by $T_f \simeq (H/G_F)^{1/5}$ [87]. Consequently, a higher expansion rate H leads to a higher temperature T_f. Since the neutron-to-proton ratio at freeze-out depends on T_f as $(n/p)_f \simeq e^{-(m_n-m_p)/T_f}$ and the helium-4 abundance roughly depends on $(n/p)_{\text{BBN}}$ —which is slightly smaller than $(n/p)_f$ because of the decays of free neutrons between the freeze-out and the beginning of BBN— as $Y_{\text{P}}^{\text{BBN}} = 2(n/p)_{\text{BBN}}/[1+(n/p)_{\text{BBN}}]$, a larger value of T_f automatically yields an increased fraction of helium [87]. The same conclusion is also valid for deuterium production. Therefore, the enhanced expansion rate in the BDE model due to the presence of the massless

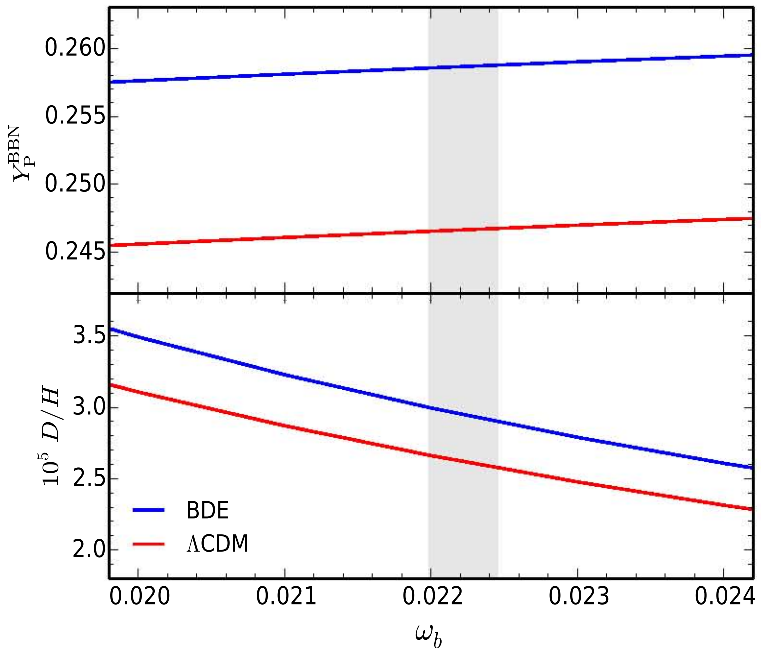

Figure 4.3: Standard BBN predictions for the abundances of primordial helium-4 (top) and deuterium (bottom) according to the fitting formulae (4.4) and (4.5) provided by the PArthENoPE code team [26, 86]. The grey band marks the 68% confidence limits on the physical density of baryons (ω_b) found by the Planck collaboration using only the temperature anisotropy spectrum of the CMB [26].

particles of the dark group before the condensation leads to an increased fraction of light elements produced during BBN. This is not a unique feature of BDE, but is a general result of any model introducing extra relativistic degrees of freedom N_{ext} in the early universe. In the standard BBN scenario, the abundances of light nuclei depend also on the cross sections of the nuclear reactions involved in each case, the neutron mean lifetime, and the baryon-to-photon ratio $\eta \equiv n_b/n_\gamma$ which is related to the physical density of baryons $\omega_b \equiv \Omega_b h^2$ up to a negligible correction involving $Y_{\rm P}^{\rm BBN}$ [87]. Assuming updated measurements of the nuclear cross sections and a neutron lifetime $\tau_n = 880.3 \pm 1.1\ s$ [88], the abundance of helium-4 ($Y_{\rm P}^{\rm BBN} \equiv 4n_{\rm He}/n_b$) and deuterium ($10^5 D/H \equiv 10^5 n_D/n_H$) can be parameterised by N_{ext} and ω_b according to the following formulae [26, 86]:

$$\begin{aligned} Y_{\rm P}^{\rm BBN} &= 0.2311 + 0.9502\omega_b - 11.27\omega_b^2 \\ &\quad + N_{ext}(0.01356 + 0.008581\omega_b - 0.1810\omega_b^2) \\ &\quad + N_{ext}^2(-0.0009795 - 0.001370\omega_b + 0.01746\omega_b^2) \end{aligned} \tag{4.4}$$

$$\begin{aligned}10^5 D/H &= 18.754 - 1534.4\omega_b + 48656\omega_b^2 - 552670\omega_b^3 \\ &\quad + N_{ext}(2.4914 - 208.11\omega_b + 6760.9\omega_b^2 - 78007\omega_b^3) \\ &\quad + N_{ext}^2(0.012907 - 1.3653\omega_b + 37.388\omega_b^2 - 267.78\omega_b^3) \qquad (4.5)\end{aligned}$$

Figure (4.3) shows these predicted abundances for the BDE —with $N_{ext} = 0.945$ for $a < a_c$— and ΛCDM —with $N_{ext} = 0$— models as a function of ω_b. Note the mild dependence of $Y_{\mathrm{P}}^{\mathrm{BBN}}$ on ω_b in contrast with the high sensitivity of $10^5 D/H$ on this parameter. The grey band marks the 1σ bounds on ω_b found by the Planck collaboration using only measurements of the CMB temperature anisotropy spectrum. The extra amount of early radiation in the BDE model leads to a marked excess of about 4.8% and 12.7% of helium and deuterium, respectively. Although these numbers are by no means a small difference, we will see in section (5.4) that the current astrophysical observations are too sparse to provide uncontroversial evidence of such excess.

4.3 Evolution of matter perturbations

The particular dynamics of the dark energy in the BDE model is interestingly reflected in the evolution of matter fluctuations since in this case the effects of the new dynamics manifest simultaneously not only at early and at late times as we may expect from our previous results, but also when the transition from the dark group to the scalar field occurs. Just like we did before, we solve the perturbation equations in the synchronous gauge and convert the solutions to the newtonian gauge to analyse the results. We need to adapt equations (1.64)-(1.71) to our model, according to whether the dark group or the BDE scalar field is present. As we mentioned before, prior the phase transition when we start solving the equations, the dark group particles behave as neutrinos, so the effective number of relativistic degrees of freedom besides photons is $N_{eff} = N_\nu + N_{ext} = 3.991$ instead of $N_{eff} = 3.046$ for three massless neutrino species. The contribution of the dark group to the total density perturbation $-\delta T^0_0$ is $\bar{\rho}_{\mathrm{DG}}\delta_{\mathrm{DG}}$. Taking $\delta_{\mathrm{DG}} = \delta_\nu$ and $\theta_{\mathrm{DG}} = \theta_\nu$, the modified version of equations (1.64), (1.65), (1.66), (1.68), and (1.70) in the synchronous gauge before the phase transition takes place is:

$$k^2\eta' = 4\pi G a^2 \left[\bar{\rho}_b\theta_b + \tfrac{4}{3}\bar{\rho}_\gamma\theta_\gamma + \tfrac{4}{3}(\bar{\rho}_\nu + \bar{\rho}_{\mathrm{DG}})\theta_\nu\right] \qquad (4.6)$$

$$\delta_c' = -\frac{a}{a'}[4\pi G a^2(\bar{\rho}_b\delta_b + \bar{\rho}_c\delta_c + \bar{\rho}_\gamma\delta_\gamma + (\bar{\rho}_\nu + \bar{\rho}_{\mathrm{DG}})\delta_\nu) + k^2\eta] \qquad (4.7)$$

$$\delta_b' = -\theta_b - \frac{a}{a'}[4\pi G a^2(\bar{\rho}_b\delta_b + \bar{\rho}_c\delta_c + \bar{\rho}_\gamma\delta_\gamma + (\bar{\rho}_\nu + \bar{\rho}_{\mathrm{DG}})\delta_\nu) + k^2\eta] \qquad (4.8)$$

$$\delta_\gamma' = -\frac{4}{3}\theta_\gamma - \frac{4a}{3a'}[4\pi G a^2(\bar{\rho}_b\delta_b + \bar{\rho}_c\delta_c + \bar{\rho}_\gamma\delta_\gamma + (\bar{\rho}_\nu + \bar{\rho}_{\mathrm{DG}})\delta_\nu) + k^2\eta] \qquad (4.9)$$

$$\delta_\nu' = -\frac{4}{3}\theta_\nu - \frac{4a}{3a'}[4\pi G a^2(\bar{\rho}_b\delta_b + \bar{\rho}_c\delta_c + \bar{\rho}_\gamma\delta_\gamma + (\bar{\rho}_\nu + \bar{\rho}_{\mathrm{DG}})\delta_\nu) + k^2\eta], \qquad (4.10)$$

The equations of the velocity divergence (1.67), (1.69), and (1.71) remain unchanged, since they don't depend directly on $(\bar{\rho}+\bar{P})\theta$ or δT^0_0. When the condensation occurs, $(\bar{\rho}_{\rm DG}+\bar{P}_{\rm DG})\theta_{\rm DG}=\frac{4}{3}\bar{\rho}_{\rm DG}\theta_{\rm DG}$ is replaced by:

$$(\bar{\rho}_{\rm BDE}+\bar{P}_{\rm BDE})\theta_{\rm BDE}=\frac{k^2}{a^2}\bar{\varphi}'\delta\varphi \qquad (4.11)$$

and $\bar{\rho}_{\rm DG}\delta_\nu$ by:

$$\bar{\rho}_{\rm BDE}\delta_{\rm BDE}=\frac{\bar{\varphi}'\delta\varphi'}{a^2}+V_\varphi\delta\varphi, \qquad (4.12)$$

where we have used equations (3.67) and (3.68).Therefore, the perturbation equations in this case are:

$$k^2\eta'=4\pi Ga^2\left[\bar{\rho}_b\theta_b+\tfrac{4}{3}\bar{\rho}_\gamma\theta_\gamma+\tfrac{4}{3}\bar{\rho}_\nu\theta_\nu+\tfrac{k^2}{a^2}\bar{\varphi}'\delta\varphi\right] \qquad (4.13)$$

$$\delta_c'=-\frac{a}{a'}[4\pi Ga^2(\bar{\rho}_b\delta_b+\bar{\rho}_c\delta_c+\bar{\rho}_\gamma\delta_\gamma+\bar{\rho}_\nu\delta_\nu+\bar{\rho}_{\rm BDE}\delta_{\rm BDE})+k^2\eta] \qquad (4.14)$$

$$\delta_b'=-\theta_b-\frac{a}{a'}[4\pi Ga^2(\bar{\rho}_b\delta_b+\bar{\rho}_c\delta_c+\bar{\rho}_\gamma\delta_\gamma+\bar{\rho}_\nu\delta_\nu+\bar{\rho}_{\rm BDE}\delta_{\rm BDE})+k^2\eta] \qquad (4.15)$$

$$\delta_\gamma'=-\frac{4}{3}\theta_\gamma-\frac{4a}{3a'}[4\pi Ga^2(\bar{\rho}_b\delta_b+\bar{\rho}_c\delta_c+\bar{\rho}_\gamma\delta_\gamma+\bar{\rho}_\nu\delta_\nu+\bar{\rho}_{\rm BDE}\delta_{\rm BDE})+k^2\eta] \qquad (4.16)$$

$$\delta_\nu'=-\frac{4}{3}\theta_\nu-\frac{4a}{3a'}[4\pi Ga^2(\bar{\rho}_b\delta_b+\bar{\rho}_c\delta_c+\bar{\rho}_\gamma\delta_\gamma+\bar{\rho}_\nu\delta_\nu+\bar{\rho}_{\rm BDE}\delta_{\rm BDE})+k^2\eta], \qquad (4.17)$$

where $\delta\varphi$ is given by the perturbed Klein-Gordon equation (3.72). The influence of BDE perturbations on the evolution of dark matter overdensities is clearly seen by substituting equation (1.55) into (1.57):

$$h''+\mathcal{H}h'=-8\pi Ga^2(\delta T^i_i-\delta T^0_0) \qquad (4.18)$$

Since $\delta_c'=-h'/2$ in the synchronous gauge, we obtain:

$$\delta_c''+\mathcal{H}\delta_c'=4\pi Ga^2(\delta T^i_i-\delta T^0_0), \qquad (4.19)$$

where $\delta T^i_i-\delta T^0_0=3\delta P+\delta\rho=\delta\rho(3c_s^2+1)$ and $4\pi Ga^2\delta\rho=\frac{3}{2}\mathcal{H}^2\Omega\delta$. If we consider all the fluids we arrive at:

$$\delta_c''+\mathcal{H}\delta_c'-\frac{3}{2}\mathcal{H}^2\sum_i\Omega_i\delta_i(3c_{s,i}^2+1)=0, \qquad i=b,\gamma,\nu,c,{\rm BDE}, \qquad (4.20)$$

so dark energy inhomogeneities act as a source term for dark matter perturbations.

Figure (4.4**a**) shows the resulting matter perturbations δ_m(BDE) (baryons + CDM) in the newtonian gauge divided by the corresponding solutions in ΛCDM for modes entering the horizon before, near, and after a_c. Since we will compare these results with the results we will obtain after fitting the data where h (the adimensional Hubble

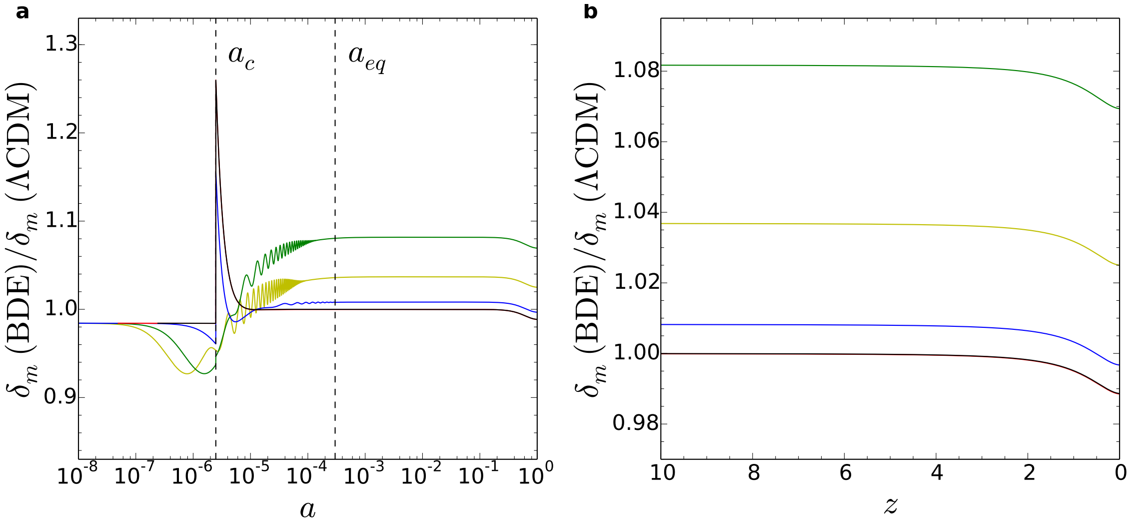

Figure 4.4: (**a**) Quotient of matter perturbations in the newtonian gauge for the BDE and ΛCDM models running with the same set of cosmological parameters for k = 10Mpc^{-1} (yellow), 5Mpc^{-1} (green), 1Mpc^{-1} (blue), 0.05Mpc^{-1} (red), and 0.005Mpc^{-1} (black). The vertical dotted lines mark the condensation epoch a_c and the matter-radiation equality era a_{eq}, respectively. (**b**) Close-up of the ratio of matter perturbations at late times for the modes shown in the left panel.

constant) is different from model to model, we don't use the h factors to express the units of the wavenumber and the power spectrum. Initially, when all modes lie outside the horizon, matter perturbations remain constant as expected, so the ratio is constant too as shown in the left side of the plot. However, we note a small suppression in BDE of about the 1.7%. This suppression is an direct consequence of the effect of the extra relativistic degrees of freedom of the dark group on the gravitational potentials. From the initial condition (1.85) we get:

$$\Psi(\Lambda\text{CDM}) = \frac{20C}{15 + 4R_\nu(\Lambda\text{CDM})} = 1.203C \tag{4.21}$$

$$\Psi(\text{BDE}) = \frac{20C}{15 + 4R_\nu(\text{BDE})} = 1.184C, \tag{4.22}$$

where $R_\nu(\Lambda\text{CDM}) = 0.405$ and $R_\nu(\text{BDE}) = 0.473$ according to expressions (1.36) and (3.22). Since initial δ_c and δ_b depend on δ_γ and δ_γ depends on Ψ, the ratio of the initial matter overdensities are:

$$\frac{\delta_m(\text{BDE})}{\delta_m(\Lambda\text{CDM})} = \frac{\Psi(\text{BDE})}{\Psi(\Lambda\text{CDM})} = 0.984, \tag{4.23}$$

so $\delta_m(\text{BDE}) < \delta_m(\Lambda\text{CDM})$. We now discuss the evolution of matter perturbations. Let's begin with small modes $k > k_c$ (yellow and green curves), where $k_c \equiv a_c H(a_c) = 0.925\text{Mpc}^{-1}$ is the mode entering the horizon at a_c long before the matter-radiation equality. We have seen that matter perturbations grow as $\delta_m \propto \ln a$ during radiation domination. However, the horizon crossing time is not the same for both models. Particularly, these modes enter the horizon earlier in ΛCDM allowing more time the matter overdensities to grow and therefore suppressing further the ratio $\delta_m(\text{BDE})/\delta_m(\Lambda\text{CDM})$. To see this, we take the horizon crossing equation (1.86) *for the same mode* and solve for the ratio $a^h_{\text{BDE}}/a^h_{\Lambda\text{CDM}}$ of the corresponding scale factors at the entrance:

$$k_{\text{BDE}} = k_{\Lambda\text{CDM}} \quad \Rightarrow \quad a^h_{\text{BDE}} H(a^h_{\text{BDE}}) = a^h_{\Lambda\text{CDM}} H(a^h_{\Lambda\text{CDM}}) \tag{4.24}$$

Using equations (4.1) and (4.2) neglecting the matter term and ρ_Λ in ΛCDM we obtain:

$$\frac{1}{a^h_{\text{BDE}}}\sqrt{\rho_{r0} + \rho_{\text{DGc}} a_c^4} = \frac{1}{a^h_{\Lambda\text{CDM}}}\sqrt{\rho_{r0}} \tag{4.25}$$

Therefore:

$$\frac{a^h_{\text{BDE}}}{a^h_{\Lambda\text{CDM}}} = \sqrt{1 + \frac{\rho_{\text{DGc}} a_c^4}{\rho_{r0}}} = \sqrt{1 + \frac{\rho_{\text{DGc}}}{\rho_{rc}}} = 1.062, \tag{4.26}$$

so $a^h_{\text{BDE}} > a^h_{\Lambda\text{CDM}}$. We see then, that this extra suppression effect is also due to the extra relativistic degrees of freedom of the dark group. Once the modes enter the horizon in BDE, the suppression slows eventually halting and then the ratio starts growing. This is simply because during this epoch $\delta'_m \propto \mathcal{H}$ and since $H(\text{BDE}) > H(\Lambda\text{CDM})$ the growth rate of matter fluctuations in BDE is larger. As we have seen, when the phase transition occurs, all the extra amount of radiation due to the particles of the dark group turns into the dark meson representing the dark energy whose equation of state initially leaps to 1 leading to its rapid dilution just after the condensation. The effect of the condensation and the subsequent rapid dilution of the scalar field on the matter perturbations is a mode-dependent boosting of the growth rate which considerably enhances the ratio $\delta_m(\text{BDE})/\delta_m(\Lambda\text{CDM})$. Note that the enhancement effect extends up to the matter equality epoch a_{eq} when the density of the scalar field has decreased to a negligible fraction of the content of the universe $\Omega_{\text{BDE}} \sim 4 \times 10^{-6}$ (c.f. figure (3.1**d**)). Then, during the matter domination era the matter overdensities grow at the same rate in both models as $\delta_m \propto a$, so their ratio keeps constant at the value it has when the rapid dilution ends. Finally, at late times when the dark energy becomes dominant, the larger amount of dark energy in the BDE model (as shown in the right side of figure (4.1)) slows the growth rate of the matter overdensities leading to a slight suppression that can be seen with more detail in figure (4.4**b**). In this case, the late-time suppression effect is mode-independent reducing the ratio $\delta_m(\text{BDE})/\delta_m(\Lambda\text{CDM})$ 1.14% with respect to the constant value in the matter epoch.

Excepting the early suppression effect due to the difference in the horizon crossing

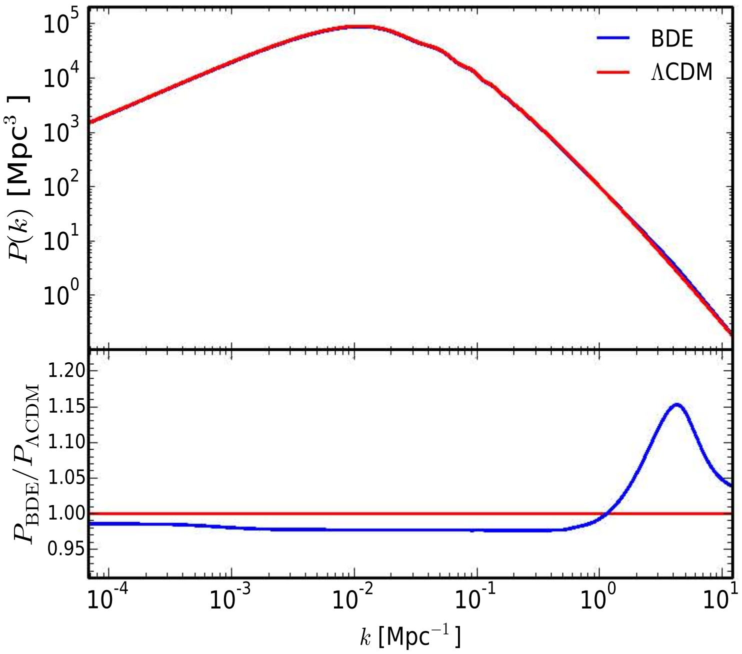

Figure 4.5: Matter power spectrum at $z = 0$ for the BDE (blue) and ΛCDM (red) models running with the same set of basic parameters. The bottom panel shows the ratio with respect to ΛCDM.

time given by equation (4.26), the enhancement of matter perturbations due to the rapid dilution of the scalar field and the suppression effect due to the late-time dynamics of the dark energy are also present in large modes $k < k_c$ (red and black curves) entering the horizon after a_c. However, here the enhancement effect takes place when the modes still lie outside the horizon, and although it is more prominent than for small modes, the effect is transient leaving at the end the perturbations with the same amplitude as ΛCDM, so these curves overlap in the plot. The transient enhancement is also observed for modes entering the horizon shortly before a_c as shown by the blue curve corresponding to $k = 1\text{Mpc}^{-1}$.

The resulting matter power spectrum is shown in figure (4.5). Our model reproduces the shape of the curve and the baryonic wiggles as should be. The bottom panel displays the quotient $P_{\rm BDE}/P_{\Lambda\rm CDM}$. Since both models run with the same primordial spectrum (same n_s and A_s), the differences arise only because of the transfer function (c.f. equations (1.110) and (1.111)). The late suppression effect leaves the BDE spectrum below ΛCDM for $k < 1.14\text{Mpc}^{-1}$, while the rapid dilution effect leaves a bump in the small mode region peaking at $k \approx 4.3\text{Mpc}^{-1}$. Of course, these modes are in the non-linear regime and therefore a non-linear approach needs to be used to study their evolution. However, it is expected [89] that this peak is not completely washed out in N-body simulations [90], opening the possibility of finding results where our model departs significantly from the ΛCDM paradigm.

4.4 The CMB power spectrum

So far we have seen that dark energy affects the CMB temperature anisotropy spectrum through the position of the acoustic peaks and the ISW effect determined by the expansion rate and the variation of the gravitational potential at late times, respectively. Since dark energy evolves differently in BDE and ΛCDM, its effect on the expansion rate and the gravitational potential leads to a change in the position of the peaks and the amount of power in the low multipole region of the spectrum. Moreover, BDE also affects the CMB anisotropies by additional contributions from the scalar field inhomogeneities and the different amount of primordial helium. Figure (4.6) shows the spectrum for both models. The green curve displays the spectrum for BDE when we turn off the dark group and the scalar field perturbations, so that we can evaluate solely the effect of the homogeneous component of the dark energy. For the combination of parameters used in the plot, the sound horizon at decoupling is practically the same (difference $\sim 0.08\%$), so from equation (2.26) the difference in the position of the peaks depends only on the angular diameter distance as:

$$\Delta l_n = \frac{n\pi}{2r_s(z_*)}(1+z_*)[D_A^{\mathrm{BDE}}(z_*) - D_A^{\Lambda\mathrm{CDM}}(z_*)] \tag{4.27}$$

Since $H(\mathrm{BDE}) > H(\Lambda\mathrm{CDM})$ and $D_A(\mathrm{BDE}) < D_A(\Lambda\mathrm{CDM})$ as we found in section (4.1), we get $l_n(\mathrm{BDE}) < l_n(\Lambda\mathrm{CDM})$. This means that the CMB spectrum in ΛCDM is shifted to the right towards smaller angular scales [72]. The shift is almost not visible in the plot due to the width of the curves, but it is clearly seen in the oscillations of the residuals ΔD_l^{TT} in the bottom panel. The amplitude of the ISW effect depends on the background history and the presence of dark energy perturbations [73, 74]. Let's first consider the effect of the homogeneous component of BDE. Since we are running the models with the same content of matter and current expansion rate H_0, $\rho_{\mathrm{BDE}}(a) > \rho_\Lambda$ as we previously found. This implies that the matter-dark energy equality epoch occurs later in BDE, so the the interval where the gravitational potential varies over the time ($\Phi' \neq 0$) is shorter in BDE and the contribution to the ISW integral (c.f. equation (2.22)) is smaller [73], leading to less power than ΛCDM as shown by the green curve. On the other hand, it has been found [73, 74] that when we include dark energy perturbations, the ISW source term Φ' becomes larger in models where $w_{DE} > -1$ as a result of matter growth suppression at late times, leading to an enhancement of the CMB power that overcomes the effect caused by the background that we have just discussed. This is the case for the BDE model, where the dark energy equation of state lies above -1 and the matter

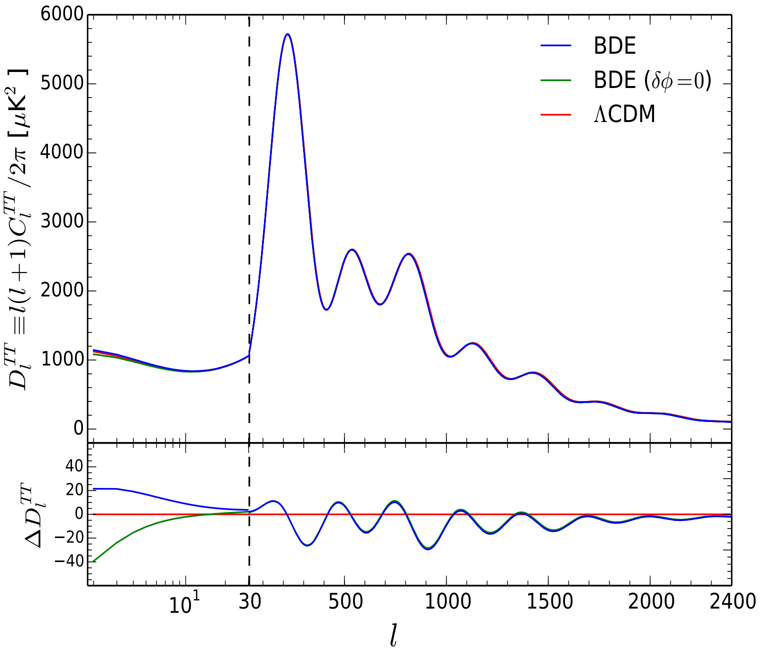

Figure 4.6: CMB temperature anisotropy spectrum for the BDE (blue) and ΛCDM (red) models. The green curve shows the spectrum for BDE when we turn off the perturbations of the dark group and the scalar field. We use a logarithmic scale for multipoles between $2 \leqslant l \leqslant 30$ and then a linear scale for higher multipoles (vertical dashed line). The bottom panel shows the residuals $\Delta D_l^{TT} \equiv D_l^{TT} - D_l^{TT}(\Lambda\text{CDM})$.

fluctuations grow slowlier than ΛCDM at late times as seen in figures (3.1**c**) and (4.4**b**), respectively. Here we get more power in the low multipole region of the spectrum as shown by the blue curve in the plot.

Although the extra relativistic degrees of freedom due to the dark group vanish once the BDE condensation occurs and therefore they don't exert direct influence on the physical processes involved in recombination, the enhanced fraction of primordial helium left by this extra early radiation modifies the damped tail of the CMB spectrum. The damping factor [36]:

$$D_\gamma(k) = \int_0^{\tau_0} d\tau \; \tau'_{op} e^{-\tau_{op}} e^{-[k/k_D(\tau)]^2} \tag{4.28}$$

depends on the optical depth τ_{op} and the damping wavenumber k_D which is inversely proportional to the root square of the number density of free electrons n_e, $k_D \propto 1/\sqrt{n_e}$ [29]. Since the ionization energy of neutral helium is higher than hydrogen, an enhanced amount of primordial helium reduces the number of free electrons left before recombination starts, so $k_D(z_*)$ and $e^{-[k/k_D(z_*)]^2}$ get smaller, which leads to a more damped spectrum [91, 92]. Unlike the ISW effect, the damping of the CMB spectrum occurs at small angular scales at large multipoles. In figure (4.6) we see that the extra damping of the spectrum in the BDE model due to the enhanced production of primordial helium manifests at $l \gtrsim 1000$, where BDE lies below ΛCDM.

Chapter 5

Constraints

So far we have studied the dynamics of the dark energy in the BDE model and its cosmological implications. However, in order to determine under which conditions our model provides a realistic account of the history of the universe, we need to constrain its parameters through observational evidence. In this chapter we analyse how BDE fits the data and how its constraints compare with those of ΛCDM. In general, when we fit two models to the observations, the resulting constraints on the parameters are different from model to model and we expect to find some tensions which give us the possibility to discriminate between them. In section (5.1) we document the modifications to the codes we used to implement our analysis and we show the constraints that result from the datasets we considered. The rest of the chapter is aimed to explore the consequences of such constraints. Note that in this case the BDE and the ΛCDM models run with their own best fit parameters, so now the discrepancies arise not only because of the different dynamics of the dark energy, but also because the matter and the dark energy content of the universe at present time, and the primordial power spectrum in the early universe is not necessarily the same. In section (5.2) we discuss the implications of the constraints we found on the background history of the universe, the expansion rate and the fits to the SNeIa and BAO data. In section (5.3) we revisit the growth of matter perturbations and study the predictions on the power spectrum and the parameters that characterise structure formation . We also outline the predictions on the mass function according to the Press-Schechter theory. Then, in section (5.4) we assess the consistency between the expected fraction of primordial helium and deuterium with current astrophysical bounds. Finally, we end our analysis in section (5.5) by discussing the fit of our model to the CMB temperature anisotropy spectrum measurements.

5.1 Constraints

5.1.1 CAMB

The Code for Anisotropies in the Microwave Background (`CAMB`) [37] is a program used for computing the CMB anisotropy and the matter power spectra by solving the perturbation equations for each one of the cosmological fluids up to linear order. The code is based on `CMBFAST` [93] written by Uros Seljak and Matias Zaldarriaga and it has been updated almost 60 times since the original release was launched in 1999. The modular architecture of the program makes easier to adapt the code to the user's specific needs since all the modules, subroutines, and functions are distributed in different files with minimum dependencies. Among the main features of the software we may quote:

- written in fortran 90. The code is available at http://camb.info; The installation on a linux machine is straightforward.
- all the calculations are performed in the synchronous gauge. The recent versions incorporate a python wrapper that makes easy the transformation of quantities into the newtonian gauge.
- support for scalar, vector, and tensor perturbations.
- support for flat and curved geometries.
- inclusion of different types of initial conditions.
- implementation of special modules for non-standard cosmologies, such as time-varying dark energy equation of state, massive neutrinos, and quintessence.

In this work we use the November 2016 release and the base code `equations_quint.f90` for standard quintessence. The main modifications we made to the code are:

- *Background equations.* The Klein-Gordon (3.39) and the Friedmann (3.40) equations are implemented as the system of equations (3.54)-(3.56) with initial conditions (3.59)-(3.61). However, the numerical integrator routine `dverk` available in `CAMB` probes to be useless because of the initial drop of y depicted in figure (3.1**a**). We solve this difficulty by implementing the equations in a python script where we use the `odeint` solver of the `scipy` library. The solutions thus obtained are in agreement with other powerful integrators such as those available in `Mathematica`.
- *H_0 and the dark energy EOS.* Since in the BDE model H_0 is not a free parameter but a derived quantity, we implement the proper code to compute it. In terms of

the BDE density parameter and the physical densities of matter and radiation, H_0 is given from equation (3.40) by:

$$H_0 = 10^2 \sqrt{\frac{\Omega_r h^2 + \Omega_m h^2}{1 - \Omega_{\mathrm{BDE0}}}} \text{ km s}^{-1}\text{Mpc}^{-1}, \tag{5.1}$$

where Ω_{BDE0} is determined by the solution for x and y at $z = 0$ as stated in equation (3.46):

$$\Omega_{\mathrm{BDE0}} = x_0^2 + y_0^2 \tag{5.2}$$

Analogously, from equation (3.47) the BDE equation of state at $z = 0$ is simply:

$$w_{\mathrm{BDE0}} = \frac{x_0^2 - y_0^2}{x_0^2 + y_0^2} \tag{5.3}$$

- *Perturbation equations.* We implement the perturbation equations before and after the phase transition (4.6)-(4.10) and (4.13)-(4.17) within the subroutine `derivs` in `equations.f90`. The initial conditions of the scalar field inhomogeneities are set according to equations (3.74). In the code, we match δ_{DG} with δ_{BDE} at a_c in the subroutine `CalcScalarSources` in `cmbmain.f90`.

- *Additional outputs.* Besides the usual outputs of the program, to wit, the CMB and the matter power spectra and the transfer functions, we implement additional code to retrieve useful information such as the luminosity and the angular diameter distances (eqs (2.1) and (2.14)), the distance modulus (eq.(2.10)), the BAO ratio (eq.(2.15)), and the root mean square of matter fluctuations in linear theory (eq.(5.8)).

5.1.2 CosmoMC

The Cosmological Monte-Carlo (`CosmoMC`) code [94] is a Markov-Chain Monte-Carlo engine used to explore and constrain the parameter space of a cosmological model using observational data. Like `CAMB`, `CosmoMC` is built on a modular architecture scheme reducing the number of dependencies across the code and thus helping to adapt the program to the user's needs. The code has been developed in close connection with `CAMB` and the dataset releases from different experiments and has been updated 47 times since its first version launched in November 2002. Among the main features of the software we may quote:

- written in fortran 90. The code is available at http://cosmologist.info/cosmomc; a very useful installation guide is found in [95].

- optimized to run in parallel with `OpenMP`. This allows to explore efficiently the parameter space within acceptable computational times by exploiting the facilities of multiprocessor machines and clusters.

- implementation of two sampling methods: a vanilla Metropolis algorithm and a fast-slow dragging algorithm specially efficient for Planck runs [96]. Other sampling methods such as slice sampling and directional gridding that were available in previous versions have not been updated in the last actualizations.

- support for different tasks (actions): sampling of the parameter space via Monte-Carlo Markov chains, best fit point determination, importance sampling, and fast calculation of the likelihood for a specific combination of parameters.

- support for different cosmological probes: SNeIa, BAO, CMB temperature, polarization and lensing spectra, local H_0, weak lensing, large scale distribution of large red galaxies, and primordial helium and deuterium abundances. For most of these probes there are multiple datasets provided by different collaborations (e.g., Union, SNLS and JLA for SNeIa; WMAP and Planck for CMB and so on)

In our analysis we use the November 2016 version. The main modifications we made to the code are:

- *The cosmological model.* We replace the `CosmoMC` default distribution of `CAMB` with our implementation of the BDE model described above.

- *Basic and derived parameters.* We recall that the number of basic parameters of the ΛCDM model are six. These can be chosen as: the present physical densities of baryons and cold dark matter $\Omega_b h^2$ and $\Omega_c h^2$, respectively, the present expansion rate H_0 (or $100\theta_{\rm MC}$ according to the Planck collaboration, see below), the amplitude of the primordial curvature perturbations A_s, the spectral scalar index n_s, and the reionization optical depth τ. However, in our BDE model H_0 is not a free parameter but a derived since it is determined by the present day dark energy density which in turn depends on the condensation scale Λ_c through the initial conditions (3.59)-(3.61) as shown in equation (5.1). Therefore, we don't use H_0 to sample the parameter space thus reducing in principle the number of basic parameters to five. Nevertheless, we remark that although Λ_c is a quantity whose value is given by the colours N_c and the massless fields N_f of our dark group, the unification scale Λ_{gut}, and the unified coupling strength g_{gut}, a precise value of Λ_c is still unknown because of the uncertainties of the latter two [84, 97]. Consequently, in spite of not being a free parameter of the model, we allow Λ_c to vary freely from 10^{-3} to 10^3 eV much wider than the theoretical estimations of equation (3.29). Hence, the set of basic parameters we use in `CosmoMC` for our BDE model are: $\Omega_b h^2$, $\Omega_c h^2$, Λ_c, A_s (more precisely, $\log(10^{10}As)$), n_s, and τ. For all them we assume wide flat priors to assert a complete exploration of the tails of the posterior distributions, the convergence of the chains and the location of the best fit point [98]. The epoch of the phase transition (a_c) and the energy density of the BDE field at that time are obtained from equations (3.20) and (3.58), respectively; once we solve for the dynamical variables x, y, and λ (c.f. equations (3.44) and (3.45)) we get the present value of the equation of state $w_{\rm BDE0}$, the density parameter $\Omega_{\rm BDE0}$, and H_0 according to equations (5.1)-(5.3). On the other hand, we use the `CosmoMC` interpolation tables prepared with the `PArthENoPE` code [86] to get the abundances of primordial helium ($Y^P_{\rm BBN}$) and deuterium ($10^5 D/H$) formed during Big Bang Nucleosynthesis from $\Omega_b h^2$ and the number of extra relativistic degrees of freedom (N_{ext}) given by (3.24).

- *Relation between H_0 and θ_{MC}.* The angular size of the sound horizon at recombination (θ_*) is well approximated by:

$$\theta_{\rm MC} = \left(\int_{10^{-8}}^{a_s} da/[\dot{a}\sqrt{3(1+R)}]\right) / \left(\int_{a_s}^{1} da/\dot{a}\right) \quad ; \quad R = \frac{3}{4}\cdot\frac{\rho_b(a)}{\rho_\gamma(a)} \tag{5.4}$$

where $a_s = 1/(1+z_s)$ [99]:

$$z_s = 1048 * \left(1 + 0.00124(\Omega_b h^2)^{-0.738}\right) * (1 + g_1(\Omega_m h^2)^{g_2}), \tag{5.5}$$

$$g_1 = \frac{0.0783(\Omega_b h^2)^{-0.238}}{1+39.5(\Omega_b h^2)^{0.763}},$$

$$g_2 = 0.560/[1 + 21.1(\Omega_b h^2)^{1.81}]$$

In the `CosmoMC` default implementation of the ΛCDM model, $\theta_{\rm MC}$ (more precisely, $100\theta_{\rm MC}$) is used as a basic parameter instead of H_0 to sample the parameter space, since θ_* is better constrained [25, 26]. H_0 is thus determined through its implicit relation with $\theta_{\rm MC}$ in equation (5.4) by a binary search which finds the value of h consistent with the proposal of $100\theta_{\rm MC}$ made by the sampling algorithm. In the BDE model there is no need of such procedure because as we have seen the initial conditions (3.59)-(3.61) determine the expansion rate at all times and so both H_0 and $\theta_{\rm MC}$ are directly obtained from the background solution through equations (5.1) and (5.4). In the code, these changes are implemented in the `TP_ParamToTheoryParams` subroutine in `CosmologyParameterizations.f90`.

5.1.3 Datasets

Our analysis includes measurements of the CMB temperature anisotropy spectrum, the BAO signal, and the luminosity distance of well-identified type Ia supernovae. At present time, these data provide the most robust constraints since they are less affected by experimental systematics and theoretical assumptions in comparison with other probes. For example, local H_0 measurements are sensitive to calibration systematics leading to discrepant results with respect to the CMB [63]; the estimations on primordial light element abundances rely strongly on nuclear cross sections and the neutron mean life, which is still unknown with enough accuracy [87]; weak lensing calculations are affected by non-linear dynamics [100], and the constraints from LSS galaxy surveys depend on the bias between the visible and dark matter [101]. Therefore, the results we report in this work are only based on recent, uncontroversial and accurate observations available at present. The datasets we considered were:

- *The Planck 2015 CMB temperature spectrum (Planck TT).* These are the measurements of the temperature anisotropy power spectrum $D_l^{TT} \equiv l(l+1)C_l^{TT}/2\pi$ released by the Planck collaboration in 2015 [102]. The baseline dataset covers the multipole region $l = 2 - 2508$ divided into a low and a high-l subsamples ranging from $l = 2 - 29$ and $l = 30 - 2508$, respectively. The release includes a supplementary code for computing the likelihood using a different algorithm in each subsample[1].

- *The Joint Light-curve Analysis sample (JLA).* This catalog contains the measurements of the luminosity distance of 740 confirmed type Ia supernovae in the redshift range $0.01 \lesssim z \lesssim 1.3$ compiled mainly from the SDSS-II survey, the first three seasons of the SNLS project, and the Harvard Smithsonian Center for Astrophysics (CfA) [41].

- *The BOSS Data Release 12 (DR12)* measurement of the BAO scale extracted from two samples called LOWZ and CMASS which contain 361 762 galaxies mapped in the range $0.15 \leqslant z \leqslant 0.43$ with an effective redshift of $z_{\rm LOWZ} = 0.32$ and 777 202 galaxies between $0.43 \leqslant z \leqslant 0.70$ with an effective redshift of $z_{\rm CMASS} = 0.57$, respectively [50].

- *The Main Galaxy Sample (MGS)* measurement of the BAO scale taken from the SDSS Data Release 7 with selected galaxies at a lower redshift than BOSS $z < 0.2$ with an effective redshift of $z_{\rm MGS} = 0.15$ [52].

- *The 6dF Galaxy Survey (6dF)* measurement of the BAO scale taken from a sample of 75 117 galaxies at an effective redshift of $z_{\rm 6dF} = 0.106$ [51].

5.1.4 Results

Table (5.1) lists the mean with the 68% confidence limits (CL), the best fit values of selected parameters and the goodness of fit (χ^2) for each model.

---

[1] For more details, see the Planck 2015 Release Explanatory Supplement available at https://pla.esac.esa.int/pla/#home

Table 5.1: Best fit, mean and 68% confidence limits for the BDE and ΛCDM models from the Planck 2015 temperature spectrum [26] in combination with the JLA type Ia supernovae catalog and the measurements of the BAO scale from the DR12-LOWZ, DR12-CMASS [50], MGS [52] and 6dF [51] samples.

	BDE		ΛCDM	
Parameter	Best fit	68% limits	Best fit	68% limits
Λ_c [eV]	44.02	44.09 ± 0.28	—	—
$10^6 a_c$	2.48	2.48 ± 0.02	—	—
Ω_{BDEc}	0.1117	0.11174 ± 0.00001	—	—
$\Omega_b h^2$	0.02252	0.02257 ± 0.00021	0.02243	0.02238 ± 0.00021
$\Omega_c h^2$	0.1173	0.1171 ± 0.0013	0.1181	0.1182 ± 0.0012
$100\theta_{\mathrm{MC}}$	1.04106	1.04112 ± 0.00043	1.04113	1.04112 ± 0.00042
$\ln(10^{10} A_s)$	3.164	$3.179^{+0.055}_{-0.048}$	3.165	3.150 ± 0.052
n_s	0.9774	0.9780 ± 0.0050	0.9710	0.9701 ± 0.0049
τ	0.117	$0.124^{+0.028}_{-0.025}$	0.118	0.110 ± 0.027
H_0 [km s^{-1}Mpc^{-1}]	67.68	67.82 ± 0.55	68.64	68.57 ± 0.58
Ω_{DE0}	0.695	0.696 ± 0.007	0.702	0.701 ± 0.007
Ω_m	0.305	0.304 ± 0.007	0.298	0.299 ± 0.007
w_{DE0}	-0.9296	-0.9294 ± 0.0007	-1	-1
$\sigma_8(z=0)$	0.8551	0.861 ± 0.022	0.8707	0.864 ± 0.022
Age [Gyr]	13.74	13.74 ± 0.03	13.75	13.75 ± 0.03
$H(0.57)$ [km s^{-1}Mpc^{-1}]	94.04	94.12 ± 0.31	93.53	93.49 ± 0.29
$r_{\mathrm{drag}}/D_V(0.57)$	0.07238	0.07248 ± 0.00044	0.07230	0.07228 ± 0.00043
$f\sigma_8(0.57)$	0.4883	0.491 ± 0.012	0.5013	0.498 ± 0.012
$\sigma_8(0.57)$	0.6396	0.644 ± 0.017	0.6507	0.646 ± 0.017
z_{rei}	13.2	$13.7^{+2.3}_{-1.7}$	13.2	$12.5^{+2.4}_{-1.8}$
z_{drag}	1060.51	1060.58 ± 0.47	1059.93	1059.82 ± 0.47
r_{drag} [Mpc]	147.52	147.54 ± 0.34	147.53	147.56 ± 0.34
z_*	1089.98	1089.90 ± 0.32	1089.68	1089.75 ± 0.32
$r_s(z_*)$ [Mpc]	144.89	144.91 ± 0.32	144.88	144.89 ± 0.31
$D_{\mathrm{A}}(z_*)$ [Gpc]	13.92	13.92 ± 0.03	13.91	13.92 ± 0.03
z_{eq}	3342	3338 ± 29	3359	3360 ± 29
k_{eq} [Mpc^{-1}]	0.0102	0.01019 ± 0.00009	0.0103	0.01025 ± 0.00009
k_D [Mpc^{-1}]	0.1400	0.13998 ± 0.00045	0.1404	0.14037 ± 0.00045
Y_P^{BBN}	0.2588	0.2588 ± 0.0001	0.2467	0.2467 ± 0.0001
$10^5 D/H$	2.89	2.88 ± 0.04	2.58	2.59 ± 0.04

$\chi^2(\mathrm{BDE}) = 5.609$ (BAO) + 776.510 (CMB) + 695.668 (SNeIa) + 1.833 (prior) = 1479.621

$\chi^2(\Lambda\mathrm{CDM}) = 7.115$ (BAO) + 776.884 (CMB) + 695.075 (SNeIa) + 1.681 (prior) = 1480.754

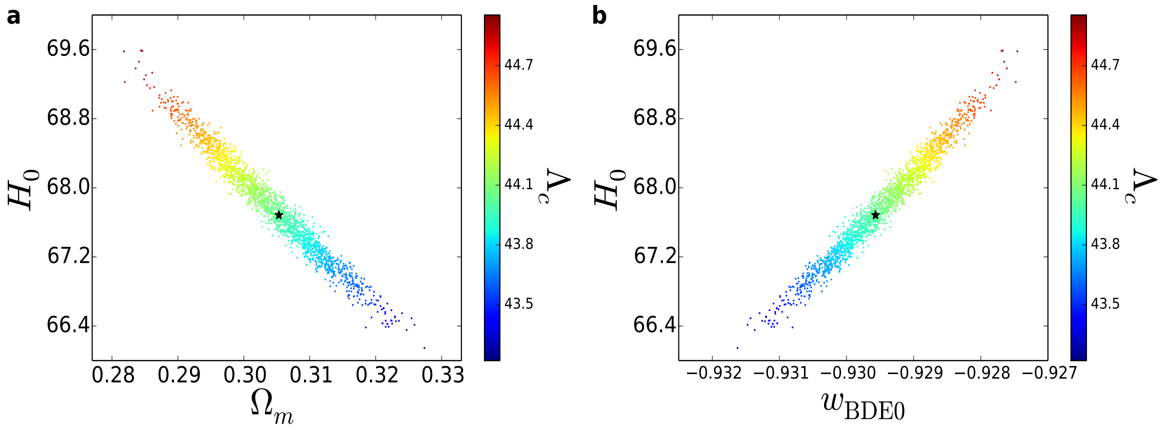

Figure 5.1: Samples in the $\Omega_m - H_0$ (**a**) and $w_{\rm BDE0} - H_0$ (**b**) planes coloured by the condensation scale Λ_c. The stars mark the location of the best fit point.

The first three parameters are the characteristic quantities of our BDE model. Then we have the six ΛCDM base parameters; the next six describe the present state of the universe followed by the constraints on late-time quantities ($z = 0.57$) that can be inferred from LSS, BAO, and SNeIa observations. Then we proceed to earlier times, namely, the reionization epoch (z_{rei}), the baryon drag, recombination, the matter-radiation equality and finally we end up with the theoretical estimations on the abundances of primordial helium and deuterium formed during BBN. For the sake of comparison we include the constraints on the ΛCDM model using the same datasets. In each case, we performed the parameter space exploration with eight Markov chains long enough to satisfy the Gelman-Rubin convergence diagnostics $R - 1 < 0.01$, leaving about 136K samples after a burn-in period of 30% [98]. We also ran two more realisations leading to the same results. When fitting to the data, we performed several runs starting from different initial positions in the parameter space ensuring the stability of the best fit point [98].

The constraints on Λ_c lie within the theoretical estimations (3.29). From the best fit values we see that the phase transition takes place well within the radiation era nearly 5 $e-$folds before the matter-radiation equality, when the temperature of photons is $T_\gamma(a_c) = 2.7255K/a_c = 94.7$eV and the density of radiation and matter is $\Omega_{rc} = 0.881$ and $\Omega_{mc} = 0.007$, respectively. Figure (5.1) shows the effect of Λ_c on the current expansion rate, the matter content, and the equation of state. We see that larger values of Λ_c lead to larger H_0 and $w_{\rm BDE0}$ and smaller Ω_m, the former two being tightly constrained. Note that the results for H_0 are still in tension with recent local measurements such as $H_0 = 73.24 \pm 1.74\ {\rm km \cdot s^{-1} Mpc^{-1}}$ [63] reinforcing the suggestion that the origin of this discrepancy may be not in the cosmological model but in the datasets themselves.

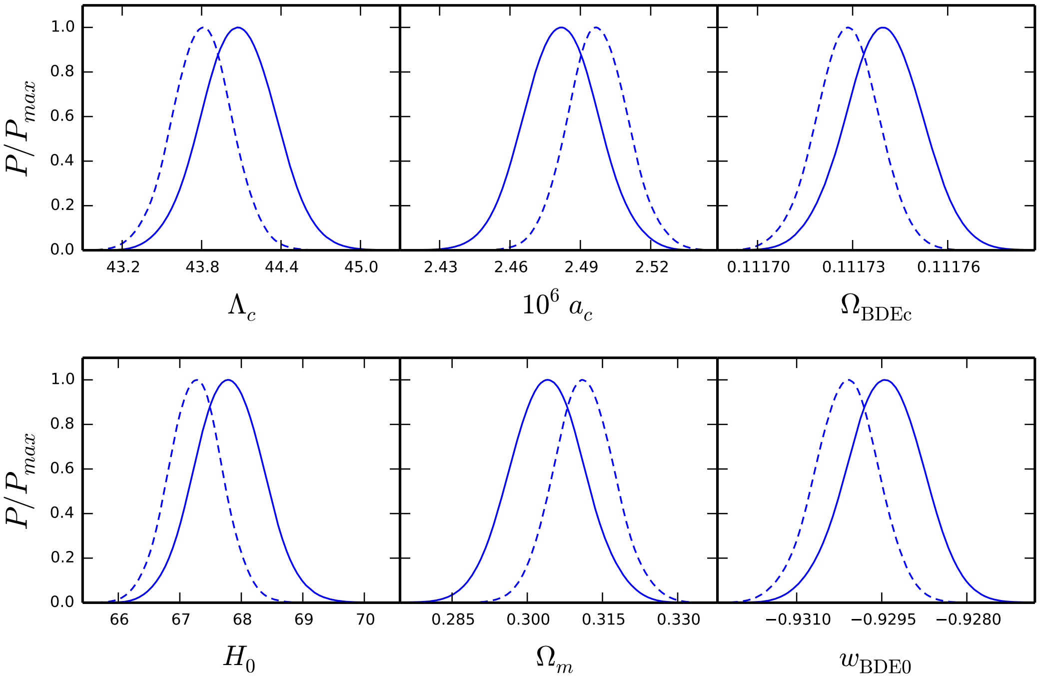

Figure 5.2: Effect of the polarization measurements of the CMB on the parameter constraints for the BDE model. The solid lines are the marginal distributions from the combination Planck TT + JLA + BAO datasets listed in section (5.1.3); the dashed lines are obtained by replacing Planck TT with polarization data lowP + TT, TE, EE [102]. LowP measurements include the cross-spectra TT, TE, EE, TB, EB, and BB in the range $l = 2 - 29$, while TT, TE, and EE data cover the range $l = 30 - 1996$.

We can assess the robustness of our constraints by including additional datasets or by testing specific features of the model. In the former case, figure (5.2) shows the marginal distributions of the parameters of BDE as well as H_0, $\Omega_{\rm BDE0}$, and $w_{\rm BDE0}$ when we include measurements of the CMB polarization in the range $l = 2-1996$ [102]. The condensation scale Λ_c is slightly smaller and consequently the phase transition occurs later according to equation (3.20). However, the marginal limits of these and the other parameters still agree at the 1σ level. On the other hand, we test our constraint of equation (3.20) by allowing a_c and Λ_c to vary freely and independently. In this case, we find for the best fit $\Lambda_c = 44.06$eV and $a_c = 2.48 \times 10^{-6}$, which lead to $a_c\Lambda_c/\text{eV} = 1.0916 \times 10^{-4}$ deviating from (3.20) only by 0.2%.

Except for the abundances of helium and deuterium, the marginal limits for BDE and ΛCDM agree at the 1σ level. However, we can see that the BDE model fits better the data since $\chi^2(\text{BDE}) < \chi^2(\Lambda\text{CDM})$ and the number of basic parameters varied in `CosmoMC` are the same. In this regard, we recall that a direct comparison between the

Table 5.2: Goodness of fit of the BDE and ΛCDM models for the datasets analysed in this work.

Dataset	χ^2(BDE)	χ^2(ΛCDM)
Planck TT low-l	14.462	15.822
Planck TT high-l	762.049	761.062
JLA	695.668	695.075
DR12-LOWZ	0.411	0.508
DR12-CMASS	3.520	4.389
MGS	1.677	2.194
6dF	0.002	0.025

goodness of fit of two models does not necessarily tell if a model is more appealing than the other: a model A with more basic parameters than a model B leads in general to $\chi^2(A) < \chi^2(B)$, but the reduction of χ^2 is obtained at the expense of the simplicity of the underlying theory [103]. In order to make a fair comparison it is important to compute the reduced χ^2 or consider some information criteria which penalize the introduction of additional parameters [103]. In our case, since the number of varied parameters of BDE is the same than ΛCDM, we are not introducing any extra free parameters and so a direct comparison of χ^2 may serve to evaluate the performance of our model. Table (5.2) shows the details of the fits. We see that the performance for the CMB and SNeIa data are very similar, but there are significant reductions in χ^2 for the BAO measurements ranging from 19% for LOWZ and CMASS to 92% for 6dF. Clearly, the BAO information favours a dynamical dark energy model.

Figure (5.3) shows the joint constraints on the six base ΛCDM parameters coloured by the condensation scale. We see that most of the samples lie within the 2σ contours (in red) of ΛCDM. However, the samples with large Λ_c (from orange to red points) fall outside the contours, the effect markedly observed when the physical density of cold dark matter $\Omega_c h^2$ is involved. Although the constraints on these parameters agree within the 1σ level it is interesting to consider the combinations with other parameters such as H_0 and Ω_m as shown in figure (5.4). The contours for $\Omega_b h^2$ and A_s still agree within the 1σ level; we observe slight tensions with n_s, and there are tensions at more than 2σ level with $\Omega_c h^2$ and the BAO ratio at $z = 0.57$, where our model fits better the data than ΛCDM. These tensions are not observed in all dynamical dark energy models. Figure (5.5) shows the results for a dark energy model with a CPL equation of state $w(a) = w_0 + w_a(1 - a)$ [104, 105] where the contours are wide enough to embrace the ΛCDM constraints. Undoubtedly, it will be interesting to monitor the results of future

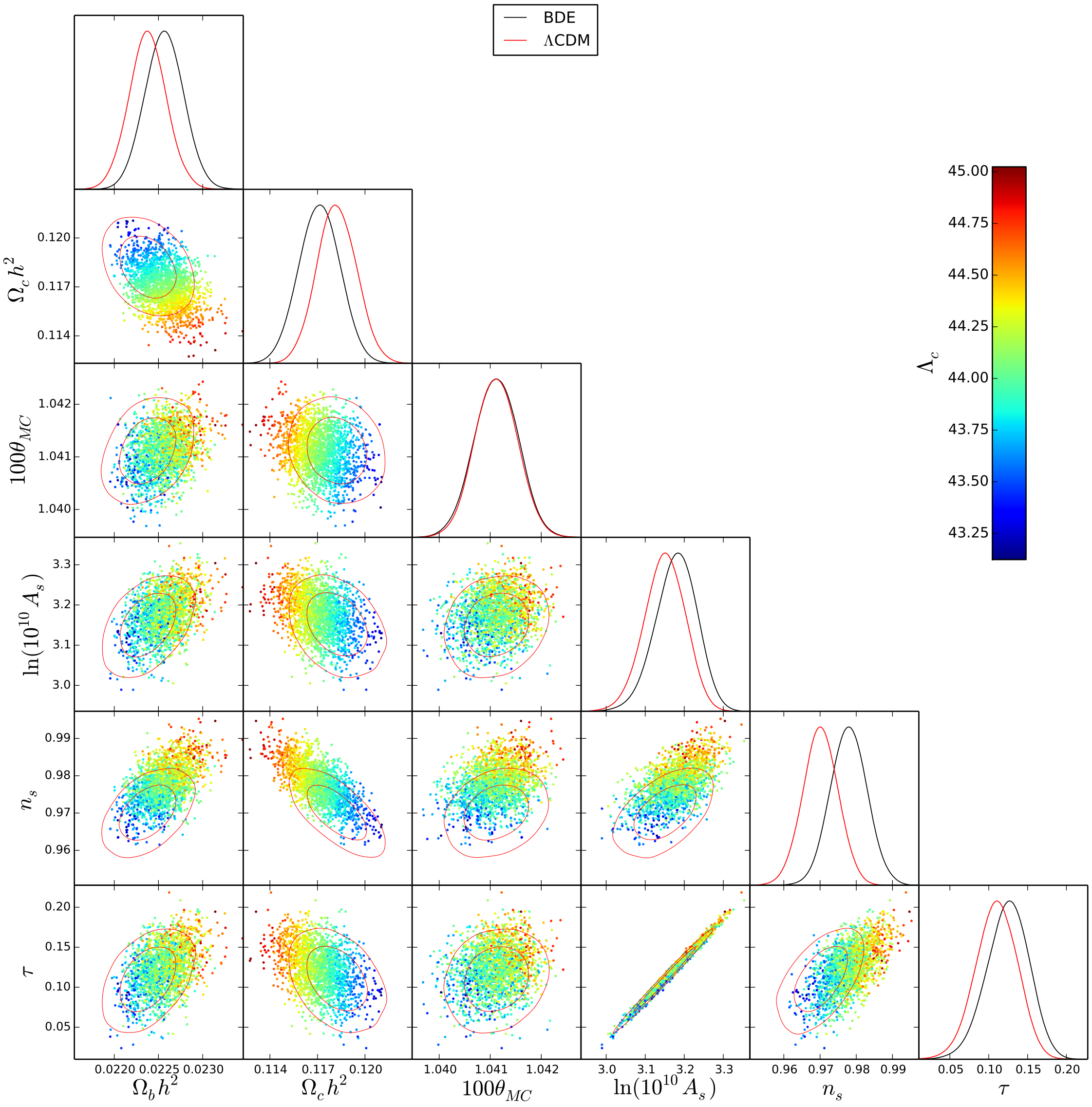

Figure 5.3: Joint constraints on the six base ΛCDM parameters coloured by the condensation scale Λ_c. The red lines mark the 68% and 95% confidence contours for the ΛCDM model.

galaxy surveys such as DESI to see if the tension between ΛCDM and BDE remains and if BDE still fits better the data not only at a single redshift. If so, this would be a suggestive evidence for a time-varying equation of state.

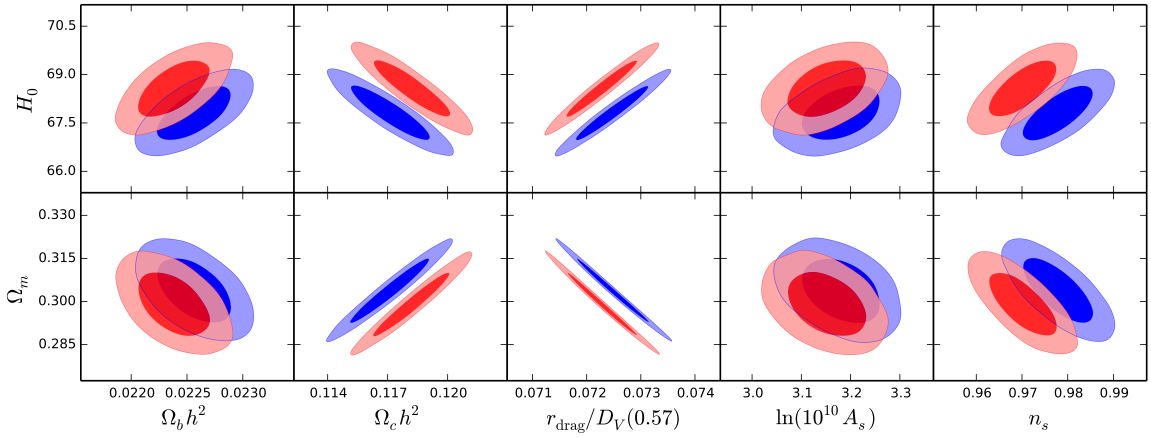

Figure 5.4: Joint constraints on the current expansion rate (H_0) and the matter content (Ω_m) with the physical densities of baryons and CDM, the BAO ratio at $z = 0.57$, the amplitude of the primordial curvature perturbations, and the spectral scalar index for BDE (blue) and ΛCDM (red).

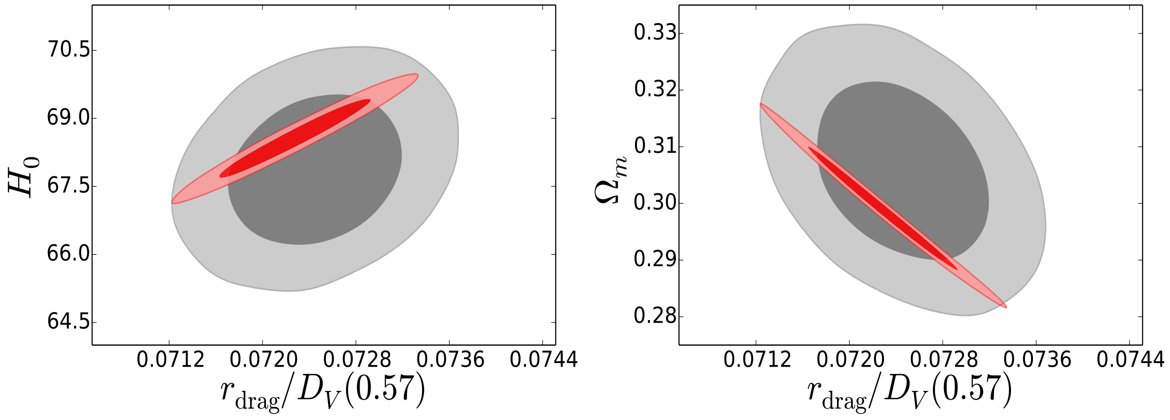

Figure 5.5: 68% and 95% contours in the $r_{\rm BAO}(z = 0.57) - H_0$ and $r_{\rm BAO}(z = 0.57) - \Omega_m$ planes from the datasets considered in this work for a CPL model (grey) and ΛCDM (red).

5.2 Background evolution and cosmological distances

The preceding analysis set the limits on the parameter space where the BDE and ΛCDM models are consistent with the datasets we are considering. In the following sections we use these constraints to track the cosmological evolution in each model, looking to identify the departures from the ΛCDM scenario where future observations might provide evidence in favour of some model. Note that unlike the previous chapter, we now run the models with their specific fitting values so besides the inherent differences due to the dynamics, there is now an additional effect due to the difference in the parameter values with which the models run.

Figure (5.6**a**) shows the evolution of the BDE equation of state for the best fit point. As we have already mentioned, before the phase transition the dark group evolves as radiation so $w_{\rm BDE}(a < a_c) = 1/3$. When the condensation occurs, the equation of state leaps to 1 and lies at this value up to a time shortly after the decoupling epoch a_*. Then it drops to -1 behaving as a cosmological constant for most of the cosmic time and finally it starts growing in the recent past to reach $w_{\rm BDE0} = -0.93$ at present. Figure (5.6**b**) displays the late-time behaviour of the equation of state. The grey band marks the 95% C.L. obtained with the Markov chains. From the thickness of the band and the distribution of the samples in the $w_{\rm BDE0} - H_0$ plane of figure (5.1**b**), we see that the equation of state in BDE is tightly constrained, so we can draw accurate conclusions from the best fit alone. The bounds we obtain are $w_{\rm BDE} \leqslant -0.99, -0.95$ for $10^2 > z \geqslant 1.8, 3.5$, respectively and $w_{\rm BDE}(z_{DE}) = -0.949$ in the matter-dark energy equality epoch $z_{DE} = 0.339$. This happens shortly after $z_{eff} = 0.650$ where the equation of state reaches the mid point between -1 and its current value:

$$w_{\rm BDE}(z_{eff}) = \frac{-1 + w_{\rm BDE0}}{2} = -0.965 \tag{5.6}$$

with a rate of change of $\frac{dw}{dz}(z_{eff}) = -1.26$. The effect on the evolution of the dark energy density is shown in figure (5.6**c**) where we also display the matter, radiation and the dark energy density as a cosmological constant for the best fit. Since the particles of the dark group redshift as a^{-4} and they amount to an important fraction of the energy content of the early universe varying from 30% at the unification scale (c.f. equation (3.5)) to 11% after the neutrino decoupling (c.f. equation (3.18)), their energy density evolves closely to the standard radiation as depicted in the plot. Then, the BDE component quickly dilutes as a result of the equation of state $w_{\rm BDE} = 1$ just after the phase transition as we previously discussed in section (3.3). The rapid dilution of the scalar field proceeds until the equation of state drops to -1 some time after recombination. The dark energy density reaches a minimum value and then keeps at this value mimicking the evolution of a cosmological constant. However, since the matter and radiation are diluting, the density parameter $\Omega_{\rm BDE}$ grows monotonically as shown in figure (3.1**d**), but even so during this period the dark energy is still subdominant. Finally, the late-time growth of the equation of state produces a slight further dilution of the dark energy density as can be seen in figure (5.6**d**), where the crossing with the matter density at $z_{DE} = 0.339$ marks the beginning of the dark energy dominance epoch. We obtain the bounds $\Omega_{\rm BDE} \leqslant 1\%, 0.1\%$ for $z \geqslant 5.3, 12.7$, respectively. It is hardly to overemphasize the conceptual differences and the observational consequences that this scenario implies

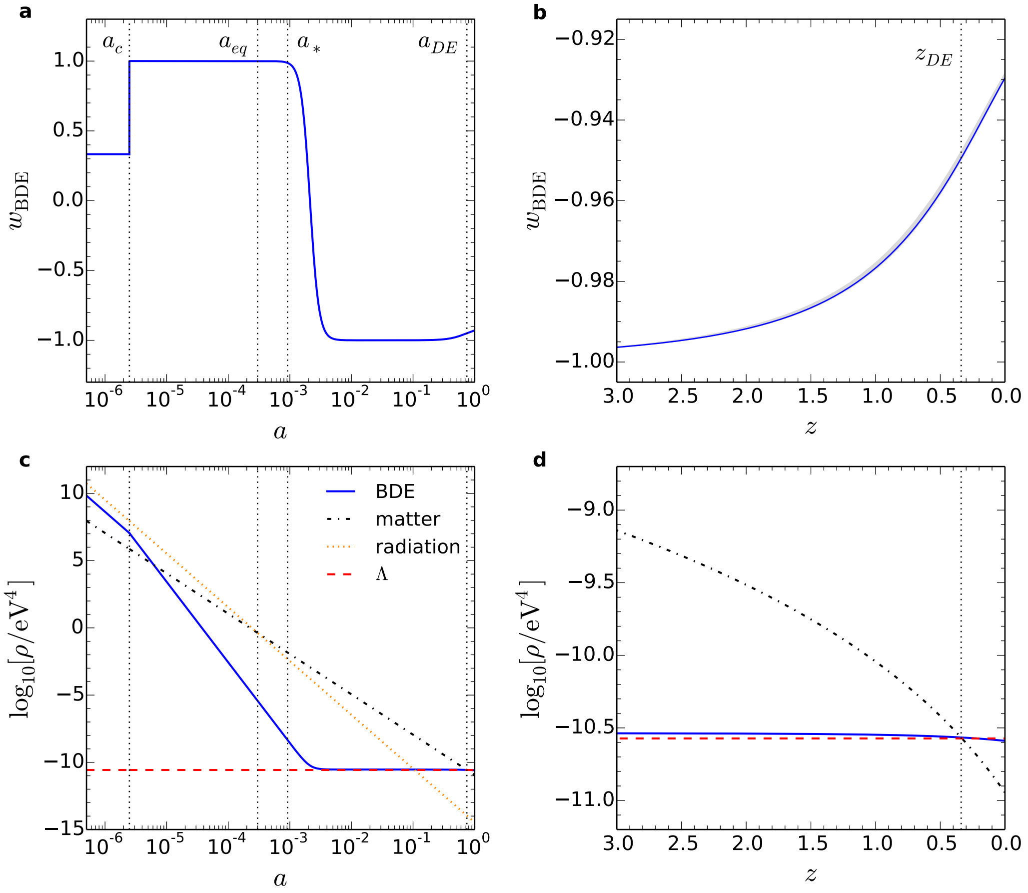

Figure 5.6: (**a**) Evolution of the equation of state for the best fit BDE model. The vertical dotted lines mark the condensation epoch (a_c), the matter-radiation equality (a_{eq}), recombination (a_*) and the matter-dark energy equality era (a_{DE}). (**b**) Close-up of the BDE equation of state at late times. The narrow grey band marks the 95% C.L. obtained from the Markov chains. (**c**) Evolution of the energy density of matter (dash-dotted black), standard radiation (dotted orange), dark energy as BDE (solid blue) and dark energy as a cosmological constant (dashed red). (**d**) Close-up of the energy density of matter and dark energy at late times.

with respect to the ΛCDM paradigm. Both figure (1.1) and the dashed red line of figure (5.6**c**) clearly expose the fine-tuning and the coincidence problems present in ΛCDM. Moreover, the slight dilution of $\rho_{\rm BDE}$ at late times leads to a universe with less dark energy content today $\rho_{\rm DE0} \propto \Omega_{\rm DE0} h^2$ than ΛCDM of about 3.7% as may be deduced from the results of table (5.1). On the contrary, the matter content $\rho_{m0} \propto \Omega_m h^2$ at present is almost the same in both models with a tiny excess of 0.5% in ΛCDM. Consequently,

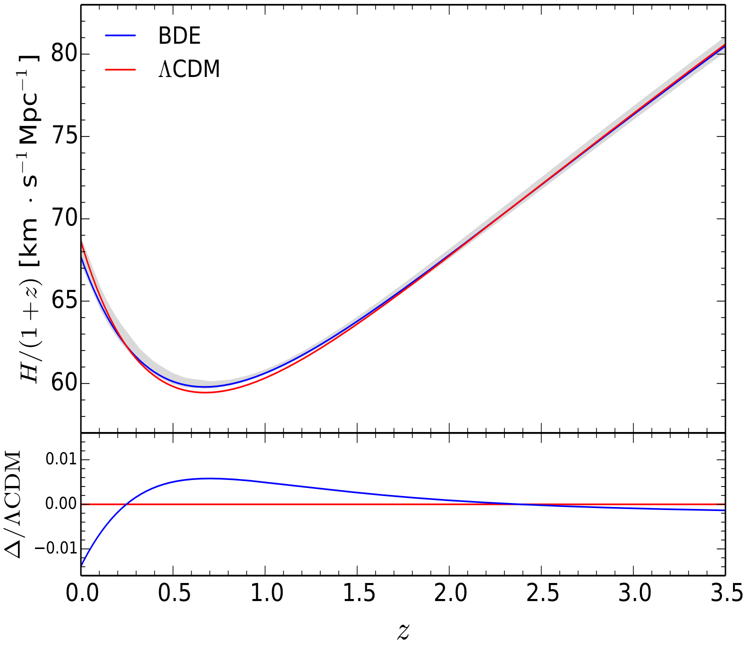

Figure 5.7: Conformal expansion rate for the best fit BDE (blue) and ΛCDM (red) models. The grey band marks the 95% C.L. for the BDE model obtained from the Markov chains. The bottom panel shows the fractional difference with respect to ΛCDM.

the current expansion rate is slower in BDE by 1.39% as seen in figure (5.7). However, $\rho_{\rm BDE}$ grows faster than ρ_Λ as we go to the past because of the slight dilution of BDE due to the late-time departure of the equation of state from -1. $\rho_{\rm BDE}$ becomes larger than ρ_Λ at $z \gtrsim 0.25$ (c.f. figure (5.6**d**)) leading to a higher expansion rate between $0.25 \lesssim z \lesssim 2.4$ with a maximum deviation from ΛCDM of 0.6% around $z \approx 0.7$. For higher redshifts in the matter domination era the difference in the dark energy content becomes irrelevant and it is the tiny difference of 0.5% in ρ_{m0} what makes the expansion rate slower in BDE once again. Note the difference with respect to the case where both models have the same content of matter and dark energy today and therefore have the same expansion rate at present as shown in figure (4.1). In that case $\rho_{\rm BDE}(a) > \rho_\Lambda(a)$ for all a, which yields $H_{\rm BDE}(a) > H_{\Lambda{\rm CDM}}(a)$ leading to a smaller angular diameter distance $D_A(z) = (1+z)^{-1}\int_0^z dz'/H(z')$ for BDE. However, when fitting to the data, the CMB information constrains very well the angular size of the sound horizon at recombination $\theta_* = r_*/D_A(z_*)$ and since r_* and z_* are practically the same in both models, then $D_A(z_*)$ must agree too as can be seen in the best fit, mean and marginal limits in table (5.1) and the marginal distribution of $\theta_{\rm MC}$ in figure (5.3). This automatically

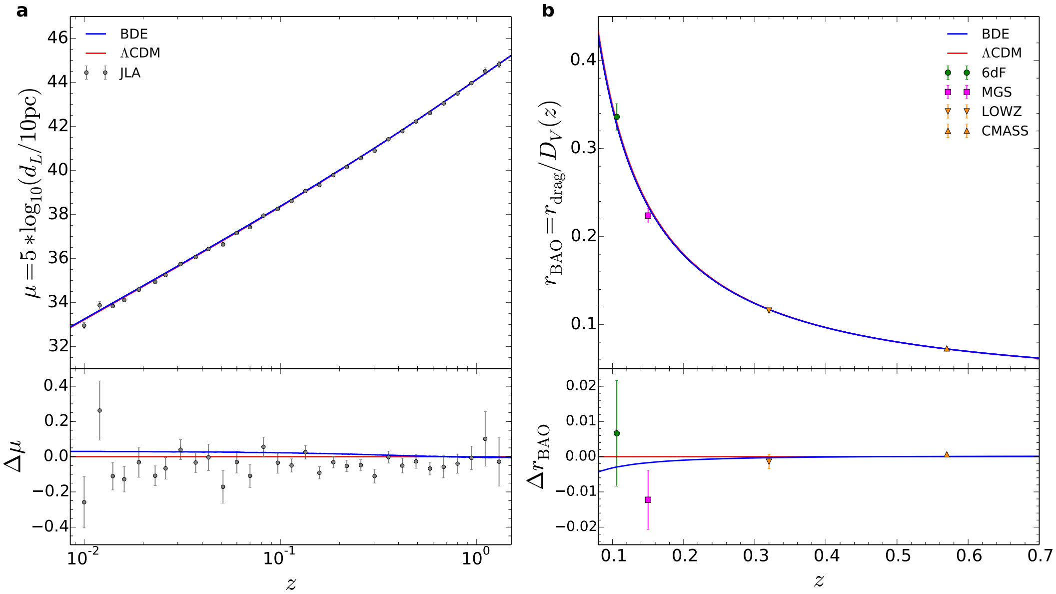

Figure 5.8: (**a**) BDE and ΛCDM fits to the modulus distance measurements of the JLA type Ia supernovae compilation. The lower panel shows the absolute residual $\mu - \mu(\Lambda\mathrm{CDM})$. (**b**) Fits to the BAO ratio measurements of the four datasets considered in our analysis. The lower panel shows the absolute residual $r_{\rm BAO} - r_{\rm BAO}(\Lambda\mathrm{CDM})$.

excludes the scenario where $H_{\rm BDE}(a) > H_{\Lambda\rm CDM}(a)$ or $H_{\rm BDE}(a) < H_{\Lambda\rm CDM}(a)$ for all a, enforcing $H_{\rm BDE}(a) < H_{\Lambda\rm CDM}(a)$ in a late-time period preceded by an earlier epoch where $H_{\rm BDE}(a) > H_{\Lambda\rm CDM}(a)$ (as shown in figure (5.7)) to make the angular diameter distance to the last scattering surface to be the same.

As we previously discussed, the size and the evolution of the expansion rate affect the cosmological distances probed by SNeIa and BAO observations. Figures (5.8**a**) and (5.8**b**) show the best fit to the distance modulus (binned in z) and BAO measurements of the datasets we consider. Since $H_{\rm BDE} < H_{\Lambda\rm CDM}$ for $z \lesssim 0.25$, $d_L(\mathrm{BDE}) > d_L(\Lambda\mathrm{CDM})$ and therefore $\mu(\mathrm{BDE}) > \mu(\Lambda\mathrm{CDM})$ in this range, which means that light sources would appear fainter in a ΛCDM cosmology in the very low-z region. Nevertheless, the difference in μ is less than 0.15% which still lies beyond the accuracy of the data. On the other hand, as we move to higher redshifts where $H_{\Lambda\rm CDM} > H_{\rm BDE}$ the integral $d_L \propto \int_0^z dz'/H(z')$ over the whole range of z is the same compensating the initial difference and leading to $\mu(\mathrm{BDE}) \approx \mu(\Lambda\mathrm{CDM})$ as shown in the plot. In the same way, $D_V \propto (D_A^2/H)^{1/3} \sim 1/H$ for $z \ll 1$, leading to $D_V(\Lambda\mathrm{CDM}) < D_V(\mathrm{BDE})$ and since $r_{\rm drag}$ is practically the same (c.f. table (5.1)), we have $r_{\rm BAO}(\mathrm{BDE}) < r_{\rm BAO}(\Lambda\mathrm{CDM})$ as can be seen. However, the difference in the BAO ratio is larger (up to 0.4%) because $r_{\rm BAO}$ is an algebraic function of the distance, unlike μ where the dependence is logarithmic.

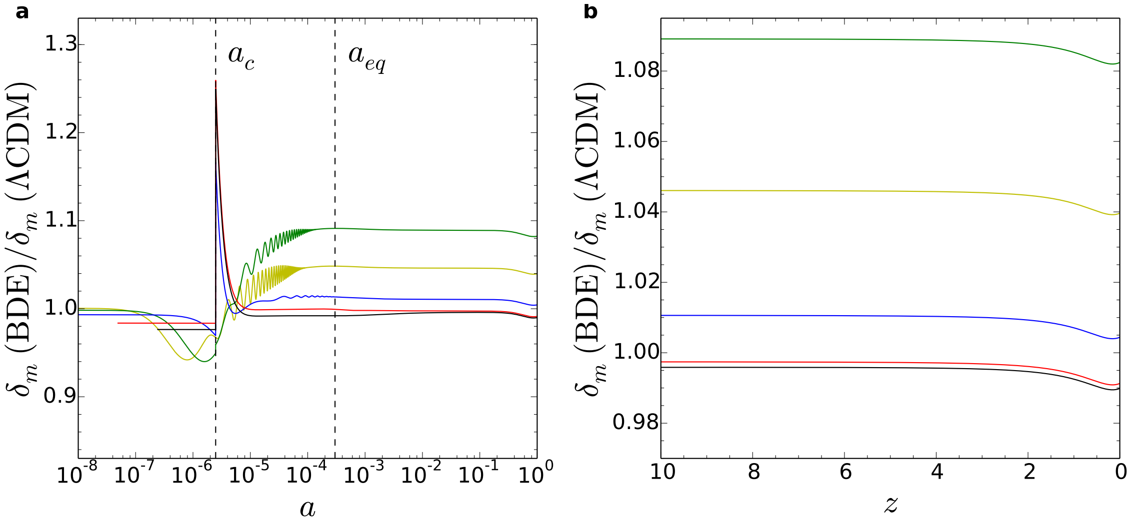

Figure 5.9: (**a**) Quotient of matter perturbations in the newtonian gauge for the best fit BDE and ΛCDM models for $k = 10\text{Mpc}^{-1}$ (yellow), 5Mpc^{-1} (green), 1Mpc^{-1} (blue), 0.05Mpc^{-1} (red), and 0.005Mpc^{-1} (black). The vertical dotted lines mark the condensation epoch a_c and the matter-radiation equality era a_{eq}, respectively. (**b**) Close-up of the ratio of matter perturbations at late times for the modes shown in the left panel.

5.3 Matter perturbations

5.3.1 The matter power spectrum

Figures (5.9**a**) and (5.9**b**) show the ratio $\delta_m(\text{BDE})/\delta_m(\Lambda\text{CDM})$ of matter perturbations (baryons + cold dark matter) in the newtonian gauge for the best fit models. For the sake of comparison, we plot the same modes as in figures (4.4**a**) and (4.4**b**), where both models run with the same set of parameters. Comparing with those results, we first note that when the modes are outside the horizon, the initial suppression in BDE due to the extra relativistic degrees of freedom of the dark group is not the same for all the modes, which is a direct consequence of the different initial amplitude given by n_s and A_s in equation (1.113). The effects of the further suppression due to the difference in the horizon crossing time, the enhancement of matter perturbations because of the rapid dilution of the scalar field after a_c, and the late-time suppression due to the BDE dark energy dynamics are still present, but some differences arise between a_c and a_{eq}. When fitting to the data, the enhancement between a_c and a_{eq} is more prominent for small modes $k > k_c = 0.925\text{Mpc}^{-1}$ (yellow, green and blue curves) crossing the horizon before a_c, while in this period there is no noticeable difference for modes entering the horizon near a_c (red curve) and the enhancement is less prominent for large modes

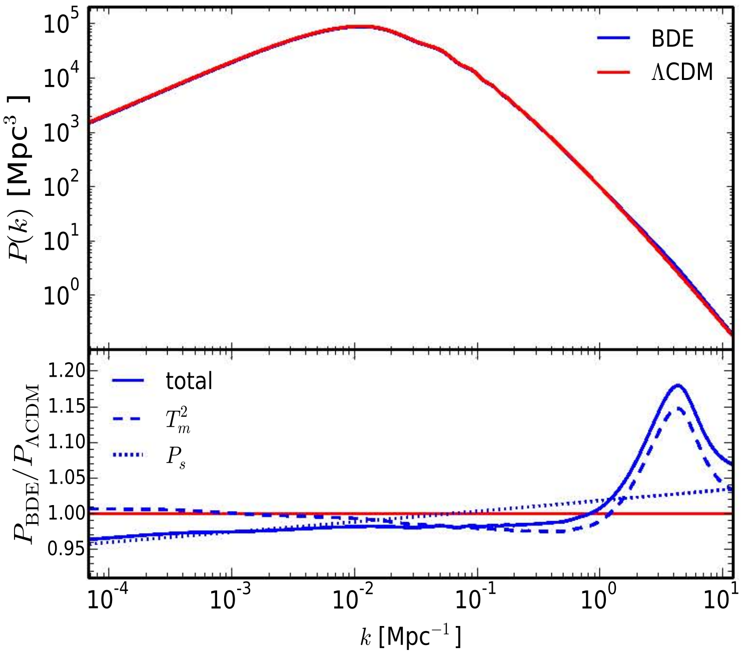

Figure 5.10: Matter power spectrum at $z = 0$ for the best fit BDE (blue) and ΛCDM (red) models. The bottom panel shows the ratio of the total matter spectrum $P_{\rm BDE}/P_{\Lambda\rm CDM}$ (solid) and the contributions from the primordial spectrum $P_s(\rm BDE)/P_s(\Lambda CDM)$ (dotted) and the matter transfer function at present time $T_m^2(\rm BDE)/T_m^2(\Lambda CDM)|_{z=0}$ (dashed).

(black curve). However, before reaching the full dominance of matter around $a \sim 10^{-3}$ (where matter perturbations scale as $\delta_m \propto a$ in both models leading to a constant ratio $\delta_m(\rm BDE)/\delta_m(\Lambda CDM)$) there is a slight suppression affecting all the modes that already entered the horizon. The late-time suppression effect is also less prominent and now the ratio $\delta_m(\rm BDE)/\delta_m(\Lambda CDM)$ drops only 0.62% with respect to the constant value during matter domination. Figure (5.10) shows the resulting power spectra for the best fit. Since the models now run with different parameters, the final shape of the quotient $P_{\rm BDE}/P_{\Lambda\rm CDM}$ shown in the bottom panel is a combination of the present value of $T_m^2(\rm BDE)/T_m^2(\Lambda CDM)$ determined by the growth of matter perturbations, and the ratio $P_s(\rm BDE)/P_s(\Lambda CDM)$ of the primordial spectra determined by the difference in n_s and A_s:

$$\frac{P_{\rm BDE}}{P_{\Lambda\rm CDM}} = \frac{P_s(\rm BDE)}{P_s(\Lambda CDM)} \cdot \frac{T_m^2(\rm BDE)}{T_m^2(\Lambda CDM)}, \tag{5.7}$$

where we have used equations (1.110) and (1.111). We can see where is dominant each term. At large scales $k \lesssim 5 \times 10^{-3}\text{Mpc}^{-1}$ the difference between BDE and ΛCDM are due to the distinct primordial spectrum, while the the matter transfer function is nearly the same. On the other hand, the differences at small scales $k \gtrsim 6 \times 10^{-2}\text{Mpc}^{-1}$ comes mostly from the matter growth. Once again, the peak at $k \approx 4.3\text{Mpc}^{-1}$ lies in the non-linear regime so it will be interesting to see how much of this signature remains when the complex non-linear effects are take into account [90].

5.3.2 Parameters

Let's now see the imprints of this dynamics on the parameters that characterise structure formation. Figure (5.11) shows the root mean square matter fluctuations in a sphere of radius $R = 8h^{-1}$ Mpc. This parameter is defined for a general radius R as:

$$\sigma_R^2(z) \equiv \langle \delta_R^2(\bar{x}, z) \rangle = \frac{1}{V} \int d^3x \; \delta_R^2(\bar{x}, z), \tag{5.8}$$

where the brackets denote the average over all space (with volume V) and δ_R is the matter density contrast convolved with a window function $W_R(\bar{x} - \bar{x}')$ given by:

$$\delta_R(\bar{x}, z) \equiv \int d^3x' \; \delta_m(\bar{x}, z) W_R(\bar{x} - \bar{x}') \tag{5.9}$$

We can express σ_R^2 in terms of the matter power spectrum $P(k)$ using the definition of the correlation function $\xi(r)$ and the relation between $\xi(r)$ and $P(k)$ as stated in equations (1.115) and (1.114):

$$\begin{aligned}
\sigma_R^2(z) &= \frac{1}{V} \int d^3x d^3y' d^3y'' \; \delta_m(\bar{x} - \bar{y}', z) \delta_m(\bar{x} - \bar{y}'', z) W_R(\bar{y}') W_R(\bar{y}'') \\
&= \int d^3y' d^3y'' \; \xi(\bar{y}' - \bar{y}'', z) W_R(\bar{y}') W_R(\bar{y}'') \\
&= \frac{1}{(2\pi)^3} \int d^3k d^3y' d^3y'' \; P(k, z) e^{i\bar{k}\cdot(\bar{y}' - \bar{y}'')} W_R(\bar{y}') W_R(\bar{y}'') \\
&= \frac{1}{(2\pi)^3} \int d^3k \; P(k, z) \int d^3y' \; W_R(\bar{y}') e^{i\bar{k}\cdot\bar{y}'} \int \; d^3y'' W_R(\bar{y}'') e^{-i\bar{k}\cdot\bar{y}''}
\end{aligned} \tag{5.10}$$

Since W_R is real, $W_R(\bar{y}) = W_R^*(\bar{y})$ so:

$$\sigma_R^2(z) = \frac{1}{(2\pi)^3} \int d^3k \; P(k, z) |W_R(\bar{k})|^2 = \frac{1}{2\pi^2} \int_0^\infty dlnk \; k^3 P(k, z) |W_R(\bar{k})|^2 \tag{5.11}$$

Normally one considers[2] the top-hat spherical window function defined as:

$$W_R(\bar{x} - \bar{x}') = \begin{cases} 1 & \text{if } |\bar{x} - \bar{x}'| \leqslant R \\ 0 & \text{if } |\bar{x} - \bar{x}'| > R, \end{cases} \tag{5.12}$$

---

[2] This is the case in `CAMB`.

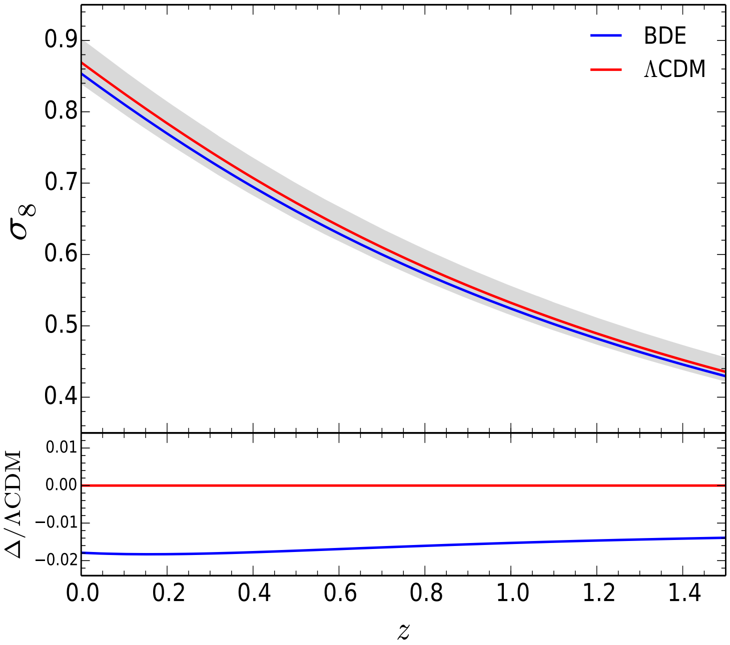

Figure 5.11: Evolution of the root mean square of matter fluctuations at late times in a sphere of radius $R = 8h^{-1}$ Mpc for the best fit BDE (blue) and ΛCDM (red) models. The grey band marks the 95% C.L. for the BDE model obtained from the Markov chains. The bottom panel shows the relative difference with respect to ΛCDM.

whose Fourier transform is simply given by:

$$W_R(\bar{k}) = \frac{3}{(Rk)^3}[\sin(Rk) - Rk\cos(Rk)], \tag{5.13}$$

where $k = |\bar{k}|$. Although the constraints on σ_8 for BDE and ΛCDM are consistent within the 95% C.L. as shown in the grey band in the plot, we see that for the best fit models $\sigma_8(\text{BDE}) < \sigma_8(\Lambda\text{CDM})$, where the relative difference slightly varies from 1.8% at $z = 0$ to 1.4% at $z = 1.5$. At first sight this result seems to contradict what we found in figure (5.10) where the matter power spectrum of BDE at $z = 0$ is significantly enhanced for $k \gtrsim 0.7$ Mpc^{-1}. However, the dominant contribution to the integral in equation (5.11) comes from the modes in the range 10^{-3} Mpc$^{-1} \leqslant k \leqslant 10^{-1}$ Mpc^{-1}; for smaller modes $k^3P(k)$ is suppressed by the cubic power of k, while for larger modes $k^3P(k)$ is suppressed by the window function (5.13). In figure (5.10) $P_{\text{BDE}}(k) < P_{\Lambda\text{CDM}}(k)$ and $|W_R(\bar{k})|^2 \simeq const$ in this range, which implies that $\sigma_8(\text{BDE}) < \sigma_8(\Lambda\text{CDM})$. However, the difference still lies below the precision limits of the measurements: $\sigma_8 = 0.83 \pm 0.1$ [106], $\sigma_8 = 0.91^{+0.22}_{-018}$ [107], $\sigma_8 = 0.81 \pm 0.26$ [108].

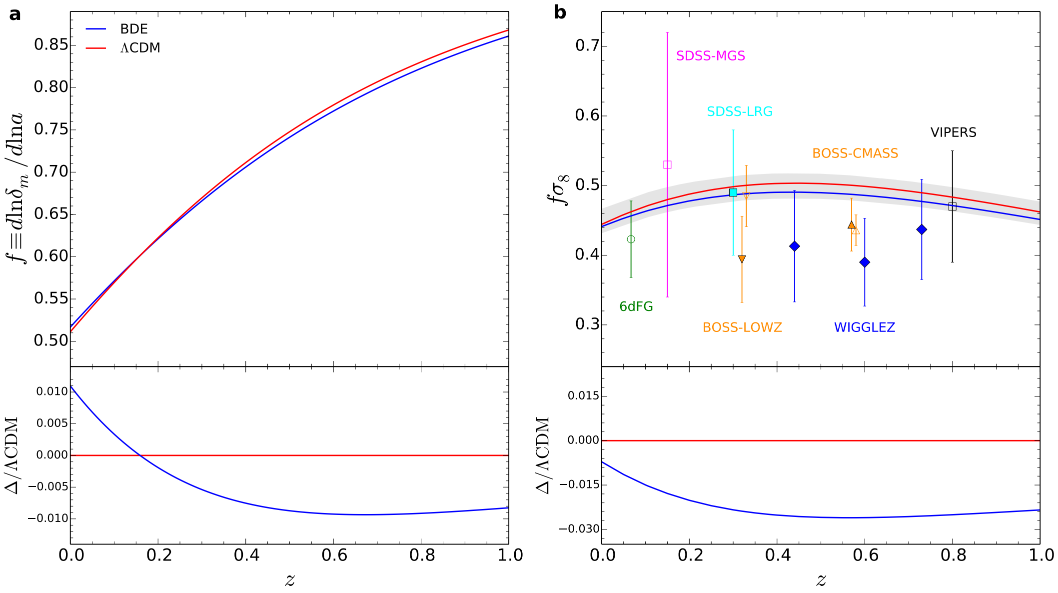

Figure 5.12: (**a**) Evolution of the growth function at late times for the best fit BDE (blue) and ΛCDM (red) models. The bottom panel shows the relative difference with respect to ΛCDM. (**b**) Predictions on $f\sigma_8$ for the best fit BDE (blue) and ΛCDM (red) models. We append the observational points measured by the 6dFG survey [109], SDSS-MGS [110] and SDSS-LRG [111], BOSS-LOWZ and BOSS-CMASS [112], WIGGLEZ [113], and the VIPERS survey [114]. The empty markers correspond to measurements where the Alcock-Paczynski effect was neglected. The grey band marks the 95% C.L. for the BDE model obtained from the Markov chains. The bottom panel shows the relative difference with respect to ΛCDM.

Figure (5.12**a**) shows the growth function f defined as:

$$f \equiv \frac{d\ln\delta_m}{d\ln a} = \frac{1}{H}\frac{\dot{\delta}_m}{\delta_m} \tag{5.14}$$

at late times. From the analysis of section (1.2.3) we see that $f = 1$ during the matter domination era, since $\delta_m \propto a$ for all modes within the horizon in that period. As we approach the present epoch and dark energy becomes dominant exerting a negative pressure, matter growth slows down and therefore f departs from 1 towards smaller values. For the best fit $f(\mathrm{BDE}) > f(\Lambda\mathrm{CDM})$ in $z \lesssim 0.16$ and then $f(\mathrm{BDE}) < f(\Lambda\mathrm{CDM})$ for larger z. However, in both cases the relative difference does not exceed the 1%. The compelling reason to determine f is the possibility of studying the clustering of matter (including unseen components such as the CDM) through the relation between the peculiar velocity field $\bar{u}$ of visible galaxies with the total matter density contrast δ_m

[12]:

$$\nabla \cdot \bar{u} = -Hf\delta_m \tag{5.15}$$

Measurements of redshift space distortions (RSD) in galaxy redshift maps actually constrain the combination $f\sigma_8$. Figure (5.12**b**) shows the predictions for the best fit models together with the observational points of some surveys [109–114]. From figure (5.11) we see that the difference $\sigma_8(\mathrm{BDE}) < \sigma_8(\Lambda\mathrm{CDM})$ is large enough to compensate the difference $f(\mathrm{BDE}) > f(\Lambda\mathrm{CDM})$ in $f\sigma_8$ for $z \lesssim 0.16$; for larger redshifts both f and σ_8 are smaller in BDE and therefore $f(\mathrm{BDE}) < f(\Lambda\mathrm{CDM})$. However, although the discrepancies are about 2.6% in $0.4 \leqslant z \leqslant 1$ the predictions of ΛCDM still lie within the 95% C.L. of BDE. Moreover, the observational techniques still need to be improved taking into account important sources of error such as the modelling of nonlinearities and the subtraction of the Alcock-Paczynski effect [26] which might bias the results as shown by the empty and filled triangles of the BOSS-LOWZ and BOSS-CMASS surveys in the plot.

Matter growth history is compactly parameterised by the growth index γ defined by the expression [115]:

$$f = \Omega_m^\gamma(a) \qquad \Rightarrow \qquad \gamma \equiv \frac{\ln f}{\ln \Omega_m(a)} \tag{5.16}$$

This parameter proves to be very useful not only in analyses of dark energy models but also in studies of modified gravity theories, where its value, its time behaviour and scale dependence might be quite different than $\gamma(\Lambda\mathrm{CDM}) \simeq 0.55$ in ΛCDM [116]. Strictly speaking $\gamma(\Lambda\mathrm{CDM})$ is not constant but varies in time. However, the time dependence is very mild so it can be assumed constant to high accuracy. Moreover, it has been found [117] that $\gamma \simeq const$ is also a good approximation for a variety of dynamical dark energy models, although if we consider strong clustering of the dark energy component γ may vary considerably in time so this approximation is no longer accurate [118]. Here we present the full evolution of the growth index at late times. Figure (5.13) shows the predicted bounds on γ derived from our fits for the BDE and ΛCDM models. We find $\gamma(\mathrm{BDE}) > \gamma(\Lambda\mathrm{CDM})$ at more than 2σ level. Nevertheless, the difference lies below 0.3% which is far beyond the precision of the observational bounds: $\gamma = 0.55^{+0.13}_{-0.14}$ [107], $\gamma = 0.64 \pm 0.09$ [110], $\gamma = 0.547 \pm 0.088$ [109]. Note that since the growth index evolves similarly in both models we may also assume $\gamma \simeq const$ for BDE. Using the fitting formula provided in [117]:

$$\gamma = 0.55 \pm 0.05[1 + w(z = 1)], \tag{5.17}$$

and $w_{\mathrm{BDE}}(z = 1) = -0.98$ as shown in figure (5.6**b**), we obtain $\gamma(\mathrm{BDE}) \simeq 0.551$ which is only 0.18% larger than $\gamma(\Lambda\mathrm{CDM})$.

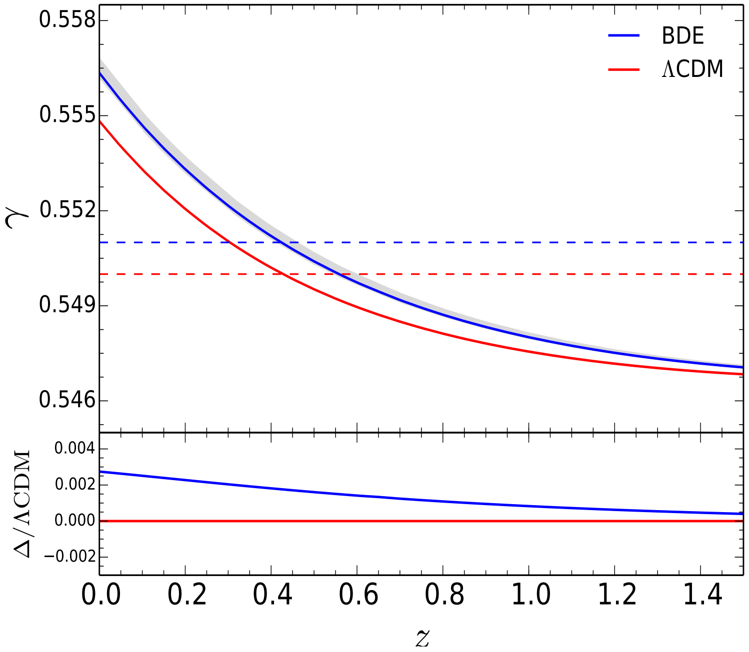

Figure 5.13: Evolution of the growth index at late times for the best fit BDE (blue solid) and ΛCDM (red solid) models. The narrow grey band marks the 95% C.L. for the BDE model obtained from the Markov chains. The dashed horizontal lines are the $\gamma \simeq const$ approximations derived from the fitting formula $\gamma = 0.55 \pm 0.05[1 + w(z = 1)]$ [117] where $w(z = 1) = -0.98$ for BDE. The bottom panel shows the relative difference with respect to ΛCDM.

5.3.3 Large Scale Structure

Unlike radiation perturbations whose amplitude remains small over the whole history of the universe, matter fluctuations do grow and eventually they become so large that first order perturbation theory ceases to be a good approximation. At this point new physical phenomena come into play and we need to implement other analytical/numerical techniques to study matter structure growth. However, we can still use our results to explore the intermediate regime between the linear theory and the full nonlinear dynamics only accessible through N-body simulations.

The spherical collapse model [12, 28] provides a simplified but a powerful picture that captures the essentials of the processes leading to the formation of nonlinear structures. The idea is to consider a spherical overdense region embedded in a flat FLRW background. Whereas the evolution of the background proceeds as we saw in chapter 1 —for the ΛCDM model— the overdense region behaves like a closed universe with a

FLRW metric with positive curvature [28]. Initially both the overdense region and the background universe expand at the same rate. However, since the matter density within the sphere is larger than the critical density, the expansion of the sphere slows eventually halting and decoupling completely from the background, and then it collapses. The contraction of the sphere does not proceed indefinitely until reaching the unphysical state of a singularity, but it stops before when a mechanism known as violent relaxation virializes the system making the kinetic energy of the cold dark matter particles within the sphere equal to half the gravitational potential energy. The virialization time is almost the same that the collapse time [12], which in turn is twice the turnaround epoch defined by the beginning of the contraction when the sphere reaches its maximum radius. As a result of these processes, the final radius of the sphere will be half the radius at the turnaround and the linear theory extrapolation of the matter overdensity at the time of collapse in ΛCDM is $\delta_{coll} \approx 1.686$. Although this value depends both on the model and the values of the cosmological parameters [119], the dependence is mild [120] so for comparison purposes it can be used also in BDE.

We can estimate the abundance of collapsed objects using the Press-Schechter theory [121]. The main idea of the model is to describe the matter overdensity field in real space by a smooth gaussian field whose variance on a sphere of radius R is given by equation (5.11). Note that here we are considering the linear power spectrum given by the solution of the perturbed equations. If we now smooth the matter fluctuations δ_R on the sphere as prescribed in equation (5.9), the probability that at some time δ_R exceeds the linear overdensity at collapse δ_{coll} is [12]:

$$P_{>\delta_{coll}}(M,z) = \frac{1}{\sqrt{2\pi}\sigma_R(z)} \int_{\delta_{coll}}^{\infty} exp\left(-\frac{\delta_R^2}{2\sigma_R^2(z)}\right) d\delta_R, \tag{5.18}$$

where $M = \frac{4}{3}\pi R^3 \bar{\rho}_m$ is the mean mass enclosed within the sphere. Then, the number of collapsed objects per unit volume with mass between M and $M + dM$ is given by [12]:

$$dn = -\sqrt{\frac{2}{\pi}} \frac{d\sigma_R}{dM} \cdot \left(\frac{\bar{\rho}_m \delta_{coll}}{M\sigma_R^2}\right) exp\left(-\frac{\delta_{coll}^2}{2\sigma_R^2}\right) dM \tag{5.19}$$

Figure (5.14) shows the differential mass function $dn/dlnM$ for the best fit BDE and ΛCDM models at $z = 0$. Since $M \propto R^3$ and $R = \pi/k$, then the mass of the object is inversely proportional to the wavenumber, which means that large masses correspond to small modes (large scales) and vice versa. Moreover, since the matter content $\bar{\rho}_m$ in both models is almost the same (c.f. section (5.2)), when we compare the differential mass function at a particular mass scale we are also comparing that function practically at the same mode. We observe an opposite behaviour for large and small scales. The number of structures with $M \gtrsim 10^{14} M_\odot$ corresponding to $k \lesssim 0.4\text{Mpc}^{-1}$ is clearly suppressed in BDE, while there is a slight excess of collapsed objects in the range $9 \times 10^9 M_\odot \lesssim M \lesssim 1 \times 10^{14} M_\odot$ where $8\text{Mpc}^{-1} \gtrsim k \gtrsim 0.4\text{Mpc}^{-1}$ peaking at

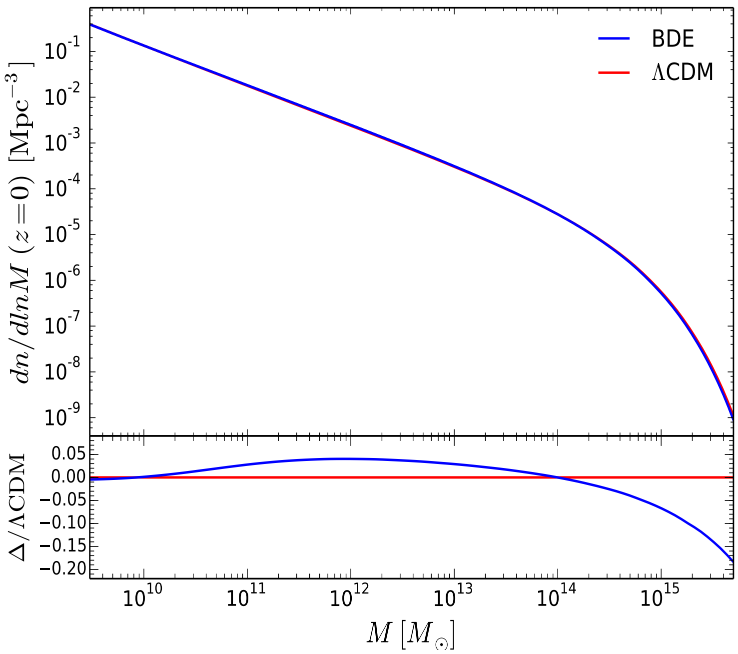

Figure 5.14: Differential mass function at $z = 0$ for the best fit BDE (blue) and ΛCDM models using the Press-Schechter formula [121]. The bottom panel shows the relative difference with respect to ΛCDM. The mass M is expressed in units of solar masses $M_\odot = 1.9885 \times 10^{30}$ kg [122].

$M \approx 1.5 \times 10^{12} M_\odot$. Since the age of the universe is almost the same in both models (c.f. table (5.1)), these results mean that large structures take more time to form in BDE, while small objects form more quickly. Therefore, we expect to observe less massive galaxy clusters (with $N_g \gtrsim 100$ galaxies) and more light structures (isolated galaxies and poorly populated clusters) in a BDE universe. Of course, the numbers we found cannot be taken too seriously given the intrinsic limitations of the Press-Schechter approach [12], but it will be interesting to see if this tendency still keeps in N-body simulations [90].

5.4 BBN consistency

The marginal limits of the abundances of primordial helium and deuterium listed in the last two rows of table (5.1) show a marked discrepancy between our BDE model and ΛCDM. The excess of 4.9% of helium and 12% of deuterium in the BDE model is a direct consequence of the extra relativistic degrees of freedom due to the dark group

Table 5.3: Astrophysical bounds on primordial helium-4 and deuterium abundances.

Helium ($Y_{\rm P}^{\rm BBN}$)	Deuterium ($10^5 D/H$)
0.2574 ± 0.0036 [124]	2.87 ± 0.22 [125]
0.2535 ± 0.0036 [126]	2.53 ± 0.04 [127]
0.2551 ± 0.0022 [128]	2.45 ± 0.28 [129]

present during the BBN epoch, as we have already expected from the discussion of section (4.2). These marginal limits are obtained from theoretical predictions based on the standard BBN theoretical framework, which takes as input the physical baryon density $\Omega_b h^2$ (varied in the Markov chains) and the number of extra relativistic degrees of freedom N_{ext} if present ($N_{ext} = 0.945$ held fixed for $a < a_c$ in our BDE model as stated in equation (3.25)). It is therefore interesting to compare these theoretical predictions derived from our fits with the astrophysical data available at present. Before doing this, it is important to bear in mind that although signficant progress has been made in the last two decades [87], the uncertainties in the theoretical calculations and the precision of the observational evidence still lie beyond the required accuracy to make primordial light element abundances a precise cosmological probe useful to make conclusive model selection.

On the theoretical side, the uncertainties in the BBN predictions are mainly affected by the experimental errors in the cross sections of the nuclear reactions involved in the production of light nuclei as well as by the neutron mean lifetime τ_n [87], which is not well determined at present, showing a discrepancy between $\tau = 880.3 \pm 1.1\ s$ [88] obtained from experiments using ultracold neutrons in traps and $\tau = 887.7 \pm 2.3\ s$ [123] measured in decays in flight beams. The situation is not better on the observational side where the limited amount of data and the systematics don't allow to set tight constraints below the percent level. For example, the helium abundance is determined from measurements of emission lines in extragalatic HII regions, but the number of such regions where the theoretical models of the emission flux fit well the observations so that a reliable estimation of the abundance can be extracted does not exceed 30 [87]. On the other hand, although all observed deuterium is of primordial origin since there are not known astrophysical phenomena that produce it, there is also evidence of deuterium depletion in the interestellar and galactic medium, which affects the accurate estimation of its primordial fraction [87]. All these difficulties are reflected in the dispersion of recent observational constraints quoted in table (5.3). We see that the theoretical predictions for the BDE model agree with most of these bounds, while ΛCDM falls short of helium production. However, if the helium fraction is determined from a linear extrapolation to zero metallicity in the $Y_{\rm P}^{\rm BBN} - O/H$ diagram instead from the weighted mean of the data, the value obtained in [126] is $Y_{\mathrm{P}}^{\mathrm{BBN}} = 0.2465 \pm 0.0097$, which is consistent with the ΛCDM prediction. Therefore, BBN constraints depend not only on the data, but also on the estimation method used. Given the state of the art, the excess of helium and deuterium in the BDE model is only a preliminary result that needs to be confirmed by different estimation methods and much more precise measurements coming in the following years.

5.5 The CMB power spectrum

Figure (5.15) shows the fit of the BDE (in blue) and ΛCDM (in red) models to the Planck 2015 measurements of the temperature anisotropies of the CMB. The results in table (5.2) show a slight preference for BDE in the low multipole region as opposed to the better performance of ΛCDM at high resolution data. However, these two effects cancel each other and the overall fit of both models is practically equivalent (see bottom of table (5.1)). It is important to stress that unlike standard extensions of the ΛCDM model [25, 26] where the extra relativistic degrees of freedom N_{ext} are present over the whole history of the universe, in BDE this extra amount of radiation vanishes once the scalar field forms long before recombination, so its influence on the CMB is only indirectly given by the enhanced amount of helium. Therefore, the stringent constraints on N_{ext} such as $N_{ext} = 0.104 \pm 0.23$ [26] found in these studies using CMB information don't apply here, since the BDE model describes a completely different cosmological scenario than usual constant N_{ext}.

The most prominent deviations from ΛCDM lie in the range $2 \leqslant l \leqslant 30$ where the discrepancies are up to the 1.7%. Unfortunately this is the region where the cosmic variance sets unavoidable limitations in reducing the error bars of the measurements. Nevertheless it is impressive to see the progress made in the precision of the data since the launch of the COBE satellite in 1989 [24, 130–132]. It is interesting to compare this plot with figure (4.6) where both models run with the same set of parameters. We note that the position of the peaks now coincide and therefore the oscillations of the residuals ΔD_l^{TT} gone. This can be immediately inferred from equation (4.27) where the shift of the peaks now vanishes given the similarity of the values of $r_s(z_*)$, z_* and $D_A(z_*)$ in table (5.1). On the other hand, the extra damping of the spectrum at high multipoles due to the enhanced production of helium in BDE also vanishes. In this case the damping wavenumber k_D is still smaller in BDE so $e^{-(1/k_D^2)}(\mathrm{BDE}) < e^{-(1/k_D^2)}(\Lambda\mathrm{CDM})$, but this effect is compensated by a larger optical depth τ with $e^{-\tau}(\Lambda\mathrm{CDM}) < e^{-\tau}(\mathrm{BDE})$ leaving the total damping factor of equation (4.28) approximately unchanged. Finally, the enhanced power of BDE at low multipoles now turns into a suppression. This suppression is a direct consequence of the different tilt n_s and amplitude A_s used in each model. To see this, the green curve shows the CMB power spectrum for the BDE model with n_s and A_s set equal to ΛCDM but the rest of the parameters kept to their

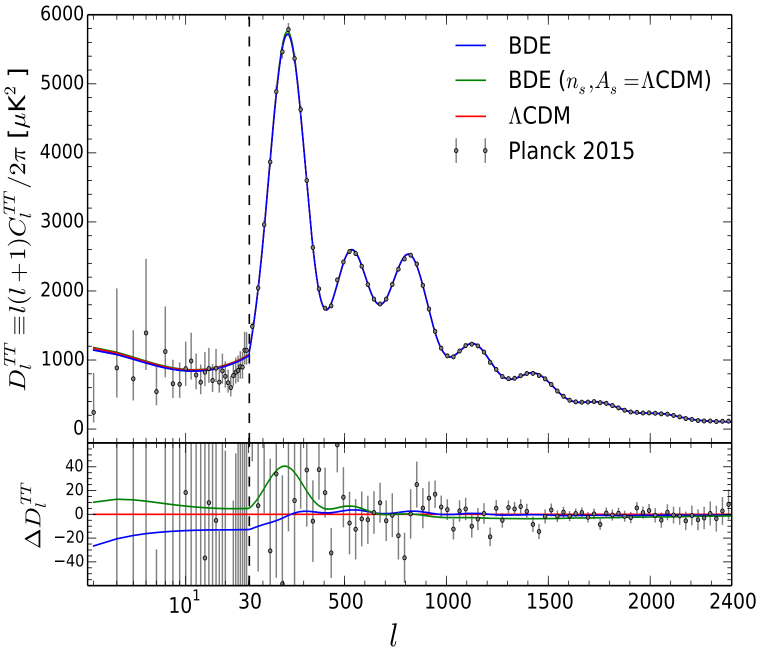

Figure 5.15: Fit of the BDE (blue) and ΛCDM (red) models to the Planck 2015 measurements of the temperature anisotropy spectrum of the CMB (grey circles). The green curve shows the spectrum for a BDE model with n_s and A_s set equal to the best fit ΛCDM values while the rest of the basic parameters kept to the BDE best fit. We use a logarithmic scale for multipoles between $2 \leqslant l \leqslant 30$ and then a linear scale for higher multipoles (vertical dashed line). The bottom panel shows the residuals with respect to ΛCDM.

best fit values. We recover the enhanced power at low multipoles and we get also an extra bump around the first peak $l \approx 220$. From $l \gtrsim 900$ onwards there is a very slight suppression of the green spectrum that can be neglected, so we conclude that the influence of n_s and A_s on the fit of BDE manifests at low multipoles extending up to the location of the first peak. As happened when we analysed the results of the matter power spectrum, we have identified where the effects of the primordial spectrum parameters n_s and A_s set predominantly the difference with respect to ΛCDM and where this difference arises because of the intrinsic dynamics of our model.

Conclusions

In this work we assessed the viability of the Bound Dark Energy model as a possible alternative to the cosmological constant. The BDE mechanism explains the origin of the dark energy from first principles using what seems to be the most viable extension of the Standard Model of particle physics. Unlike other implementations of quintessence and even other dark energy models, we don't introduce additional cosmological free parameters. The condensation scale Λ_c of the light meson representing dark energy, the epoch of the condensation a_c, the exponent of the potential $n = -2/3$, and the initial conditions of the scalar field are quantities determined once we set the fundamental parameters N_c and N_f of the gauge group and therefore we don't have a fine-tuning problem in the theory. In fact, we demonstrated that in principle our model has one less free parameter than ΛCDM, but since the unification scale is not well constrained given the uncertainties of the gauge couplings of the Standard Model, a precise value of Λ_c is still unknown at present time. In any case, the evolution of dark energy is not sensitive to the initial conditions and therefore we don't have a coincidence problem either.

The effects of the dynamics of the dark energy in the BDE model manifest both at the background and the perturbative level not only at late times, but also in the early universe. We explored the imprints of these effects on the cosmological distances, the abundances of primordial light nuclei produced during Big Bang Nucleosynthesis, the evolution of matter perturbations and the temperature anisotropy spectrum of the CMB. We constrained our model using recent measurements of the luminosity distance of type Ia supernovae, the BAO ratio of different galaxy surveys and data of the CMB spectrum from the Planck mission. The constraint $\Lambda_c = 44.09 \pm 0.28$ eV is consistent with our theoretical expectations $\Lambda_c^{th} = 34^{+16}_{-11}$ eV, placing the epoch of the condensation of the dark energy meson at $a_c = (2.48 \pm 0.02) \times 10^{-6}$, almost 5 $e-$folds before the matter radiation equality. BDE fits slightly better the data than ΛCDM, but it is important to note the systematic improvement for the BAO measurements. The better performance of BDE in this case is reflected in manifest tensions with ΛCDM for certain combination of parameters involving the current expansion rate H_0, the cold dark matter density $\Omega_c h^2$ and the BAO ratio r_{drag}/D_V. Undoubtedly, it will be interesting to see if these results are also observed in the next generation galaxy surveys.

Although most of the constraints on the cosmological parameters in BDE and ΛCDM are consistent at the 1σ level, we found additional discrepancies where future observations will provide the definite answers. The BDE scenario predicts an enhanced amount of primordial helium and deuterium, but the current astrophysical bounds are not precise enough to settle this issue. On the other hand, there is a clear signature of the scalar field dilution on the matter power spectrum at small scales. Although these scales correspond to the non-linear regime of the spectrum, we expect to see part of this signature when we take into account the non-linear corrections in N-body simulations.

The problem of the dark energy requires the introduction of new physics. Given the success of the general theory of relativity, the robustness of the observational evidence gathered during these years, and the intimate link between particle physics and cosmology, we think that the most natural place to look for answers is in theories beyond the Standard Model. At the present time, every attempt to explain dark energy from elementary particle physics has to rely on simplifying assumptions that at first sight might sound artificial. The BDE model is not the exception. However, the history of science has shown that the construction of a new paradigm goes from simplicity to complexity. Having this in mind, we conclude that our BDE model is a viable scenario for elucidating the nature of the dark energy.

Bibliography

1. Smoot, G. F. *et al.* Structure in the COBE differential microwave radiometer first year maps. *Astrophys. J.* **396,** L1–L5 (1992).
2. Riess, A. G. *et al.* Observational Evidence from Supernovae for an Accelerating Universe and a Cosmological Constant. *The Astronomical Journal* **116,** 1009 (1998).
3. Perlmutter, S. *et al.* Measurements of Ω and Λ from 42 High-Redshift Supernovae. *The Astrophysical Journal* **517,** 565 (1999).
4. Eisenstein, D. J. *et al.* Detection of the Baryon Acoustic Peak in the Large-Scale Correlation Function of SDSS Luminous Red Galaxies. *The Astrophysical Journal* **633,** 560 (2005).
5. Cole, S. *et al.* The 2dF Galaxy Redshift Survey: power-spectrum analysis of the final data set and cosmological implications. *Monthly Notices of the Royal Astronomical Society* **362,** 505–534 (2005).
6. Boughn, S. & Crittenden, R. A correlation between the cosmic microwave background and large-scale structure in the Universe. *Nature* **427,** 45–47 (2004).
7. Nolta, M. R. *et al.* First Year Wilkinson Microwave Anisotropy Probe Observations: Dark Energy Induced Correlation with Radio Sources. *The Astrophysical Journal* **608,** 10 (2004).
8. Fosalba, P. & Gaztañaga, E. Measurement of the gravitational potential evolution from the cross-correlation between WMAP and the APM Galaxy Survey. *Monthly Notices of the Royal Astronomical Society* **350,** L37–L41 (2004).
9. Fosalba, P., Gaztañaga, E. & Castander, F. J. Detection of the Integrated Sachs-Wolfe and Sunyaev-Zeldovich Effects from the Cosmic Microwave Background-Galaxy Correlation. *The Astrophysical Journal Letters* **597,** L89 (2003).
10. Weinberg, S. The cosmological constant problem. *Rev. Mod. Phys.* **61,** 1–23 (1 1989).
11. Martin, J. Everything you always wanted to know about the cosmological constant problem (but were afraid to ask). *Comptes Rendus Physique* **13.** Understanding the Dark Universe, 566 –665 (2012).

12. Amendola, L. & Tsujikawa, S. *Dark Energy: Theory and Observations* (Cambridge University Press, 2010).

13. Nielsen, J. T., Guffanti, A. & Sarkar, S. Marginal evidence for cosmic acceleration from Type Ia supernovae. *Sci. Rep.* **6,** 35596 (2016).

14. Dam, L. H., Heinesen, A. & Wiltshire, D. L. Apparent cosmic acceleration from Type Ia supernovae. *Monthly Notices of the Royal Astronomical Society* **472,** 835–851 (2017).

15. Tomita, K. A local void and the accelerating Universe. *Monthly Notices of the Royal Astronomical Society* **326,** 287–292 (2001).

16. Syksy Räsänen. Dark energy from back-reaction. *Journal of Cosmology and Astroparticle Physics* **2004,** 003 (2004).

17. Copeland, E. J., Sami, M. & Tsujikawa, S. Dynamics of Dark Energy. *International Journal of Modern Physics D* **15,** 1753–1935 (2006).

18. Clifton, T., Ferreira, P. G., Padilla, A. & Skordis, C. Modified gravity and cosmology. *Physics Reports* **513.** Modified Gravity and Cosmology, 1 –189 (2012).

19. Ezquiaga, J. M. & Zumalacárregui, M. Dark Energy After GW170817: Dead Ends and the Road Ahead. *Phys. Rev. Lett.* **119,** 251304 (25 2017).

20. De la Macorra, A. & Stephan-Otto, C. Natural Quintessence with Gauge Coupling Unification. *Phys. Rev. Lett.* **87,** 271301 (2001).

21. De la Macorra, A. & Stephan-Otto, C. Quintessence restrictions on negative power and condensate potentials. *Phys. Rev. D* **65,** 083520 (2002).

22. De la Macorra, A. Quintessence Unification Models from Non-Abelian Gauge Dynamics. *Journal of High Energy Physics* **2003,** 033 (2003).

23. De la Macorra, A. Realistic particle physics dark energy model. *Phys. Rev. D* **72,** 043508 (2005).

24. Hinshaw, G. *et al.* Nine-year Wilkinson Microwave Anisotropy Probe (WMAP) Observations: Cosmological Parameter Results. *The Astrophysical Journal Supplement Series* **208,** 19 (2013).

25. Planck Collaboration *et al.* Planck 2013 results. XVI. Cosmological parameters. *A&A* **571,** A16 (2014).

26. Planck Collaboration *et al.* Planck 2015 results - XIII. Cosmological parameters. *A&A* **594,** A13 (2016).

27. Weinberg, S. *Gravitation and Cosmology: Principles and Applications of the General Theory of Relativity* (Wiley, New York, NY, 1972).

28. Kolb, E. & Turner, M. *The Early Universe* (Avalon Publishing, 1994).

29. Dodelson, S. *Modern cosmology* (Academic Press, San Diego, CA, 2003).

30. Fixsen, D. J. The Temperature of the Cosmic Microwave Background. *The Astrophysical Journal* **707,** 916 (2009).

31. Betts, S. *et al. Development of a Relic Neutrino Detection Experiment at PTOLEMY: Princeton Tritium Observatory for Light, Early-Universe, Massive-Neutrino Yield* in *Proceedings, 2013 Community Summer Study on the Future of U.S. Particle Physics: Snowmass on the Mississippi (CSS2013): Minneapolis, MN, USA, July 29-August 6, 2013* (2013). arXiv: `1307.4738 [astro-ph.IM]`.

32. Hannestad, S. Neutrinos in cosmology. *New Journal of Physics* **6,** 108 (2004).

33. Weinberg, S. *Cosmology* (Oxford University Press, 2008).

34. Baumann, D. *Inflation* in *Physics of the large and the small, TASI 09, proceedings of the Theoretical Advanced Study Institute in Elementary Particle Physics, Boulder, Colorado, USA, 1-26 June 2009* (2011), 523–686. arXiv: `0907.5424 [hep-th]`.

35. Ma, C.-P. & Bertschinger, E. Cosmological perturbation theory in the synchronous and conformal Newtonian gauges. *The Astrophysical Journal* **455,** 7–25 (1995).

36. Hu, W. *Concepts in CMB anisotropy formation* in *The Universe at High-z, Large-Scale Structure and the Cosmic Microwave Background* (eds Martínez-González, E. & Sanz, J. L.) (Springer Berlin Heidelberg, Berlin, Heidelberg, 1996), 207–239.

37. Lewis, A., Challinor, A. & Lasenby, A. Efficient computation of CMB anisotropies in closed FRW models. *Astrophys. J.* **538,** 473–476 (2000).

38. Tsujikawa, S. *Introductory review of cosmic inflation* in *2nd Tah Poe School on Cosmology: Modern Cosmology Phitsanulok, Thailand, April 17-25, 2003* (2003). arXiv: `hep-ph/0304257 [hep-ph]`.

39. Kosowsky, A. The cosmic microwave background. arXiv: `astro-ph/0102402 [astro-ph]` (2001).

40. Livio, M. *The Progenitors of Type Ia Supernovae* in *Type Ia Supernovae, Theory and Cosmology* (2000). arXiv: `astro-ph/9903264`.

41. Betoule, M. *et al.* Improved cosmological constraints from a joint analysis of the SDSS-II and SNLS supernova samples. *A&A* **568,** A22 (2014).

42. Conley, A. *et al.* Supernova Constraints and Systematic Uncertainties from the First Three Years of the Supernova Legacy Survey. *The Astrophysical Journal Supplement Series* **192,** 1 (2011).

43. Kowalski, M. *et al.* Improved Cosmological Constraints from New, Old, and Combined Supernova Data Sets. *The Astrophysical Journal* **686,** 749 (2008).

44. Amanullah, R. *et al.* Spectra and Hubble Space Telescope Light Curves of Six Type Ia Supernovae at $0.511 < z < 1.12$ and the Union2 Compilation. *The Astrophysical Journal* **716,** 712 (2010).

45. Hamann, J., Hannestad, S., Lesgourgues, J., Rampf, C. & Wong, Y. Y. Cosmological parameters from large scale structure - geometric versus shape information. *Journal of Cosmology and Astroparticle Physics* **2010,** 022 (2010).

46. Eisenstein, D. J. & Hu, W. Baryonic Features in the Matter Transfer Function. *The Astrophysical Journal* **496,** 605 (1998).

47. Eisenstein, D. J., Seo, H.-J. & White, M. On the Robustness of the Acoustic Scale in the Low-Redshift Clustering of Matter. *The Astrophysical Journal* **664,** 660 (2007).

48. Bassett, B. A. & Hlozek, R. Baryon Acoustic Oscillations. arXiv: `0910.5224` (2009).

49. Sutherland, W. On measuring the absolute scale of baryon acoustic oscillations. *Monthly Notices of the Royal Astronomical Society* **426,** 1280–1290 (2012).

50. Gil-Marín, H. *et al.* The clustering of galaxies in the SDSS-III Baryon Oscillation Spectroscopic Survey: BAO measurement from the LOS-dependent power spectrum of DR12 BOSS galaxies. *Monthly Notices of the Royal Astronomical Society* **460,** 4210–4219 (2016).

51. Beutler, F. *et al.* The 6dF Galaxy Survey: baryon acoustic oscillations and the local Hubble constant. *Monthly Notices of the Royal Astronomical Society* **416,** 3017–3032 (2011).

52. Ross, A. J. *et al.* The clustering of the SDSS DR7 main Galaxy sample I. A 4per cent distance measure at z=0.15. *Monthly Notices of the Royal Astronomical Society* **449,** 835–847 (2015).

53. Blake, C. *et al.* The WiggleZ Dark Energy Survey: mapping the distance−redshift relation with baryon acoustic oscillations. *Monthly Notices of the Royal Astronomical Society* **418,** 1707–1724 (2011).

54. Hu, W. & Sugiyama, N. Anisotropies in the cosmic microwave background: An Analytic approach. *Astrophys. J.* **444,** 489–506 (1995).

55. Durrer, R. *The Cosmic Microwave Background* (Cambridge University Press, 2008).

56. Sachs, R. K. & Wolfe, A. M. Perturbations of a cosmological model and angular variations of the microwave background. *Astrophys. J.* **147,** 73–90 (1967).

57. Crittenden, R. G. & Turok, N. Looking for a Cosmological Constant with the Rees-Sciama Effect. *Phys. Rev. Lett.* **76,** 575–578 (1996).

58. Wanajo, S., Itoh, N., Ishimaru, Y., Nozawa, S. & Beers, T. C. The r-Process in the Neutrino Winds of Core-Collapse Supernovae and U-Th Cosmochronology. *The Astrophysical Journal* **577,** 853 (2002).

59. Cowan, J. J. *et al.* The Chemical Composition and Age of the Metal-poor Halo Star BD +173248. *The Astrophysical Journal* **572,** 861 (2002).

60. Ivans, I. I. *et al.* Near-Ultraviolet Observations of HD 221170: New Insights into the Nature of r-Process-rich Stars. *The Astrophysical Journal* **645,** 613 (2006).

61. Carretta, E., Gratton, R. G., Clementini, G. & Pecci, F. F. Distances, Ages, and Epoch of Formation of Globular Clusters. *The Astrophysical Journal* **533,** 215 (2000).

62. Hansen, B. M. S. *et al.* The White Dwarf Cooling Sequence of the Globular Cluster Messier 4. *The Astrophysical Journal Letters* **574,** L155 (2002).

63. Riess, A. G. *et al.* A 2.4% Determination of the Local Value of the Hubble Constant. *The Astrophysical Journal* **826,** 56 (2016).

64. Efstathiou, G. H0 revisited. *Monthly Notices of the Royal Astronomical Society* **440,** 1138 (2014).

65. Bamba, K., Capozziello, S., Nojiri, S. & Odintsov, S. D. Dark energy cosmology: the equivalent description via different theoretical models and cosmography tests. *Astrophys. Space Sci.* **342,** 155–228 (2012).

66. Peebles, P. J. E. & Ratra, B. Cosmology with a Time Variable Cosmological Constant. *Astrophys. J.* **325,** L17 (1988).

67. Ratra, B. & Peebles, P. J. E. Cosmological Consequences of a Rolling Homogeneous Scalar Field. *Phys. Rev.* **D37,** 3406 (1988).

68. Wetterich, C. Cosmology and the fate of dilatation symmetry. *Nuclear Physics B* **302,** 668 –696 (1988).

69. Caldwell, R. R., Dave, R. & Steinhardt, P. J. Cosmological Imprint of an Energy Component with General Equation of State. *Phys. Rev. Lett.* **80,** 1582–1585 (1998).

70. Steinhardt, P. J., Wang, L. & Zlatev, I. Cosmological tracking solutions. *Phys. Rev. D* **59,** 123504 (1999).

71. Ma, C.-P., Caldwell, R. R., Bode, P. & Wang, L. The Mass Power Spectrum in Quintessence Cosmological Models. *The Astrophysical Journal Letters* **521,** L1 (1999).

72. Brax, P., Martin, J. & Riazuelo, A. Exhaustive study of cosmic microwave background anisotropies in quintessential scenarios. *Phys. Rev. D* **62,** 103505 (2000).

73. Weller, J. & Lewis, A. M. Large-scale cosmic microwave background anisotropies and dark energy. *Monthly Notices of the Royal Astronomical Society* **346,** 987–993 (2003).

74. Bean, R. & Doré, O. Probing dark energy perturbations: The dark energy equation of state and speed of sound as measured by WMAP. *Phys. Rev. D* **69,** 083503 (2004).

75. De la Macorra, A. & Piccinelli, G. Cosmological evolution of general scalar fields and quintessence. *Phys. Rev. D* **61,** 123503 (2000).

76. Chen, Y., Geng, C.-Q., Cao, S., Huang, Y.-M. & Zhu, Z.-H. Constraints on a ϕCDM model from strong gravitational lensing and updated Hubble parameter measurements. *JCAP* **2015,** 010 (2015).

77. Wang, P.-Y., Chen, C.-W. & Chen, P. Confronting tracker field quintessence with data. *Journal of Cosmology and Astroparticle Physics* **2012,** 016 (2012).

78. Smer-Barreto, V. & Liddle, A. R. Planck satellite constraints on pseudo-Nambu-Goldstone boson quintessence. *JCAP* **2017,** 023 (2017).

79. Alimi, J.-M. *et al.* Imprints of dark energy on cosmic structure formation I. Realistic quintessence models and the non-linear matter power spectrum. *Monthly Notices of the Royal Astronomical Society* **401,** 775–790 (2010).

80. Linder, E. V. The dynamics of quintessence, the quintessence of dynamics. *General Relativity and Gravitation* **40,** 329–356 (2008).

81. Tsujikawa, S. Quintessence: a review. *Class. Quantum Grav.* **30,** 214003 (2013).

82. Mangano, G., Miele, G., Pastor, S. & Peloso, M. A precision calculation of the effective number of cosmological neutrinos. *Physics Letters B* **534,** 8 –16. ISSN: 0370-2693 (2002).

83. Binétruy, P. Models of dynamical supersymmetry breaking and quintessence. *Phys. Rev. D* **60,** 063502 (1999).

84. Amaldi, U., de Boer, W. & Fürstenau, H. Comparison of grand unified theories with electroweak and strong coupling constants measured at LEP. *Physics Letters B* **260,** 447 –455 (1991).

85. Affleck, I., Dine, M. & Seiberg, N. Dynamical supersymmetry breaking in four dimensions and its phenomenological implications. *Nuclear Physics B* **256,** 557 –599. ISSN: 0550-3213 (1985).

86. Pisanti, O. *et al.* PArthENoPE: Public algorithm evaluating the nucleosynthesis of primordial elements. *Computer Physics Communications* **178,** 956 –971 (2008).

87. Cyburt, R. H., Fields, B. D., Olive, K. A. & Yeh, T.-H. Big bang nucleosynthesis: Present status. *Rev. Mod. Phys.* **88,** 015004 (2016).

88. Olive, K. & Group, P. D. Review of Particle Physics. *Chinese Physics C* **38,** 090001 (2014).

89. Ma, Z. The Nonlinear Matter Power Spectrum. *The Astrophysical Journal* **665,** 887 (2007).

90. Almaraz, E., Li, B. & de la Macorra, A. *in preparation* (2018).

91. Trotta, R. & Hansen, S. H. Constraining the helium abundance with CMB data. *Phys. Rev. D* **69,** 023509 (2004).

92. Ichikawa, K. & Takahashi, T. Reexamining the constraint on the helium abundance from the CMB. *Phys. Rev. D* **73,** 063528 (2006).

93. Seljak, U. & Zaldarriaga, M. A Line of Sight Approach to Cosmic Microwave Background Anisotropies. *Astrophys. J.* **469,** 437–444 (1996).

94. Lewis, A. & Bridle, S. Cosmological parameters from CMB and other data: A Monte Carlo approach. *Phys. Rev. D* **66,** 103511 (2002).

95. Li, M.-H., Wang, P., Chang, Z. & Zhao, D. CosmoMC Installation and Running Guidelines. arXiv: `1409.1354` (2014).

96. Lewis, A. Efficient sampling of fast and slow cosmological parameters. *Phys. Rev. D* **87,** 103529 (2013).

97. Bourilkov, D. Strong coupling running, gauge coupling unification and the scale of new physics. *Journal of High Energy Physics* **2015,** 117 (2015).

98. Trotta, R. *Bayesian Methods in Cosmology* in (2017). arXiv: `1701.01467`.

99. Hu, W. & Sugiyama, N. Small-Scale Cosmological Perturbations: An Analytic Approach. *The Astrophysical Journal* **471,** 542 (1996).

100. Hearin, A. P., Zentner, A. R. & Ma, Z. General requirements on matter power spectrum predictions for cosmology with weak lensing tomography. *Journal of Cosmology and Astroparticle Physics* **2012,** 034 (2012).

101. Tegmark, M. *et al.* Cosmological constraints from the SDSS luminous red galaxies. *Phys. Rev. D* **74,** 123507 (2006).

102. Planck Collaboration *et al.* Planck 2015 results. XI. CMB power spectra, likelihoods, and robustness of parameters. *A&A* **594,** A11 (2016).

103. Liddle, A. R. How many cosmological parameters. *Monthly Notices of the Royal Astronomical Society* **351,** L49–L53 (2004).

104. Chevallier, M. & Polarski, D. Accelerating Universes with Scaling Dark Matter. *International Journal of Modern Physics D* **10,** 213–223 (2001).

105. Linder, E. V. Exploring the Expansion History of the Universe. *Phys. Rev. Lett.* **90,** 091301 (2003).

106. Ettori, S. *et al.* Mass profiles and $c - M_{DM}$ relation in X-ray luminous galaxy clusters. *A&A* **524,** A68 (2010).

107. Abate, A. & Erdoğdu, P. Peculiar velocities into the next generation: cosmological parameters from the SFI++ survey. *Monthly Notices of the Royal Astronomical Society* **400,** 1541–1547 (2009).

108. Liu, X. *et al.* Cosmological constraints from weak lensing peak statistics with Canada-France-Hawaii Telescope Stripe 82 Survey. *Monthly Notices of the Royal Astronomical Society* **450,** 2888–2902 (2015).

109. Beutler, F. *et al.* The 6dF Galaxy Survey: $z \approx 0$ measurements of the growth rate and σ_8. *Monthly Notices of the Royal Astronomical Society* **423,** 3430–3444 (2012).

110. Howlett, C., Ross, A. J., Samushia, L., Percival, W. J. & Manera, M. The clustering of the SDSS main galaxy sample - II. Mock galaxy catalogues and a measurement of the growth of structure from redshift space distortions at $z = 0.15$. *Monthly Notices of the Royal Astronomical Society* **449,** 848–866 (2015).

111. Oka, A., Saito, S., Nishimichi, T., Taruya, A. & Yamamoto, K. Simultaneous constraints on the growth of structure and cosmic expansion from the multipole power spectra of the SDSS DR7 LRG sample. *Monthly Notices of the Royal Astronomical Society* **439,** 2515–2530 (2014).

112. Gil-Marín, H. *et al.* The clustering of galaxies in the SDSS-III Baryon Oscillation Spectroscopic Survey: RSD measurement from the LOS-dependent power spectrum of DR12 BOSS galaxies. *Monthly Notices of the Royal Astronomical Society* **460,** 4188–4209 (2016).

113. Blake, C. *et al.* The WiggleZ Dark Energy Survey: joint measurements of the expansion and growth history at $z < 1$. *Monthly Notices of the Royal Astronomical Society* **425,** 405–414 (2012).

114. de la Torre, S. *et al.* The VIMOS Public Extragalactic Redshift Survey (VIPERS). Galaxy clustering and redshift-space distortions at $z \simeq 0.8$ in the first data release. *A&A* **557,** A54 (2013).

115. Peebles, P. *The Large-scale Structure of the Universe* (Princeton University Press, 1980).

116. Linder, E. V. & Cahn, R. N. Parameterized beyond-Einstein growth. *Astroparticle Physics* **28,** 481 –488 (2007).

117. Linder, E. V. Cosmic growth history and expansion history. *Phys. Rev. D* **72,** 043529 (2005).

118. Batista, R. C. Impact of dark energy perturbations on the growth index. *Phys. Rev. D* **89,** 123508 (2014).

119. Courtin, J. *et al.* Imprints of dark energy on cosmic structure formation II. Non-universality of the halo mass function. *Monthly Notices of the Royal Astronomical Society* **410,** 1911–1931 (2011).

120. Pace, F., Waizmann, J.-C. & Bartelmann, M. Spherical collapse model in dark-energy cosmologies. *Monthly Notices of the Royal Astronomical Society* **406,** 1865–1874 (2010).

121. Press, W. H. & Schechter, P. Formation of galaxies and clusters of galaxies by self-similar gravitational condensation. *Astrophys. J.* **187,** 425–438 (1974).

122. Patrignani, C. *et al.* Review of Particle Physics. *Chin. Phys.* **C40,** 100001 (2016).

123. Yue, A. T. *et al.* Improved Determination of the Neutron Lifetime. *Phys. Rev. Lett.* **111,** 222501 (2013).

124. Aver, E., Olive, K. A. & Skillman, E. D. An MCMC determination of the primordial helium abundance. *Journal of Cosmology and Astroparticle Physics* **2012,** 004 (2012).

125. Iocco, F., Mangano, G., Miele, G., Pisanti, O. & Serpico, P. D. Primordial nucleosynthesis: From precision cosmology to fundamental physics. *Physics Reports* **472,** 1–76 (2009).

126. Aver, E., Olive, K. A., Porter, R. & Skillman, E. D. The primordial helium abundance from updated emissivities. *Journal of Cosmology and Astroparticle Physics* **2013,** 017 (2013).

127. Cooke, R. J., Pettini, M., Jorgenson, R. A., Murphy, M. T. & Steidel, C. C. Precision Measures of the Primordial Abundance of Deuterium. *The Astrophysical Journal* **781,** 31 (2014).

128. Izotov, Y. I., Thuan, T. X. & Guseva, N. G. A new determination of the primordial He abundance using the He I λ10830 Å emission line: cosmological implications. *Monthly Notices of the Royal Astronomical Society* **445,** 778–793 (2014).

129. Riemer-Sørensen, S. *et al.* A robust deuterium abundance; re-measurement of the $z = 3.256$ absorption system towards the quasar PKS 1937101. *Monthly Notices of the Royal Astronomical Society* **447,** 2925–2936 (2015).

130. Wright, E. L., Bennett, C. L., Górski, K., Hinshaw, G. & Smoot, G. F. Angular Power Spectrum of the Cosmic Microwave Background Anisotropy Seen by the COBE DMR. *The Astrophysical Journal Letters* **464,** L21 (1996).

131. Jones, W. C. *et al.* A Measurement of the Angular Power Spectrum of the CMB Temperature Anisotropy from the 2003 Flight of BOOMERANG. *The Astrophysical Journal* **647,** 823 (2006).

132. Stompor, R. *et al.* The MAXIMA experiment: latest results and consistency tests. *Comptes Rendus Physique* **4,** 841 –852 (2003).